DOI: 10.14750/ME.2024.016

ANTAL KERPELY DOCTORAL SCHOOL OF MATERIALS SCIENCE & TECHNOLOGY

Development of Polyurethane-based Nanocomposites to be Applied as Flexible Pressure Sensors

A Ph.D. dissertation submitted to Antal Kerpely Doctoral School of Materials Science & Technology for the degree of Doctor of Philosophy in the subject of Materials Science and Technology

by

Mohammed Nabeel Ibrahim Al-Mandalawi

Supervisors:

Dr. László Vanyorek

&

Dr. Mariann Kollár Szabó

Head of the Doctoral School

Prof. Dr. Valéria Mertinger

Institute of Chemistry

Faculty of Materials and Chemical Engineering

University of Miskolc

Hungary, 2023

DOI: 10.14750/ME.2024.016

Acknowledgments

First and foremost, I am extremely grateful to my supervisor, **Dr. László Vanyorek**, and co-supervisor **Dr. Mariann Kollár Szabó**, for their guidance, support, and encouragement throughout my Ph.D. journey. Their invaluable insights, expertise, and feedback have been instrumental in shaping my research and ensuring its quality. I would also like to extend my heartfelt thanks to the Head of the chemistry institute, **Prof. Béla Viskolcz**, for his unwavering support and mentorship. Prof. Viskolcz has been a great source of inspiration, providing scientific advice and emotional support whenever I faced challenges. I am indebted to **Béla Fiser**, whose scientific and linguistic contributions were indispensable in improving the quality of my research articles. His willingness to lend a helping hand has been truly appreciated. I would like to acknowledge the contributions of my colleagues, **Ádám Prekob** and **Emőke Sikora**, whose support has been invaluable in my research endeavors. I owe a debt of gratitude to **Dr. Ail J Addie** and **Dr. Mohaned Mousa**, whose scientific guidance and assistance have been instrumental in shaping my research and achieving its objectives. I would like to extend a special thanks to **Ágnes Solczi** for her friendship, empathy, and support. I am deeply grateful to my family, my dear wife, and my daughters, **Aya Ban**, and **Jwan** for their unwavering love, support, and understanding throughout my Ph.D. journey. Their encouragement and motivation were critical in helping me achieve my academic goals. I would also like to thank **my father**, **mother, and my siblings** for their financial and moral support, and their unwavering belief in me. Without them, I would not have been able to reach the completion of my scientific career. Finally, I would like to express my gratitude to my home country, **Iraq**, for allowing me to exchange experiences with a European country. I hope that I can repay my country in the future by contributing to its scientific advancement.

DOI: 10.14750/ME.2024.016

Contents

DOI: 10.14750/ME.2024.016

DOI: 10.14750/ME.2024.016

DOI: 10.14750/ME.2024.016

List of abbreviations and notations

e-skin	Electronic skin
FPS	Flexible pressure sensor
PU	Polyurethane foam
N-BCNT	Nitrogen-doped bamboo-shaped carbon nanotube
SR	Silicone rubber
CB	Carbon black
NBP	Nanocomposite based piezoresistive
PVA	Polyvinyl alcohol
CNT	Carbon nanotube
GNP	Graphene Nanoplate
MNPs	Metal nanoparticles
0D	Zero dimension
1D	One dimension
2D	Two dimensions
PDMS	Polydimethylsiloxane
MFF	Melamine Formaldehyde foam
PIF	PI-Polyimide foam
MPa	Megapascal
AuNP	Gold nanoparticles
rGO	Reduction graphene oxide
R	Electrical resistance
R_0	Initial electrical resistance
CCVD	Catalytic Chemical Vapor Deposition
SEM	Scanning electron microscopy

DOI: 10.14750/ME.2024.016

HRTEM	High-resolution transmission electron microscopy
FTIR	Fourier-transform infrared spectroscopy
TGA	Thermogravimetric analysis
XPS	X-ray photoelectron spectroscopy
S	Pressure sensitivity
P	Pressure
GF	Gauge factor
E	Strain

DOI: 10.14750/ME.2024.016

Abstract

Electronic skin (e-skin) is a synthetic skin that mimics human sensing abilities and has many applications, such as prosthetics, robotics, health monitoring, and artificial intelligence technologies. To adapt the e-skins to specific functions and properties, many attempts have been made with different mechanisms, approaches, materials, and structures. However, the high sensitivity and flexibility of the e-skin are the biggest drivers in the field of research. Therefore, to prepare a sensitive, flexible pressure sensor (FPS) for the e-skin application that can detect any movement, the applied materials and technologies used should be optimized.

The first step in optimizing the FPS was to develop a novel technology to prepare the applied nanocomposite. This was done by coating the polyurethane foam (PU) with nitrogen-doped bamboo-shaped carbon nanotube (N-BCNT) by dip coating and then impregnating it with silicone rubber (SR). PU was used as a supporting skeleton for N-BCNT, while SR was used as a polymer matrix to fill the pores of the foam to improve recoverability, compressive strength, and durability. N-BCNTs were used as conductive fillers due to their remarkable electronic behavior. Their fibrous structure spans the entire volume of the PU foam, allowing them to act as nanometric electrical cables that provide conductivity at the macroscopic dimension of the N-BCNT/PU-SR composite.

The second step was to optimize the best PU foam as the supporting skeleton for the nanofiller by preparing PU foam with different pore volumes by mixing commonly used isocyanate and polyol with different isocyanate indices (1.0:0.8, 1.0:1.0, 1.0:1.1). Then, the prepared polyurethane foam samples were dip-coated with a fixed ratio of N-BCNTs to obtain pressure sensor systems. The results show that the PU foam with a low isocyanate index and high pore volume has higher pressure sensitivity because it has a smaller PU scaffold. Consequently, more N-BCNTs are interconnected, resulting in more conductive paths and a larger effective conductive area in the PU scaffold.

The third step was to optimize the nanofiller by using N-BCNT and carbon black (CB) to coat PU by using different mixing ratios of the nanotube and CB (5:5; 6:4; 7:3; 8:2; 9:1). Then, the coated PU was impregnated with SR to fill the pores. Due to the higher aspect ratio of N-BCNTs, they contribute more to improving the electrical conductivity in the composites, while CB fills the smaller gaps among N-BCNTs. The results show that the optimal mixing ratio of 7:3 N-BCNT: CB is even better than N-BCNT alone. Thus, this mixing ratio is optimal in terms of pressure sensitivity due to the synergistic effect of the nanofillers. If the N-BCNT:

CB ratio is increased beyond 7:3, it becomes more difficult for the N-BCNT to align and expand, and the relative amount of CB also decreases, resulting in minimal contact between the fillers. On the other hand, decreasing the amount of N-BCNT decreases the ability of electrical charge transport over long distances along the aligned and extended nanotubes.

Finally, the optimized parameters and technologies were applied to prepare FPS for the advanced application of e-skin by dispersion of 7:3 N-BCNT: CB on PU foam prepared with a ratio of 1.0:0.8 polyol: isocyanate and then impregnated in SR. All in all, the method has the potential to improve the performance of pressure sensors that can be used for human activity monitoring and e-skin development. The final sensor exhibited higher pressure sensitivity due to more efficient electron transport through the SR-based nanocomposite. The pressure sensitivity was 0.4 kPa^{-1} and 0.07 kPa^{-1} in the range of 0-120 kPa and 180-1000 kPa, respectively. The sensitivity of the prepared system enables us to fabricate e-skin and other devices. A promising approach has been developed to improve the performance of FPS by optimizing the dispersion of the nanofiller in SR.

DOI: 10.14750/ME.2024.016

Chapter 1

Introduction and literature review

Introduction

1.1 Various types of flexible pressure sensors

FPS are devices that are designed to measure pressure by detecting deformation flexibly [1][2]. Conventional pressure sensors, in contrast, are rigid sensors and are not capable to adjust to complex shapes [3][4]. Conventional sensors are usually heavier than FPS and might also need to be installed in a certain way. Therefore, FPS are appropriate for a wide range of applications for which conventional sensors are not [5]. In general, FPS has several benefits over conventional sensors, such as the ability to measure irregular shapes, lightweight, long lifetime, and good pressure sensitivity. On the other hand, conventional sensors may be suitable for limited applications. FPS is promising as it can be used in many advanced applications such as health monitoring [6], intelligent robots [7], and aerospace devices [8].

The sensing mechanism of FPS can be piezoresistive [9][10], capacitive [11–13] and piezoelectric [14] (Figure 1). The response of the sensing mechanism differs depending on the type of materials that make up the sensor and the sensor's structure. The operating principle of the piezoresistive sensor is based on the change in electrical resistance in response to the application of pressure. When an external force acts on a piezoresistive sensor and causes it to change shape, the distance between the conductive fillers decreases, resulting in a decrease in electrical resistance. On the other hand, the capacitive sensor's working principle depends on the change in capacitance when pressure is applied to it [15]. A capacitive pressure sensor consists of two parallel conducting plates separated by the dielectric material. The FPS piezoelectricity type takes advantage of this effect by measuring the change in voltage as a function of the applied pressure. Piezoelectricity means that materials generate electrical voltage when pressure is applied to them. When pressure is applied, the piezoelectric sensor deforms and produces polarization phenomena. At the same time, negative and positive charges accumulate on their opposing surfaces and convert the mechanical pressure into an electrical signal [16]. All these types of electrical signals are measurable and calculated as a function of pressure. However, the piezoresistive type is the best choice because, first, piezoresistive sensors are manufactured cost-effectively. Second, due to its

DOI: 10.14750/ME.2024.016

high-pressure sensitivity, it is able to detect any pressure fluctuations [17]. Third, the piezoresistive sensor has high mechanical strength which makes it withstand mechanical stress without breaking [18].

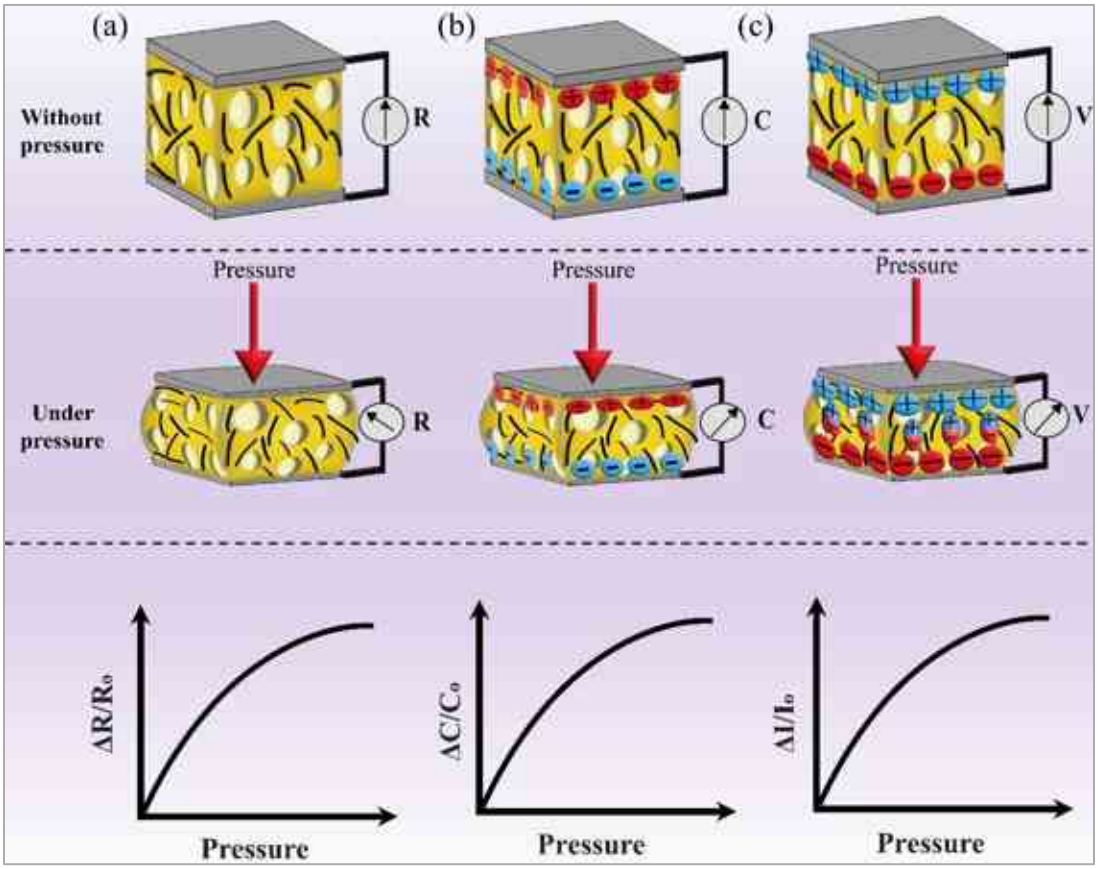

Figure 1. The sensing mechanism of flexible pressure sensors: piezoresistive (a), capacitive (b), and piezoelectric (c).

1.2 Preparation methods of flexible pressure sensors

FPS can be fabricated in many ways, such as piezoelectric materials, conductive polymers, and nanocomposite-based piezoresistive (NBP) systems. Piezoelectric is a substance that produces an electrical voltage when applying pressure on it. Such a phenomenon has been used to fabricate an FPS by incorporating piezoelectric constituents into the sensor system as displayed in Figure 2a. Polyvinyl alcohol (PVA) [19] is a piezoelectric polymer that has high-pressure sensitivity; however, it is expensive and cannot be used in high-temperature environments [20] Conductive polymers such as polyaniline are the type of materials that include free electrons, and they have the ability to have electrical conductivity [20]. The conductive polymer can be utilized in the

DOI: 10.14750/ME.2024.016

preparation of FPS by coating a flexible structure with a layer of this polymer as shown in Figure 2b. The polymer's electrical resistance alters when it experiences pressure, enabling the sensor to gauge changes in pressure [21]. The conductive polymer is easy to fabricate with excellent stability, however, it has low-pressure sensitivity and a delay in response time [22]. NBP materials comprise a matrix combined and a nanofiller such as graphene, CNT, and CB [19][23]. NBP materials can be utilized to create FPS by dispersion of nanofiller in the polymer matrix (Figure 2c). NBP is intrinsically flexible and elastic, making it the perfect choice for many applications where a sensor needs to conform to a curved surface or withstand repeated bending[24]. Unlike the piezoelectric sensor. In addition, NBP's pressure sensitivity has a wide range of highly sensitive materials such as CNT, graphene, and CB, making it possible to produce a pressure sensor that is highly sensitive even at low pressure. Unlike piezoelectric materials and conductive polymers, the ability to make a pressure-sensitive sensor is less sensitive due to the limited variety of materials. In addition, NBP is more durable than conductive polymers and piezoelectric materials, making it more appropriate for long-term use in harsh environments [25]. Finally, NBP technology is also relatively less expensive and easy to manufacture sensors for mass production. This makes it a promising technology for the next-generation manufacturing FPS [25].

DOI: 10.14750/ME.2024.016

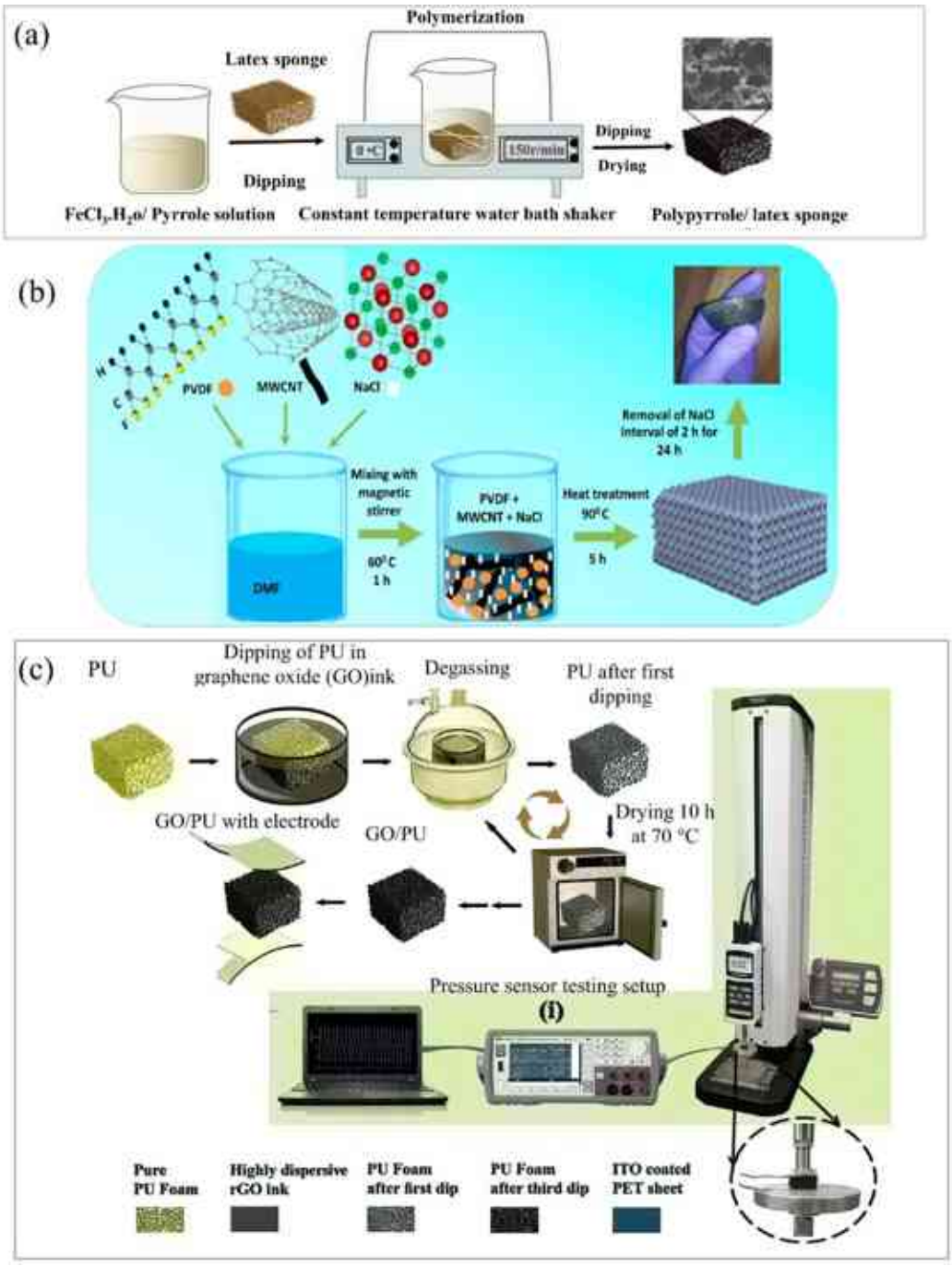

Figure 2. Preparation of flexible pressure sensors (FPS) by using a conductive polymer (a), [26] piezoelectric polymer (b), [27] and nanocomposite-based piezoresistive materials (c)[28].

1.3 Nanocomposite-based piezoresistive pressure sensors and their applications in e-skin technology

1.3.1 Types and properties of nanofillers in flexible pressure sensors

Nanofiller is a material that is combined with a matrix to enhance its characteristics [29]. In FPS technology, this has been used to enhance thermal, mechanical, and electrical characteristics [30][31]. This improvement is essential in maintaining FPS's overall strength and durability when exposed to external stresses, as well as guaranteeing its efficient thermal and electrical performance. Figure 3 displays various nanofillers commonly used in FPS sensors. Metal nanoparticles (MNPs), composed of pure metals like gold and silver, have become widely used in FPS due to their excellent electrical and mechanical characteristics [32,33][34][35][36,37]. Nevertheless, their production is quite challenging which limits their application in pressure sensors [38]. Graphene nanoplate (GNP) is one such material, consisting of hexagonal honeycomb lattices of carbon atoms tightly bound together [39,40]. GNP nanofiller offers outstanding tensile strength and high thermal and electrical conductivity [41], making it a suitable nanofiller for pressure sensors [42,43]. Unfortunately, while graphene's many potential uses are endless, its production and handling in large amounts remain challenging. In addition, CNT is another type of nanofiller often utilized in FPS. CNTs are rolled sheets of graphene with hemispherical endcaps and diameters ranging from less than 1 nanometer to several nanometers [44]. It has remarkable mechanical and electrical properties, such as superior electrical conductivity [45,46], excellent flexibility [47][48], and high tensile strength [49–51]. These desirable characteristics make CNTs an ideal solution for pressure sensors that require superior electrical and mechanical performance [52]. However, producing large quantities of CNTs could be costly, thus restricting its application beyond pressure sensors [53]. CB is one of the promising nanofillers created through thermal decomposition and incomplete combustion of carbon-hydrogen compounds [64][65]. CB possesses desirable characteristics like low cost and good electrical conductivity that make it suitable for FPS production. A hybrid nanofiller is a material system in which two or more different nanofillers are mixed with the polymer matrix. This can improve mechanical and electrical properties while being more cost-effective than single nanofillers like graphene or CNT. For instance, a hybrid nanofiller made of CB and CNT can offer superior mechanical and electrical properties at lower costs than using CNT alone. On the other hand, using this hybrid nanofiller improves dispersion quality, leading to increased effective conduction paths. CB acts as a

DOI: 10.14750/ME.2024.016

connecting point between CNTs, leading to decreased resistivity due to the synergistic effect of the two nanofillers. Thus, less loading is necessary to reach the electrical percolation threshold in the nanocomposite [54]. Moreover, different morphologies, shapes, and structures of nanofillers lead to different conductivity mechanisms which in turn increase pressure sensitivity [55].

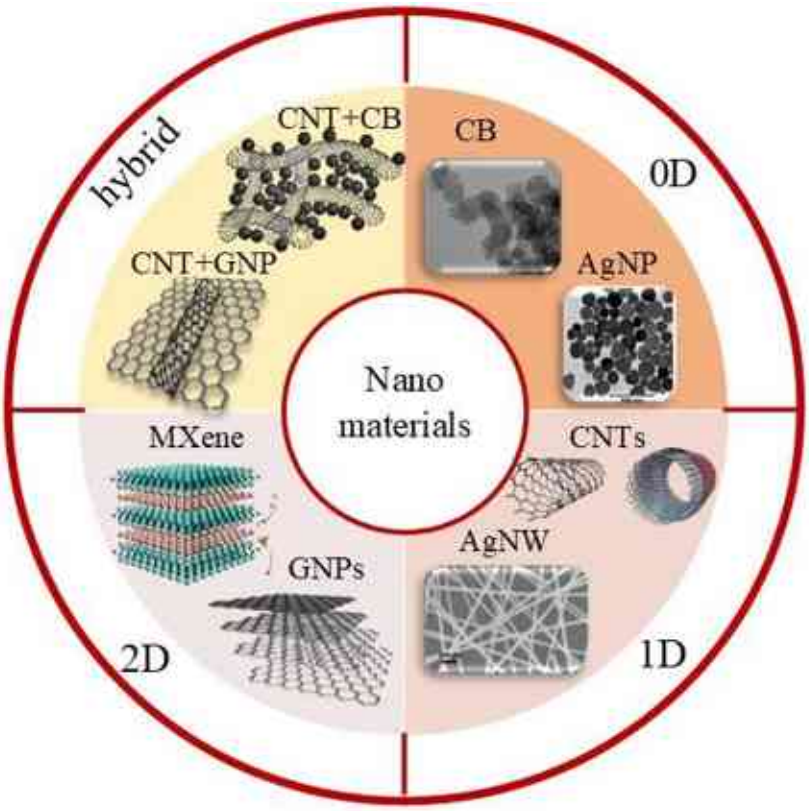

Figure 3. Classification of nanofillers used in flexible pressure sensors based on dimensionality: zero dimension (0D), one dimension (1D), and two dimensions (2D).

1.3.2 Properties and selection of polymer matrix for flexible pressure sensors

The polymer matrix serves as a base material for nanocomposite and holds the nanofillers together. At FPS, the polymer matrix should contribute to the required electrical and mechanical properties of the sensor [56]. The polymer matrix plays a crucial role in FPS and influences its electromechanical properties. Moreover, the sensor must be resistant to chemicals and the environment to have a long lifetime. The pressure sensors may be exposed to harsh environments or chemicals that can cause damage over time [57] [58]. Moreover, it might need particular features to function correctly in an FPS, such as high flexibility and elasticity to resist loads and deformations, which are crucial for increasing the sensor's durability and preventing breaking [59–

61]. Additionally, it must be electrically insulating to avoid electrical leakage since electrical leakage will impact the pressure sensor's accuracy [62,63]. Therefore, silicone rubber is the most common choice because it satisfies pre-request properties such as combining excellent mechanical, moderate chemical resistance, and high electrical conductivity. These properties make it able to resist the mechanical deformation that occurs during the application of pressure, and it has a high level of electrical insulation, which prevents current leakage and resists harsh environments.

1.3.3 Strategies for achieving uniform dispersion of nanofillers in the polymer matrix

To efficiently use the characteristics of nanofillers in FPS, it is crucial to create a continuous conductive network pathway inside the polymer matrix and achieve an electrical conductivity percolation threshold. Therefore, several approaches have been used such as increasing the nanofiller loading [64] [65]. However, this approach tends to form nanofiller bundles, leading to an increase in the viscosity of the polymer matrix[66]. This leads to difficulties in dispersing nanofillers and affects the performance of the sensors. Thus, high-power ultrasonication and shear mixing have been to achieve uniform dispersion of nanofiller in the polymer matrix is needed. However, this approach may cause thermal degradation and structural damage which leads to reduced sensor durability. Due to the applied high power the polymer chains may be broken at the center point or the structurally weakest points [67]. An alternative approach is by dispersion of nanofiller on a skeleton foam by using the dip-coating process and then, this structure is impregnated and combined with a polymer to achieve the final sensor system. By using this approach the nanofiller spans the entire volume of the polymer and provides electrical conductivity in the macroscopic dimension of the sensor. Moreover, it minimizes negative effects on the performance of the sensor because there is no further process needed.

1.3.4 Types of polymers to use in pressure sensors

Many types of foam structures have been utilized to fabricate FPS, such as polydimethylsiloxane (PDMS) [9,68–72], melamine formaldehyde foam (MFF) [73–77], polyimide foam (PIF) [78,79] and PU [80–84]. PDMS is made from dimethyldichlorosilane that reacts with H_2O during production. PDMS can also be produced through the reaction between hexamethylcyclotrisiloxane and octamethylcyclotetrasiloxane in the presence of either acidic or basic catalysts [85]. Porous structures created in PDMS foam can be created through direct templating [86,87], emulsion templating [88,89], gas forming [90,91] and 3D printing [92,93]. As PDMS is an elastic polymer it's mechanically and chemically robust while being non-toxic,

inexpensive to produce, and easy to shape [94–96]. However, two drawbacks hindered its use in pressure sensors: its virgin form has a solid structure and requires additional techniques to create a foam structure. Additionally, when making PDMS it is difficult to control the structure as we cannot adjust the reactant ratio. MFF is a flexible polymer with low density and high porosity that can be made from formaldehyde-melamine-sodium bisulfite copolymer [97]. MFF exhibits good mechanical properties; when pressure is applied it compresses and then returns to its original shape when released [98]. However, MFF has poor thermal properties and can decompose at low temperatures.[99]. Furthermore, PIF possesses excellent thermal characteristics like thermostability, flame retardancy, and excellent mechanical properties such as flexibility and tensile strength [100][101]. The powdered forming technique is the most widely employed and typical process for producing PIF [102]. PIF preparation involves two steps: (1) polymerizing benzophenone tetracarboxylic dianhydride and oxydianiline with a mixture of tetrahydrofuran and methanol; and (2) imidization process and thermal forming. The chemical and physical characteristics of PIF are determined by several factors, including foam structure, chemical composition, and density [103][104]. Nonetheless, compared to conventional substrates, the fabrication of PF-based sensors may require additional processing steps or challenges, which can increase the complexity and cost of manufacturing. PU is a highly flexible material with a high pore structure, low modulus of elasticity, and high resilience [105–108]. Thus, PU could be compressed up to 85% without plastic deformation [109]. PU is an extremely flexible material with a high pore structure, low modulus of elasticity, and excellent resilience [110]. Foaming of PU occurs when isocyanide, polyol, and water react, producing CO_2, and turning the polymer into foam. One of the fascinating properties of PU is that its properties can be tailored by altering the ratio between reactants. Isocyanate and polyol are two distinct segments of PU. Their phase separation and content, as well as how well these segments blend together, influence PU's structures and properties [111]. For example, changes in phase separation between hard and soft segments and content can significantly affect mechanical and physical characteristics [112] [113]. However, like other types of foam, PU foam is typically porous and allows liquid or gas penetration. This permeability can affect the performance of nanofillers, compromising sensor reliability [114].

Table1 outlines the physical and chemical characteristics of various supporting skeletons for nanofillers. It can be seen that PU foam structures are the best choice among other polymer foam structures due to their easy controllability when changing reactant ratios. Furthermore, the versatility of producing PU with a range of Young's moduli and high compressive strength enables its application in various pressure levels and applications. Furthermore, by selecting suitable polyol and isocyanates, one can make their product both hydrophilic and hydrophobic [115]. The polyol content of PUs tends to make them more hydrophilic, as isocyanates are reactive and responsible for polymerization and stiffness in PU. Therefore, an excessive amount of isocyanate will lead to stiffer and hydrophobic PU [115]. Hence, the ideal PU can be created by mixing it with nanofillers based on their hydrophilicity.

Table1. Physical and chemical properties of foamed polymer

Property type	**PU**	**PDMS**	**MFF**	**PIF**	**Ref.**
Foam structure	Easy to control	Hard to control	Easy to control	Hard to control	[116–119]
Young modulus (MPa)	0.08- 151.4	0.1 - 1	0.17-0.48	0.005- 11.17	[93,120–124]
Compression strength (MPa)	0.14-1.95	0.1-0.5	0.04-0.15	0.098- 0.8	[125–129]
Hydrophilicity	Hydrophilic and hydrophobic (Based on compound mixing ratio)	Hydrophobic	Hydrophilic	Hydrophobic	[130–136]
Chemical resistance	Good	Good	Weak	Good	[137–141]
Biocompatibility	Biocompatible	Biocompatible	Biocompatible	Biocompatible	[142–146]
Cost	Low	Moderate	Low	Low	[147][148][149]

1.3.5 Methods for dispersion of nanofillers onto foam skeletons nanofillers onto foam skeletons

There are several methods for the dispersion of nanofiller on the pores of polymer skeletons such as dip coating, sputtering, spray coating, and in-situ polymerization as shown in Table 2. Sputtering describes the ejection of atoms from a target by using high energy. Subsequently, the ejected atoms are deposited on the substrate material [150]. This technique was used to fabricate FPS by sputtering gold nanoparticles (AuNP) onto PU foam [151]. Spray coating is a process in which materials are sprayed through a nozzle to form a fine aerosol [152]. This method has been used to fabricate FPS by depositing conductive aerosol layer by layer on foamed PDMS [153]. Spray coating involves applying a thin layer of a material to a substrate by spraying a suspension liquid or solution of the material onto the surface. This approach is often used to produce FFPS as it is a relatively simple and scalable process. The coating liquid is sprayed onto the supporting substrate such as PDMS using a spray gun or other spray device. The spray parameters, such as the spray rate and distance, are precisely controlled to ensure that an even coating is applied.[153][154] During in-situ nanocomposite polymerization, nanoparticles are dispersed in a monomeric solution and then, polymerization is carried out in the presence of the dispersed nanoparticles.[155] Hu *et al.*[156] describe the preparation of a polyurethane-based conductive sponge by coating it with silver nanoparticles after in situ synthesis of poly(3,4-ethylenedioxythiophene)(PEDOT) on the backbone of a PU foam. Silver nitride is then dissolved in deionized water and the PU sponge is immersed in the silver nitride solution for 5 minutes, followed by drying at 60°C for 6 hours to obtain a PU/ PEDOT -Ag pressure sensor [155][156]In dip coating, a conductive nanofiller is dispersed in a suitable solvent and the foamed structure is then immersed in the nanofiller solution. Finally, the solvent is removed in an oven to obtain a dispersed nanofiller on the foamed structure.

Table 2 revealed, that the dip coating method is the most suitable for the fabrication of FPS because it is the most cost-effective method, the sensor can be used directly, no special equipment is required, and the substrates can be fully covered with nanofiller. In addition, a wide range of nanofiller types and concentrations can be used, which is a very efficient method for mass production.

DOI: 10.14750/ME.2024.016

Table 2. The advantages and limitations of methods used for the dispersion of nanofiller in skeleton foam

Methods	Advantage	Limitation	Ref.
Spray coating	Speed process, low risk, ultra-thick coatings, no phase changes, no oxidation, minimum thermal input to the substrate.	Inappropriate for complex shapes, the sprayed material is subjected to plastic deformation, which leads to a reduction in the ductility of the coating layers	[158] [159] [160]
Sputtering	The process can be performed at low temperatures, the no-change microstructure, uniform coating thickness, good adhesion, and eco-friendly	Slow process (typically less than 300 nm/min), surface treatment of substrate required, and high equipment cost.	[161] [162]
in-situ polymerization	Improve the agglomeration of the nanoparticles and at the same time ensure excellent dispersion in the polymer matrix.	Properties of the final product can be affected by unreacted substance of the in-situ reaction	[163]
Dip coating	Simple, cost-effective, practical, and applicable for different scale sizes. Easily control the electrical resistance of the pressure sensor by manipulation of the nanofiller loading and the number of dip coatings.	Considering the polarity of the solvent, nanofiller, and substrate is necessary to ensure good dispersion of the nanofiller on the substrate.	[164] [165]

1.4 Application of flexible pressure sensors `

FPS with a wide pressure range, high flexibility, and excellent pressure sensitivity meet the requirements for use in wearable and e-skin applications [166]. Generally, an FPS is attached to the human body or placed on wearable textiles to detect human activity. FPS can be used both in the low-pressure range, such as breath and speech recognition, and in the high-pressure range,

DOI: 10.14750/ME.2024.016

such as motion detection. Chen *et al.* prepared MXene/PU foam and used it for e-skin and wearable device applications [167]. Due to the wide range of pressure detection, the sensor can recognize voices, facial movements, and hand and foot movements (Figure 4a-e) [168,169].

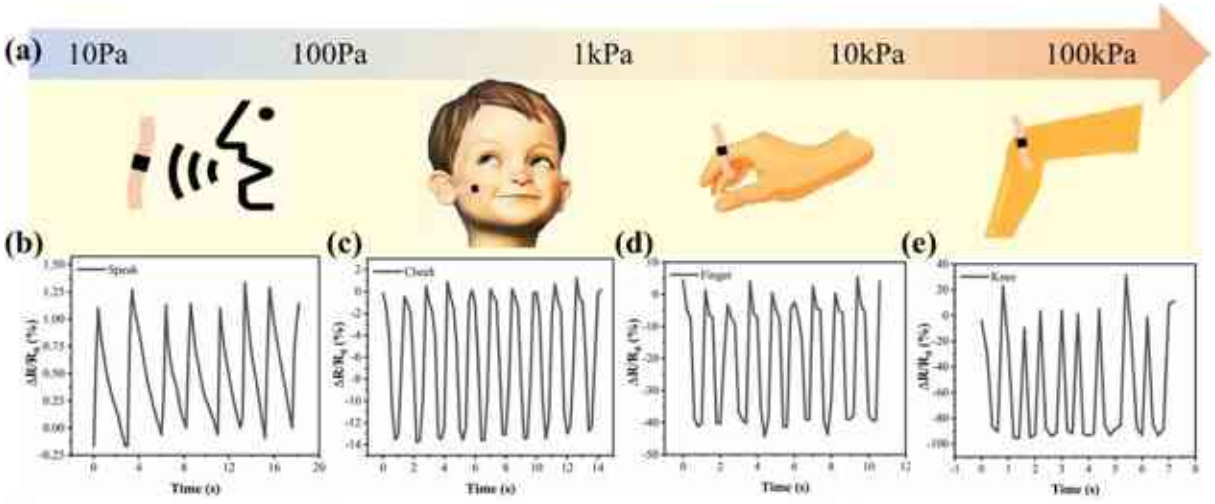

Figure 4. Application of flexible foam pressure sensors (FPS): (a) pressure range, (b) speech, (c) cheek, (d) finger, and (e) knee motion detection [167].

Lue *et al.* developed rGO/PU and used it as a wearable pressure sensor to detect human activity. The sensor was placed on the neck, index finger joint, wrist, elbow, shoe sole, and face (Figure 5) [170]. The results revealed that the current intensity changes proportional to the pressure applied during neck bending, finger movement, wrist bending, arm bending, walking movement, and facial expression. When human motion compresses the sensor, the current of the sensor increases as responds to the deformation of the sensor and returns to its initial value when the pressure is removed. These are encouraging results that offer the possibility to use foam-based sensors in intelligent robot applications. Dai *et al.* created a CNT/PDMS foam pressure sensor that was fitted in various locations on the human body to detect different practical body movements and physiological signs (Figure 6 a-c) [68]. The sensor is attached to the wrist to detect the peaks of the heart pulse (a) and it can distinguish the peaks of T (tidal), P (percussive), and D (diastolic) in each heart pulse from the steady waveforms of the radial artery pulse at a heart rate of 68 beats per minute. An FPS was also able to detect breathing by placing it on the subject's chest to monitor respiration, which is an important physiological signal to prevent sleep apnea. Periodic breathing produces repeatable variations of $\Delta R/R_0$ (Figure 6b). In addition, the $\Delta R/R_0$ of the sensor shows different and repetitive patterns when the tester pronounces "Silicon," "Hi," and "Sensor"

DOI: 10.14750/ME.2024.016

indicating a possible application in speech recognition devices (Figure 6c).

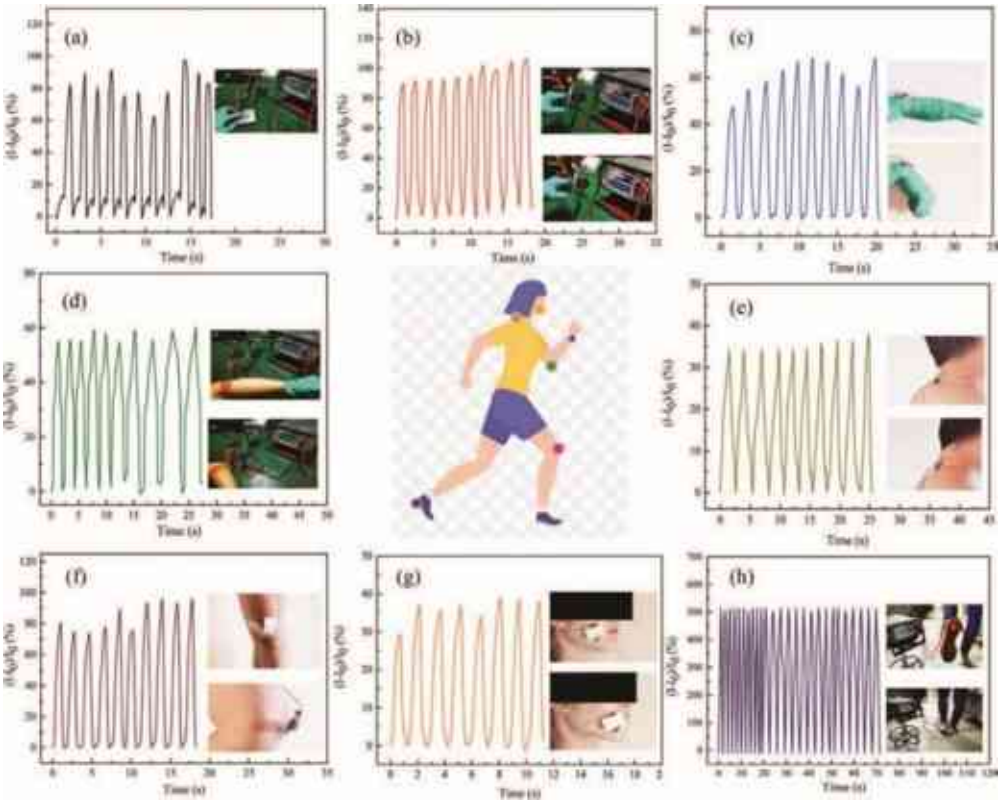

Figure 5. Monitoring human motion using rGO/PU foam sensor: (a) finger pressing, (b) finger movement, (c) wrist bending, (d) arm bending, (e) nodding, (f) knee bending, (g) facial expression of cheek-bulging, and (h) walking [170].

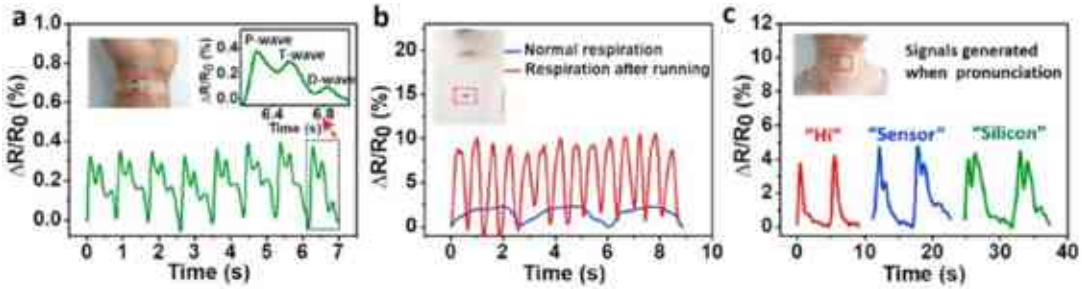

Figure 6 Applications of the CNT/PDMS sensor for detecting various physiological signals and monitoring human body movements: (a) wrist pulse monitoring. The inset shows the pulse waveform of one cycle (right), where the P-wave, T-wave, and D-wave are visible. (b) Monitoring of respiration under normal conditions and after running. Inset: photo of the sensors attached to the chest. (c) Detection of various acoustic stimuli when the wearer spoke: "Hi", "Sensor", "Silicon" [68].

DOI: 10.14750/ME.2024.016

1.5 Thesis objective

The goal is to develop a piezoresistive FPS for e-skin applications using nanocomposite technology. The piezoresistive type is the best sensing mechanism because it is low-cost, it has high-pressure sensitivity and can detect minute pressure variations. Nanocomposites have been selected for the fabrication of FPS because they are very sensitive, low cost, and very durable. Nanocomposites consist of a matrix and a nanofiller. Since hybrid nanofillers are less expensive and more pressure sensitive than pure CNT-based pressure sensors, N-BCNT and CB were selected as nanofillers. In turn, the introduction of a hybrid nanofiller improves the dispersion quality, leading to an increase in effective conduction paths. Silicone rubber was chosen as the polymer matrix due to its high flexibility and excellent chemical and electrical properties. To ensure the functionality of FPS, it is important to obtain a homogeneous dispersion of nanofillers in the polymer matrix. However, it can be difficult to disperse nanofillers uniformly in polymers with high viscosity, such as silicone rubber, which could limit the performance of the sensors. To solve this problem, we have developed a novel approach based on the dispersion of nanofillers on the skeleton of PU foam by dip coating and subsequent impregnation of the coated PU with SR. It is worth mentioning that we optimized PU foam to obtain the best pressure sensitivity by mixing commonly used isocyanate and polyol with different isocyanate indices (1.0:0.8, 1.0:1.0, 1.0:1.1) to obtain different pore volumes. The results show that the sample with a larger pore volume of PU foam leads to higher pressure sensitivity because the PU scaffold is smaller. Consequently, more nanofillers are interconnected, resulting in more conductive paths and a larger effective conductive area in the PU scaffold. The current research provides the shortest electron transport channels in silicone rubber. In addition, the use of a hybrid N-BCNT:CB nanofiller has a synergistic effect on pressure sensor performance that cannot be achieved with either material alone.

DOI: 10.14750/ME.2024.016

Chapter 2

Experimental work

2.1 Materials

The N-BCNTs were prepared by catalytic chemical vapor deposition (CCVD) method and the physical properties of the resulting N-BCNTs are reported in Table 3. The CB was produced by Birla Carbon Hungary Ltd. and is a pure carbon without stabilizers and its physical properties are shown in Table 3. The exceptional properties of CB and N-BCNTs make them ideal materials for a wide range of applications, especially in the field of pressure sensors. The PU was produced using the Topline casting machine (Hennecke GmbH). The silicone rubber consists of liquid silicone rubber (Silorub ds F-20) and a catalyst (Silorub ds K), which were manufactured in China. The silicone rubber produced was used as a polymer matrix for the pressure sensor. It has a Shore A hardness of 20 and a tensile strength of 1.65 N/m^2. These mechanical properties suggest that it's suitable for high-pressure resistance applications. It's also a good electrical insulator, preventing electrical leakage, which would affect the accuracy of the pressure sensor. The silicone rubber also has good thermal resistance and moderate chemical resistance, making it suitable for use in harsh environments. Patosolv is a mixture of aliphatic alcohols, 98% ethanol, and 2% isopropanol purchased from Molar Chemicals Ltd. in Halásztelek, Hungary, and used as a dispersant for the nanofiller. The use of the dispersion medium reduces the agglomeration of the nanofiller and increases the surface area, resulting in better dispersibility.

Table 3 Physical properties of N-BCNT [171] and CB

	Density (g/cm^3)	**$NSA_{(BET)}$ (m^2/g)**	**Metal impurities (wt.%)**	**Particle diameter (nm)**	**Length (µm)**
CB	0.44	35	0.0	81.8 ± 33.1	-
N-BCNT	-	146	7.0	20.4 ± 4.6	> 2

2.2 Characterization techniques

To ensure the excellent performance of manufactured pressure sensors, it is crucial to analyze the structure and morphological qualities of the materials used to construct the sensor. We applied cutting-edge technologies to assess the relationship between the qualities of the materials used in the production of FPS and the manufacturing process. Our findings demonstrate the efficacy of these methodologies for evaluating the pressure sensor's quality and acquiring a comprehensive understanding of its behavior in various environments.

2.2.1 Scanning electron microscopy

Scanning electron microscopy (SEM) (Thermo Fisher Scientific, Waltham, MA, U.S.) was used to examine the morphology of the nanofiller and FPS. The SEM facilitates the visibility of minute features and details at high magnifications, making it a suitable instrument for the characterization of the pressure sensor's materials. The materials and prepared FPS were coated with gold sputtering. In addition, the SEM was used to study the dimension of the nanofiller and its distribution in the polymer matrix of FPS.

2.2.2 High-resolution transmission electron microscopy

The synthesized N-BCNT, as well as CB, were examined by high-resolution transmission electron microscopy (HRTEM) using an FEI Technai G2-20X Twin machine with an acceleration voltage of 200 kV. The sample preparation was carried out by dropping the aqueous suspension of the samples onto a copper grid (300 Mesh, only carbon from Ted Pella). TEM is an advanced technology used to study materials at the nanoscale level. TEM is a valuable tool for investigating materials that are difficult to investigate by conventional techniques due to their small size or composition.

2.2.3 Fourier-transform infrared spectroscopy (FTIR)

FTIR (Bruker Vertex 70) spectrometer was used to examine the functional groups on their surfaces. All in all, 2 mg of synthesized N-BCNT as well as CB was added to 250 mg spectroscopic potassium bromide, and after homogenization, a pellet was created which was used in the measurements carried out in transmission mode.

2.2.4 Measuring Zeta Potential by Laser Doppler Electrophoresis

Zeta potential (Malvern Nano Zs instrument) measurements were applied to determine the surface charge of N-BCNT and CB in aqueous dispersions [172]. Also understanding the

interactions between N-BCNT, CB, and the suspension and prediction of suspension stability and dispersion. It measures the negative charge at the interface between a solid and a liquid in which it is suspended. A high zeta potential value indicates a high repulsive force between nanofillers as a result of a high surface charge, causing a more stable suspension and vice versa.

2.2.5 Thermogravimetric analysis

Thermogravimetric analysis (TGA) is widely acknowledged as an effective method for investigating the thermal behavior and purity of materials. Therefore, the carbon content and purity of N-BCNTs and CB were determined by TGA using a Netzsch Tarsus TG 209 thermal microbalance. TGA measurements were performed in a mixed atmosphere ((nitrogen (4.5) and oxygen (5.0)) with the flow rate set at 6 $mL*min^{-1}$ and 14 $mL*min^{-1}$ for O_2 and N_2, respectively. Combustion in pure oxygen was considered too fast; therefore, a mixture of nitrogen and oxygen was used to burn the carbon content of the samples. The heating rate was 10 $^oC\ min^{-1}$, in the temperature range of 35-800 ^oC.

2.2.6 X-ray photoelectron spectroscopy

X-ray photoelectron spectroscopy (XPS) is a surface analysis technique commonly used to assess the elemental composition and oxidation states of elements as well as the kind of bonding at the surface of materials. [173]The XPS using a SPECS Phoibus 150 MCD nine analyzer has been used to identify the nitrogen incorporation types in the N-BCNTs.

2.2.7 Micro CT measurements

Micro-CT is a non-destructive analytical method that generates high-resolution, three-dimensional pictures of a sample using X-rays. These photos can be used to examine the structure of PU foam and establish the level of SR incorporation into the foam's pores. Micro CT measurements with YXLON FF35 equipment (microfocus X-ray tube) with parameter transmission beam, acceleration voltage: 90 kV, Al filter: 0.5 mm, and voxel size: 15.6 µm. The pores were analyzed by using the porosity analysis/foam structure analysis modules of the VG Studio software after applying adaptive Gaussian filtering.

2.2.8 Pressure sensor performance characterization

To measure the performance of the flexible pressure sensor, the pressure was applied with the Zwick/Roell Z010 universal tensile testing machine, and the change in electrical resistance was

DOI: 10.14750/ME.2024.016

measured simultaneously with an oscillator (FLUKE 8808 A) as shown in Figure 7. All measurements were carried out at room temperature.

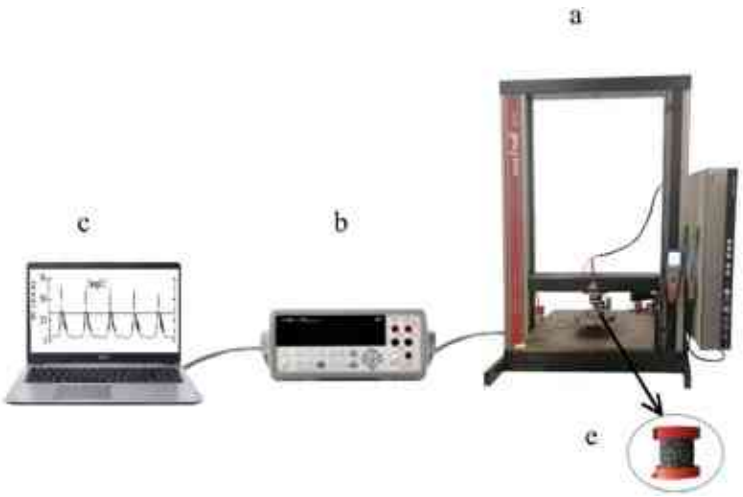

Figure 7 The flexible pressure sensor performance examination setup. (a) tensile test device, (b) oscillator, (c) computer to collect the data, and (e) the sample.

2.3 Methods

2.3.1 Preparation of N-BCNT

The synthesis of the N-BCNTs was carried out by using the CCVD method as shown in Figure 8. Nickel-containing catalyst ($Ni(NO_3)2*6\ H_2O$, from Thermo Fisher GmbH) with 5 wt. % and 2.00 g of magnesium oxide (Merck Ltd., Germany) were placed into a quartz reactor in a tube furnace, which was heated up to 750 °C. The time of synthesis was 20 min, and the dosing speed of n-butylamine ($C_4H_{11}N$, Sigma-Aldrich Ltd., Hamburg, Germany), which was used as a carbon source, was 6 $mL*h^{-1}$. The while flow rate of the nitrogen (99.995% purity, Messer Ltd., Budapest, Hungary) used as carrier gas was 100 mL min^{-1}. The production cycle was repeated ten times and then, the N-BCNT sample was purified, and the catalytic mixture (magnesium oxide and nickel) was removed by using concentrated hydrochloride acid (36 wt. %).

DOI: 10.14750/ME.2024.016

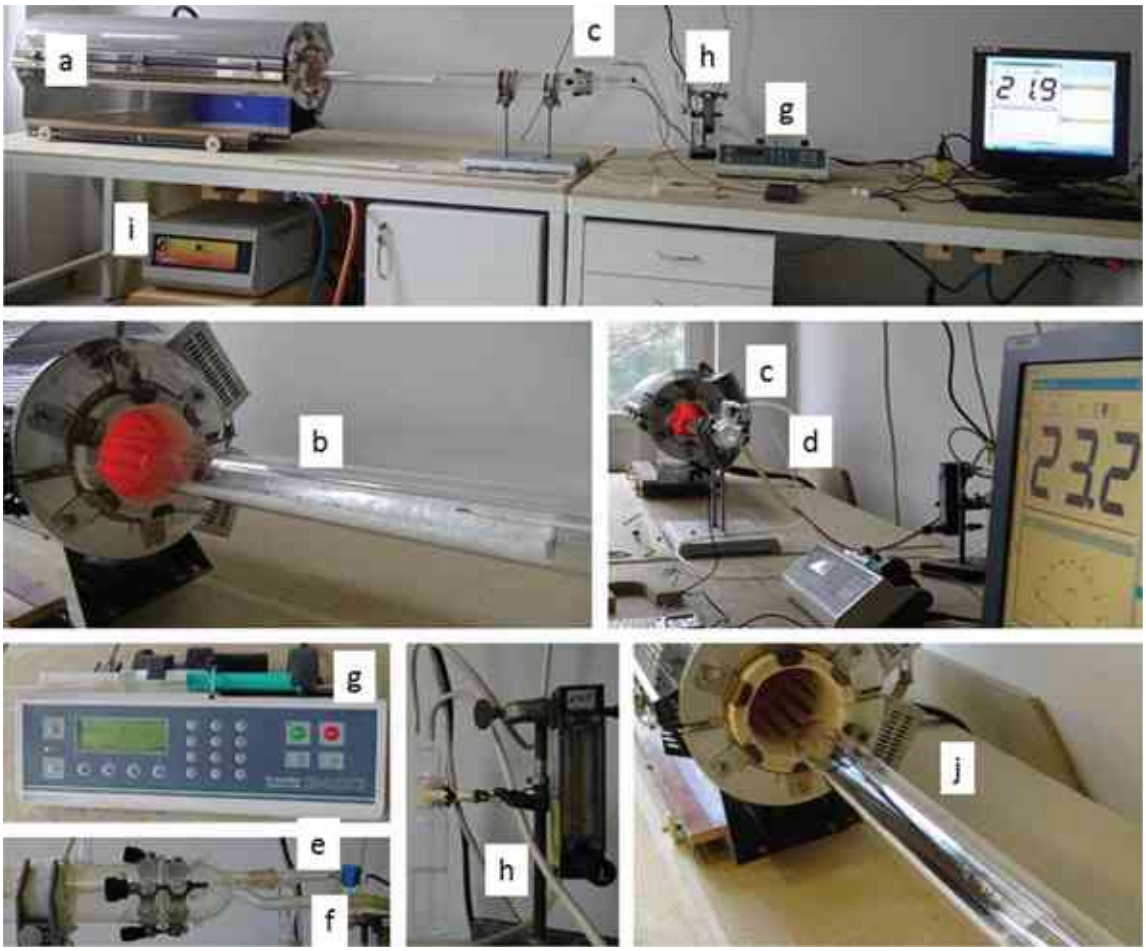

Figure 8. The experimental setup used in the synthesis of N-BCNT. The setup consists of a tube furnace (a), a quartz reactor (b), a carrier gas inlet (c), a carbon source feeder (d), a temperature sensor (e), an outlet for gases (f), a syringe pump (g), a nitrogen flow meter (h), a control unit for the tube furnace (i), and a quartz bowl containing the N-BCNTs with catalyst (j).

2.3.2 Synthesis of the polyurethane (PU) foam

The manufacture of PU foams was carried out by the reaction of isocyanate and polyol, while water was also added as a blowing agent to initiate the formation of CO_2. Carbon dioxide transforms polyurethane into PU foam. The water content of the polyol was 3.6 wt.%. The amount of water was controlled by weighing the water and the polyol separately with a precision balance before mixing. The isocyanate is the so-called hard segment, while the polyol is the soft segment in the PU. The structural, mechanical, and physical properties of the polymer are controlled by their ratio. The PU samples were prepared using the Topline casting machine (Hennecke GmbH) as shown in Figure 9 a-c. The machine operated with a high-pressure process and was suitable to

produce flexible polyurethane foams. Mixing of the components (polyol and isocyanate) took place in the mixing head by a countercurrent injection process. The robotic arm with the high-pressure mixing head (Figure 9 a) was applied to inject the reaction mixture (a mixture of raw materials) into the jacketed thermostatic aluminum mold (Figure 9 b). The final size of the PU product is 400 × 400 × 100 mm. Then cylindrical samples (h = 32 mm, d = 29) were cut out and used to make the piezoresistive sensors.

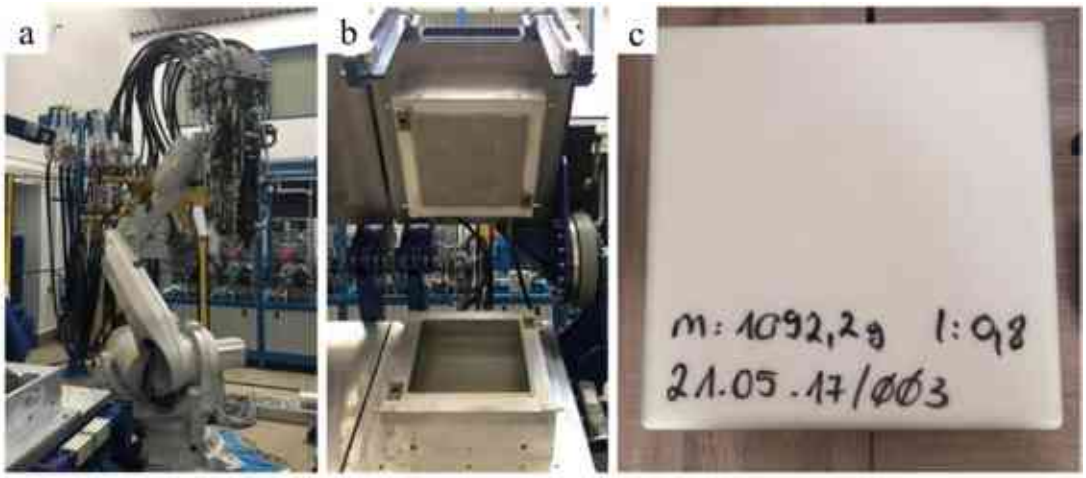

Figure 9. Illustrates a robotic arm system designed for the precise injection of raw materials to PU foam synthesis. The system consists of a robotic arm (a) and a mold (b) for shaping the injected PU foam.

2.3.3 Preparation of N-BCNT-PU/SR flexible pressure sensors

The pressure sensor nanocomposite was prepared in several steps as shown in Figure 10. First, the PU foam was prepared by mixing 11.9 g TR4040 isocyanate and 20.0 g FFP 303 polyol using a shear mixer for 10 s at 5000 rpm and room temperature. Then, the PU foam was cut into rectangular pieces (45 mm x 42 mm x 38 mm). Then, three different amounts of N-BCNT (0.1, 0.2, and 0.3 g) were dispersed in patosolv (150 mL) using the Hielscher UIPHdt1000 tip homogenizer (340 w/19.42 kHz) for 8 min. Thereafter, the PU samples were immersed in the N-BCNT suspension. Then, the treated foam samples were dried at 105 ^{o}C to evaporate the solvent and obtain the N-BCNT/PU systems. The dipping and drying process was repeated three times to maximize the amount of N-BCNT absorbed by the foam samples. In the next step, the N-BCNT/PU systems were vacuum-impregnated with silicone rubber to fill the pores of the foam as much as possible. This method ensures a more even uniform dispersion of N-BCNT compared to

DOI: 10.14750/ME.2024.016

directly mixing it into the polymer matrix. Thus, N-BCNT-PU/SR samples were obtained in Table 4, which were cut into cylindrical shapes before testing.

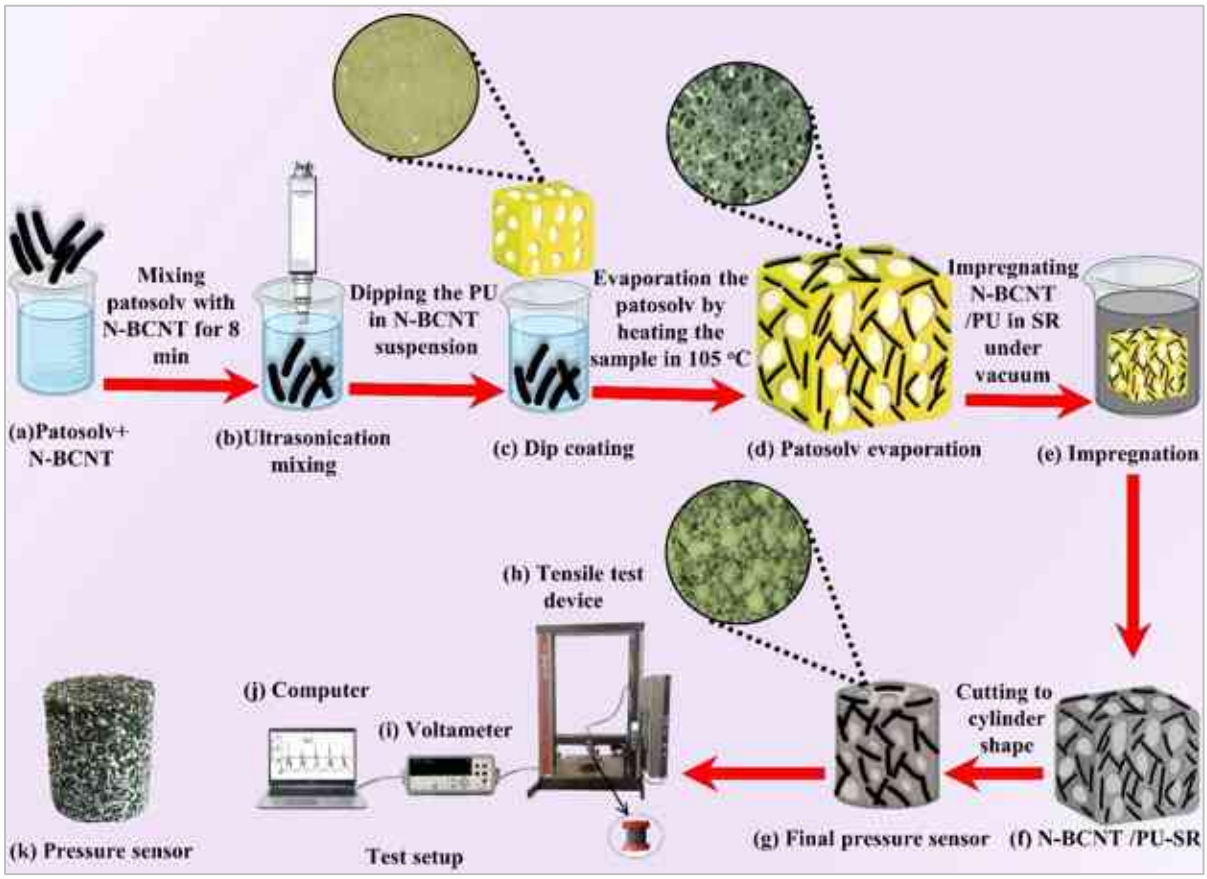

Figure 10. Schematic representation of the preparation and testing of the N-BCNT/PU-SR FPS. Mixing N-BCNT with alcohol (a). Dispersion of N-BCNT in alcohol by ultrasonication (b). Dipping the PU samples into the N-BCNT solution (c) and drying the N-BCNT/PU system (d). Vacuum impregnation of the N-BCNT/PU samples with silicone rubber (e,f). Cutting the N-BCNT/PU-silicone rubber nanocomposite samples (g). In the pressure-resistance test, the pressure was applied to the pressure sensor samples with tensile test equipment (h), a voltameter was used to calculate the change in electrical resistance under pressure (i), and a computer was used to record the data (j). The real image of the pressure sensor (k).

Table 4. Loading ratios of silicone rubber, PU, and N-BCNT in the prepared N-BCNT/PU-SR samples

samples	N-BCNT wt.%	PU wt.%	Silicon rubber wt%
sample 1	0.43	4.52	95.05
sample 2	0.21	3.07	96.71
sample 3	0.13	3.5	96.37

2.3.4 Preparation of N-BCNT: CB-PU/SR flexible pressure sensors

The preparation of the pressure sensor involved several steps as shown in Figure 11. First, the PU foam was prepared by mixing 11.9 g of TR4040 isocyanate and 20.0 g of FFP 303 polyol in a shear mixer for 10 seconds at 5000 rpm and room temperature. Then, 0.3 g of hybrid nanofiller with different mixing ratios (5:5, 6:4, 7:3, 8:2, 9:1) of N-BCNT and CB (Table 5) were dispersed in patosolv (150 ml) using Hielscher UIPHdt1000 tip homogenizer (340 W/19.42 kHz) for 8 min. Thereafter, the PU samples were immersed in the N-BCNT: CB suspension and the treated foam samples were dried at 105 ^{o}C to evaporate the solvent and obtain the N-BCNT: CB/PU systems. In the next step, the samples were impregnated with SR under a vacuum to fill the pores of the foam as much as possible and to obtain the final N-BCNT: CB/PU-SR pressure sensors. The results show the optimal mixing ratio of nanofillers was 7:3 N-BCNT: CB/PU-SR sensor regarding pressure sensitivity.

Table 5. Loading ratios of SR, PU, and N-BCNT in the prepared N-BCNT: CB/PU-SR pressure sensor samples.

No.	N-BCNT: CB mixing ratio	N-BCNT: CB wt.%	PU wt.%	Silicon rubber wt.%
1	5:5	0.45	4.49	95.06
2	6:4	0.46	4.41	95.13
3	7:3	0.47	4.39	95.14
4	8:2	0.44	4.41	95.15
5	9:1	0.43	4.38	95.19

DOI: 10.14750/ME.2024.016

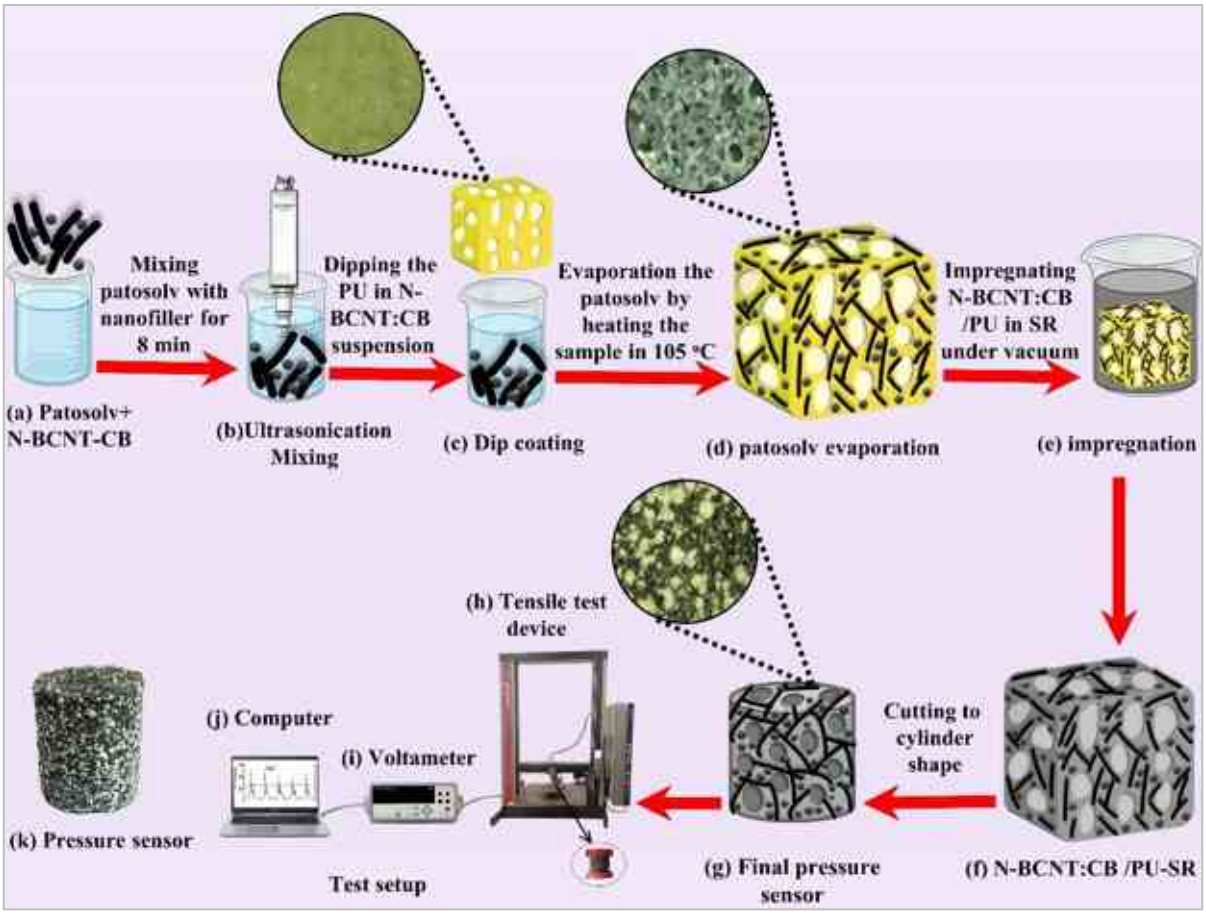

Figure 11. Schematic representation of the preparation steps and testing of the FPS (N-BCNT: CB/PU-SR) which are based on N-BCNT and CB as nanofillers, PU as supporting substrates, and SR. Mixing N-BCNT and CB with patosolv (a). Dispersion of N-BCNT: CB in patosolv by ultrasonication (b). Dipping the PU samples into the N-BCNT: CB suspension (c). Patosolv evaporation to obtain N-BCNT: CB/PU (d). Impregnation of the N-BCNT: CB/PU samples with SR (e-f). Cutting of N-BCNT/PU-SR nanocomposite samples (g). In the pressure-resistance test, the pressure was applied to the pressure sensor samples with tensile test equipment (h), the voltameter was used to calculate the change in electrical resistance under pressure (i), and a computer was used to record the data (j). The real image of the pressure sensor (k).

2.3.5 Preparation of N-BCNT/PU flexible pressure sensors

Three different types of PU foam were prepared by reacting an isocyanate with different isocyanate indices (Table 6), produced by the topline casting machine. The ratio of isocyanate to polyol in the reaction mixture was systematically modified to obtain different pore volumes within

DOI: 10.14750/ME.2024.016

the PU foams. Subsequently, the effect of pore volume on the pressure-sensing properties of the PU foam was investigated. The production of PU foams was carried out by the reaction of isocyanate and polyol, while water was also added as a blowing agent to initiate the formation of CO_2. Carbon dioxide transforms polyurethane into PU foam. The pressure sensors were then prepared in several steps as shown in Figure 12 a-e. First, ≈0.147 g N-BCNT was dispersed in 100 mL patosolv for 8 min using a Hielscher UIPHdt1000 tip homogenizer (340 W/19.42 kHz, Figure 12 b). Then, the PU foam samples were immersed into the N-BCNT dispersions and after that, the samples were dried at 105 °C to evaporate patosolv and obtain the N-BCNT/PU pressure sensors (Figure 12 c,d). Immersion and drying were repeated three times to maximize the amount of N-BCNT absorbed by the foam samples. The weight percentage of the added N-BCNTs to PU foam is the same for all samples as shown in Table 6. The results proved that the best type of polyurethane is 1.0:0.8 a polyol-to-isocyanate ratio to be used in the manufacture of N-BCNT/PU pressure sensors as a result of its superior pressure-sensing behavior.

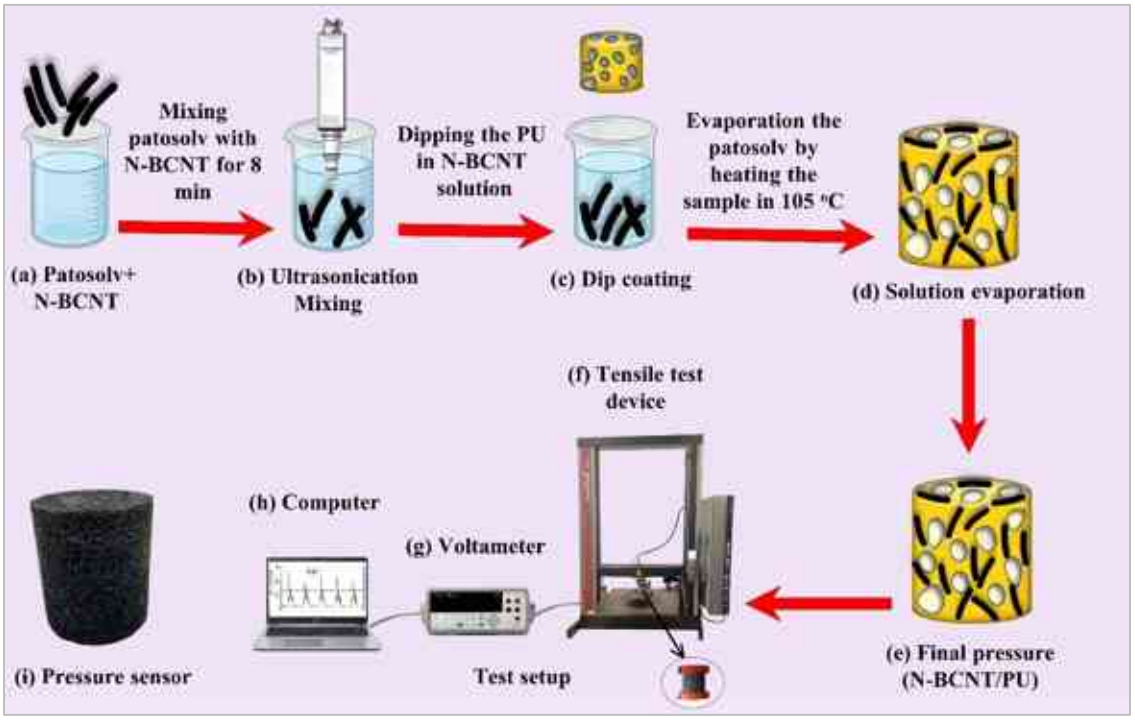

Figure 12. Schematic representation of the preparation and testing of the designed N-BCNT/PU sensor. Mixing N-BCNT with alcohol (a), dispersion of N-BCNT in alcohol by applying sonication (b), immersion of PU samples into the N-BCNT dispersion (c), drying the N-BCNT/PU system (d-e), testing the pressure sensor (f-h), picture of the pressure sensor (i).

Table 6. N-BCNT and PU weight of the prepared N-BCNT/PU nanocomposite

samples	Polyol: Isocyanate ratio	N-BCNT weight	PU weight
sample 1	1.0:0.8	0.146 g	1.46 g
sample 2	1.0:1.0	0.147 g	1.47 g
sample 3	1.0:1.1	0.141 g	1.41 g

2.3.6 Preparation of N-BCNT: CB-PU/SR flexible pressure sensors for e-skin application.

Manufacturing high-performance FPS for e-skin applications requires optimum manufacturing technology. Therefore, as previously discussed in sections 2.3.3, 2.3.4, and 2.3.5 and highlighted in Figure 13 an analysis was made to select the best manufacturing technology, PU foam type, and nanofiller. To obtain high performance of FPS, a novel technology was used by dispersion of nanofiller on PU foam by dip coating to obtain electrically conductive structure, then impregnation is silicon rubber. This technology provides a shortcut for electron transport inside silicone rubber. In addition, the best nanofiller mixing was found to be a 7:3 N-BCNT: CB mixing ratio, because the use of a hybrid nanofiller revealed improved pressure sensitivity compared to the use of N-BCNT alone. Furthermore, the selection of PU foam was according to a suitable mixing ratio of polyol: isocyanate (1:0.8), as it was found to result in the best sensing performance. The e-skin fabrication process was conducted in several steps, as outlined in Figure 14. The PU foam was cast using a topline casting machine, and the nanofiller (N-BCNT: CB) was dispersed in patosolv solvent via ultrasonic treatment for 8 minutes. The resulting nanofiller suspension was then utilized to impregnate the PU foam, which was dried at 105°C to evaporate the solvent, resulting in the formation of a stable N-BCNT: CB/PU system. The PU samples were then impregnated with SR and subjected to vacuum treatment to fill the pores of the PU foam. This resulted in the formation of the N-BCNT: CB/PU-SR pressure sensor, which was then cut and shaped for use in e-skin applications.

DOI: 10.14750/ME.2024.016

Figure 13. The optimization of the technology, PU foam type, and mixing ratio of nanofillers for the fabrication of e-skin was carried out.

DOI: 10.14750/ME.2024.016

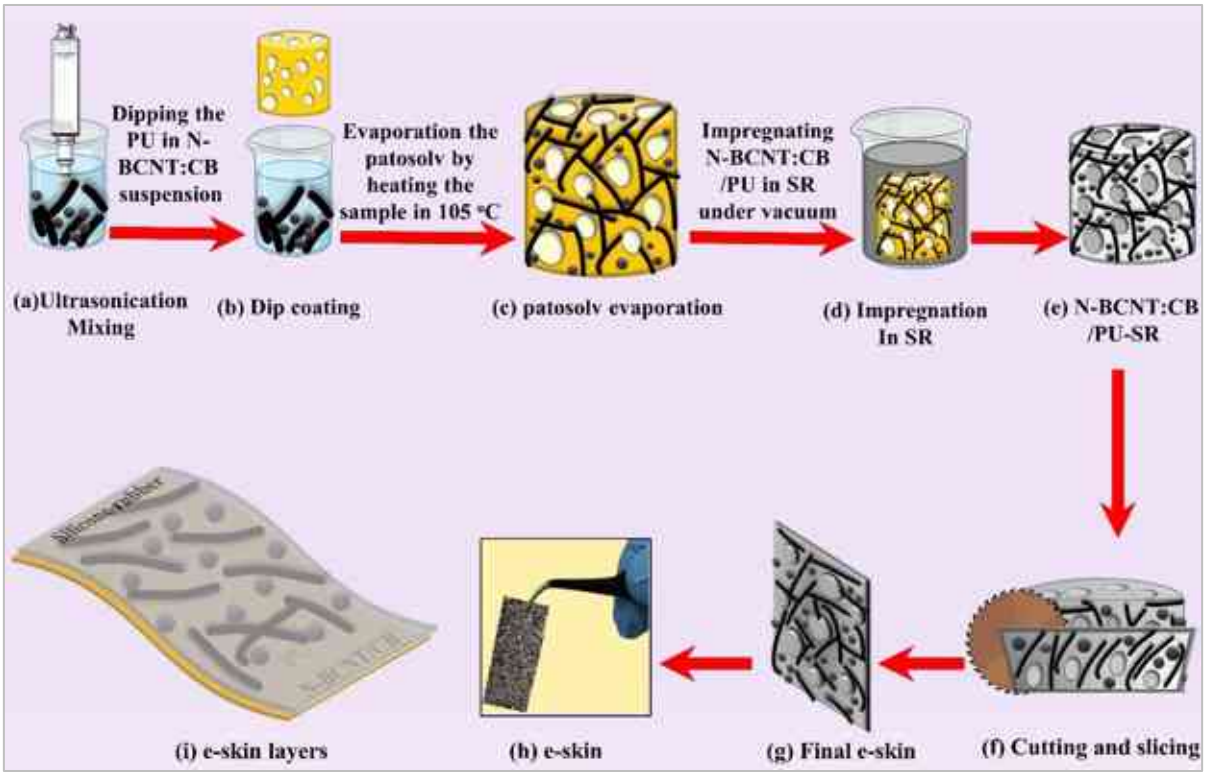

Figure 14. Preparation steps for the manufacture of e-skin. The process includes mixing a nanofiller with ultrasonication in patosolv (a), dip coating of PU in the nanofiller suspension (b), heating to evaporate the patosolv (c), impregnating the sample in SR to obtain N-BCNT: CB/PU-SR (d-e), cutting and slicing (f), resulting in the final e-skin sample (g) and the e-skin (h), e-skin layers (i).

DOI: 10.14750/ME.2024.016

Chapter 3

Results and Discussion

3.1 Characterizing of N-BCNT and CB

3.1.1 Characterizing N-BCNT and CB Purity Via Thermogravimetric Analysis

TGA is an analytical technique used to test material purity by measuring weight loss with temperature at a constant rate of heating[174]. For this analysis, 20 mg of N-BCNTs and CB were heated from 35 ^{o}C to 800 ^{o}C at 10 degrees Celsius/min as shown in Figure 15. Pure oxygen was considered too rapid for combustion, so a mixture of nitrogen and oxygen was employed instead to burn off the carbon content in the samples. Therefore, TGA measurements were conducted in a mixed atmosphere of nitrogen (4.5) and oxygen (5.0), with flow rates set to 6 mL/min^{-1} for O_2 and 14 mL/min^{-1} for N2. The analysis for CB revealed its purity was 100%; thus, there were no impurities present. Conversely, N-BCNT's purity was 93% due to residual catalytic material due to the CCVD method utilized during production.

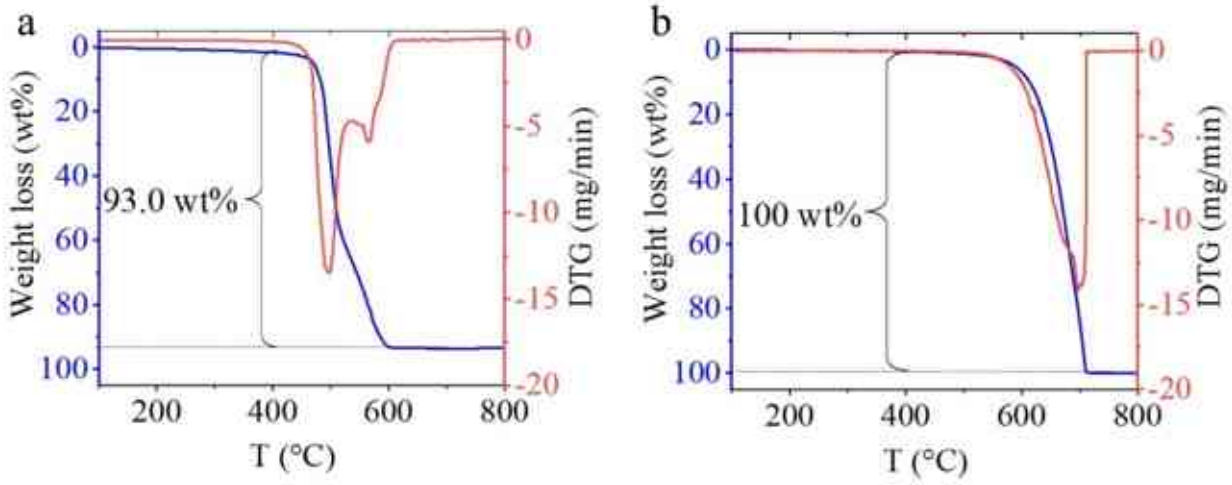

Figure 15. TGA for N-BCNT (a) and CB (b).

3.1.2 Identification of hetero atoms incorporated into the N-BCNT structure by XPS method

XPS was utilized to identify the types of nitrogen incorporation in N-BCNTs. Three distinct forms were detected: graphitic, pyridinic, and oxidized. XPS measurements confirmed this incorporation of nitrogen. The structure of an N-BCNT contains C-N bond types as a result of the deconvolution of the N 1s band (Figure 16a). There are three bands at 404.8, 401.3, and 398.7eV which correspond to graphitic (pyridine N-oxide), pyridinic, and graphitic nitrogen respectively.

DOI: 10.14750/ME.2024.016

The XPS spectrum also revealed other bonds. The peak in C 1s deconvoluted band of nanotubes corresponds to the C=C bond (graphitic Carbon), at 284.5 eV binding energies (Figure 16a). C-O and C-N bonds were detected as an adsorption peak at 287.6 eV, while another peak at 291.1 eV could have been caused by C-O bonds within the structure itself. The incorporation of these nitrogen atoms into the system will lead to structural distortion (bamboo-shape, edges) and electronic property change [175].

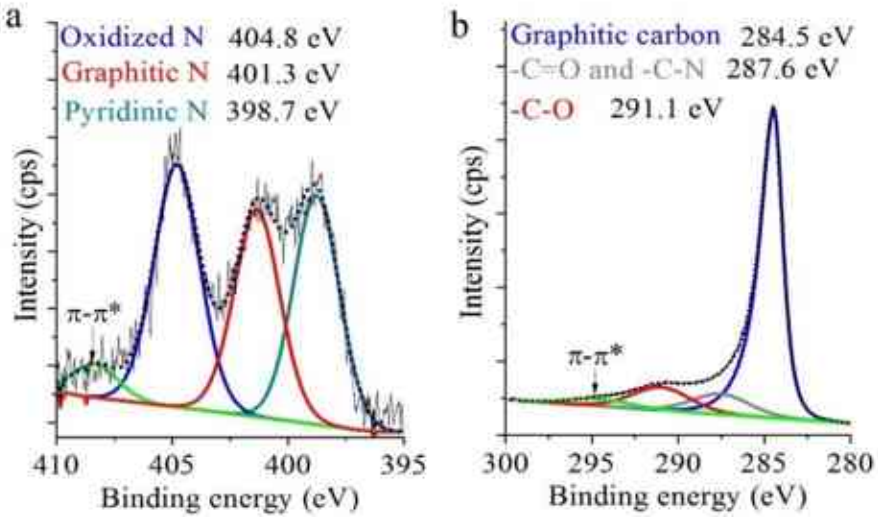

Figure 16. XPS spectra of N-BCNT: N 1s band E and C 1s band (F) are presented to showcase the chemical binding types of the species incorporated in N-BCNT respectively.

3.1.3 Identification of surface functional groups of CB and N-BCNT by FTIR analysis

FTIR tool that can be utilized to study the functional groups chemical and composition present on the surface of materials[176]. In the case of N-BCNTs and CB, FTIR can be used to identify the presence of functional groups, such as hydroxyl and carboxyl groups. These functional groups are formed during the synthesis of CB and the acid purification of N-BCNTs. FTIR spectra of N-BCNTs and CB were obtained by the absorption of infrared radiation by the sample. The spectra were then examined to determine which absorption peaks correspond to the vibrational modes of particular functional groups[177]. The synthesis of CB and purification of N-BCNT results in the presence of functional groups, this enhances the dispersibility in liquid media. The FTIR spectra of N-BCNT and CB, shown in Figure 17, reveal a band at 1065 cm^{-1} associated with C-O stretching vibrations of hydroxyl and carboxyl groups. An absorption peak at 1400 cm^{-1}, corresponding to the βOH vibrational mode, is indicative of the presence of hydroxyl, carboxyl

DOI: 10.14750/ME.2024.016

groups, and adsorbed water. Peaks at 1631 cm^{-1} (N-BCNT) and 1628 cm^{-1} (CB) are attributed to νC=C stretching, corresponding to skeletal vibrations of CNTs and the graphitic structure of carbon black. The νC=O bands at 1661 cm^{-1}, overlapping with C=C bands in both nanostructured carbon forms, likely originate from carbonyl or carboxyl groups. Additionally, peaks at 2823 cm^{-1} and 2905 cm^{-1} are due to C-H bond stretching. Broadband around 3400 cm^{-1} owing to stretching vibration (νOH) of hydroxyl functional groups. Deprotonation of hydroxyl groups, leading to a decrease in the zeta potential of N-BCNT and CB and stabilization of their aqueous dispersion[178].

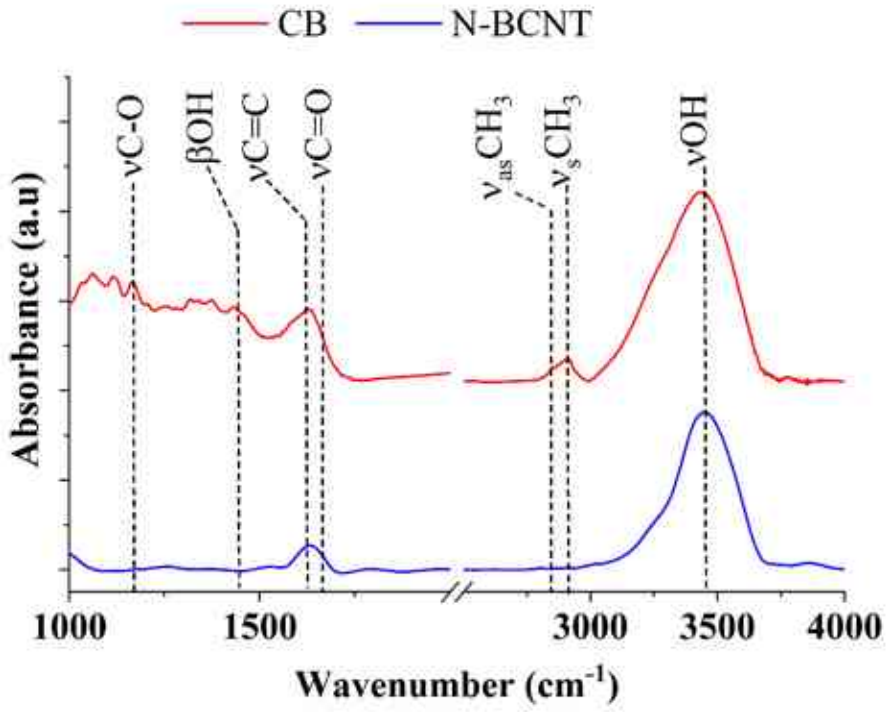

Figure 17. FTIR analysis of N-BCNT and CB

3.1.4 Zeta potential analysis of N-BCNT and CB

Zeta potential is the charge generated at the interface between particles and their liquid medium [179]. The zeta potential provides information about the stability of dispersions of nanomaterials in the aqueous phase, the wettability of these materials, and the polar character of their surface. As can be seen in Figure 18 the zeta potential of CB and N-BCNT is -21.8 mV and -24.5 mV, respectively. The negative zeta potential is due to the oxygen-containing functional groups on the surface, especially the hydroxyl and carboxyl groups, donating their protons and creating a negative charge on the surface of the carbon particles. The negative zeta potential leads

to electrostatic repulsion between the carbon nanoparticles, which is why stable aqueous dispersions can be prepared from them. This zeta potential indicates that CB and N-BCNTs are stabilized in aqueous media, so the potential for aggregation decreases, and the suspension remains dispersed. This ensures that the carbon nanotubes and carbon black particles can be homogeneously distributed in the structure of the PU foams during their wet impregnation. The homogeneous distribution of the carbon nanomaterials in the foam structure is a prerequisite for proper electrical contact between these electrically conductive nanoparticles. For this reason, this information is important to understand the interactions of CB and N-BCNTs in aqueous media and to predict their stability or dispersibility.

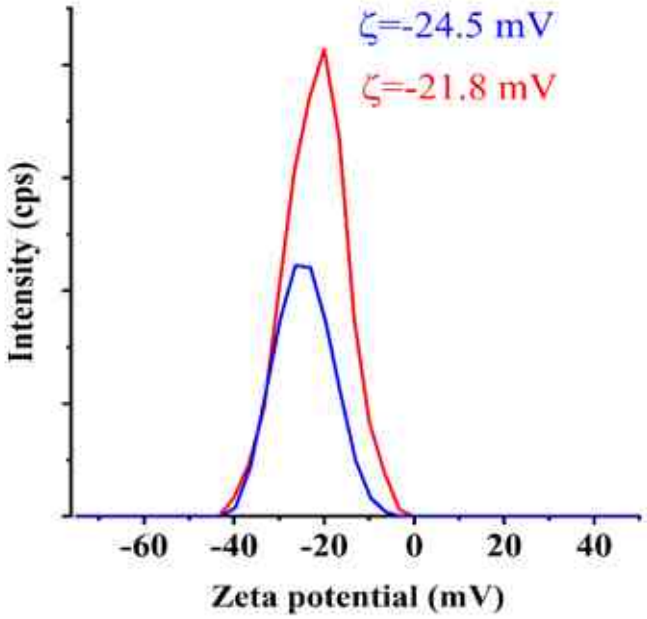

Figure 18. Zeta potential analysis of N-BCNT and CB

3.1.5 Characterization of CB and N-BCNT morphology and structure by HRTEM

HRTEM was used to characterize the microstructure of CB and N-BCNT at the nanoscale level. As shown in Figure 19 a-d the fibrous structure of the carbon nanotubes can be seen on the purified N-BCNT sample. The average diameter of the outer tube is 19.7 nm, Catalyst-related contamination is not visible next to the nanotubes, and the hemispherical fullerene-like building blocks of the N-BCNTs are also visible in the images. Graphene edges are visible on the walls of carbon nanotubes in the high-resolution image, as result in the formation of a high number of

DOI: 10.14750/ME.2024.016

oxygen-containing functional groups in those areas. The majority of these functional groups are hydroxyl and carboxyl groups. These groups experience deprotonation when exposed to an aqueous medium and contribute to the formation of a stable dispersion. In the case of CB, the images show the aggregated structure of CB, which is composed of smaller carbon particles in the nanoscale range(Figure 19 e-f). The two conductive carbon nanomaterials have different morphologies that result in improved electrical conductivity when coated on PU foam. This synergistic effect can be explained by the fact that the carbon nanotubes behave like nanosized tubes when they connect the carbon black aggregates.

DOI: 10.14750/ME.2024.016

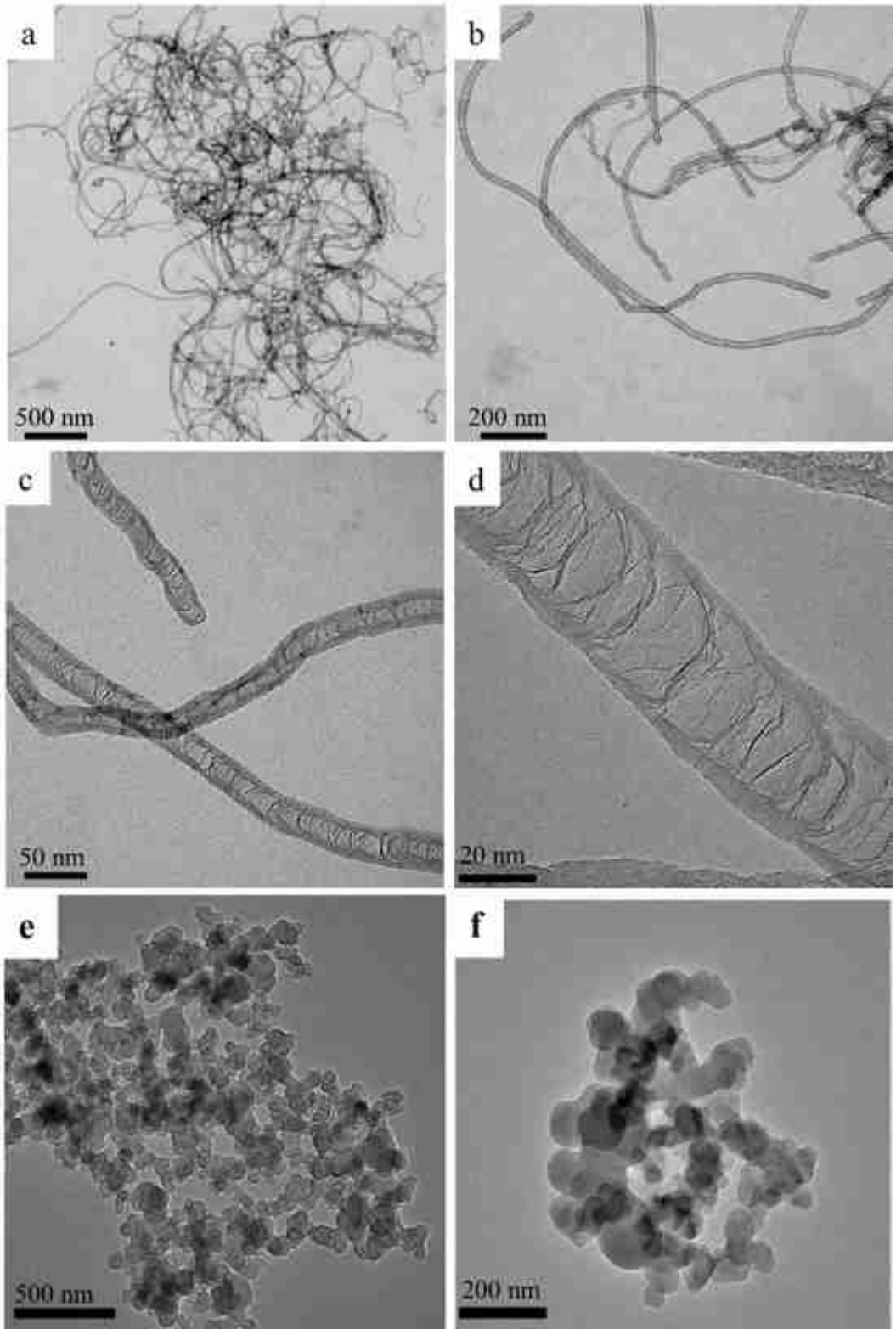

Figure 19.HRTEM images of N-BCNT and CB at various magnifications (a-f).

DOI: 10.14750/ME.2024.016

3.2 N-BCNT-PU-SR flexible pressure sensor performance evaluation

In this part, I will analyze the N-BCNT-PU/SR FPS that was the manufacturing process described in 2.3.3. Including sensing mechanisms, cyclic load, pressure sensitivity, and mechanical properties. In addition, the investigation of sensor morphology and its relationship to performance outcomes is explored.

3.2.1 Piezoresistive and electrical properties of N-BCNT-PU/SR flexible pressure sensor

Figure 20 depicts the investigation of the electrical resistance of the N-BCNT: CB/PU- SR in response to the applied pressure. The data indicate that the electrical resistance reduces with increasing pressure. For example, when the pressure is increased from 100 kPa to 200 kPa, sample 1 resistance falls from 90 kΩ to 20 kΩ. Because under pressure the distance between the N-BCNT will be closer, resulting in a more conductive network being created. Additionally, greater N-BCNT loading resulted in lower initial resistance, namely 450 kΩ, 2220 kΩ, and 6500 kΩ for sample 1, sample 2, and sample 3, respectively. The phenomena associated with increased N-BCNT loading as a conductive nanofiller reduces electrical resistance. Since the presence of additional N-BCNT increases the polymer matrix's conducting network.

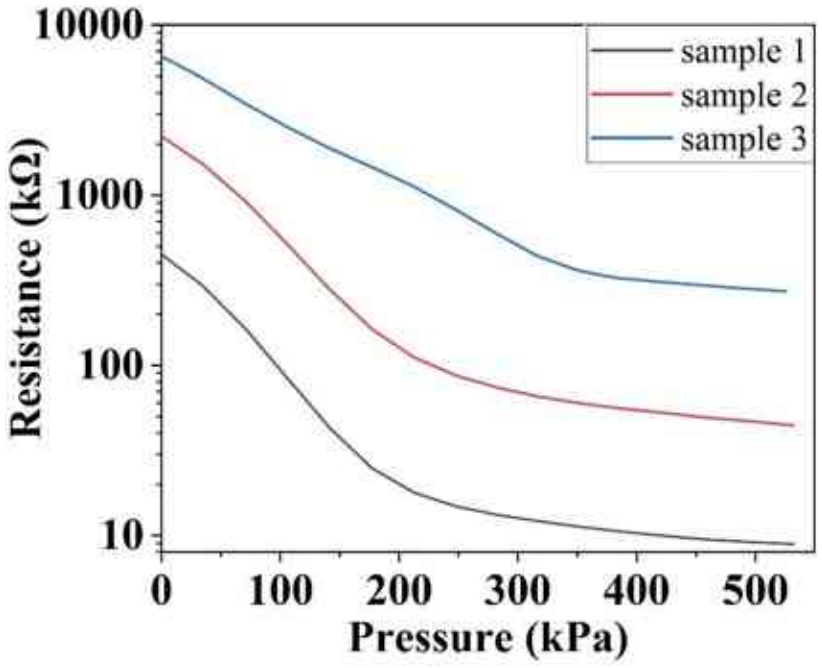

Figure 20. The relationship between applied pressure and electrical resistance for N-BCNT-PU/SR in three distinct samples (1, 2, and 3).

DOI: 10.14750/ME.2024.016

Furthermore, in the range of 80 kPa and 210 kPa, where the pressure climbs gently and the curve flattens, is the plateau region. The pressure increases considerably at the compaction zone (>210 kPa) because the conductive N-BCNTs within the PU skeleton are too close together.

The pressure sensitivity (S) of the piezoresistive pressure sensor is calculated by measuring the slope of the curve of the relative resistance changes versus the applied pressure and can be calculated according to the following equation:

$$S = (\Delta R/R_0)/\Delta P \quad (1)\ [180]$$

The relative resistance changes are ($\Delta R/R_o$), where $\Delta R=R-R_o$, R_o is the initial resistance in Ω, R is the electrical resistance while the sensor is under pressure, and ΔP is the varying pressure in Pa. The pressure sensor's pressure sensitivity is the most important characteristic since it determines the sensor's measuring efficiency and accuracy. [181] According to Table 7 and Figure 21, the result shows that when N-BCNT concentration increases, the pressure sensitivity increases. This is because the N-BCNTs act as the conductive phase, and it's responsible for the resistance change in response to applied pressure. Increasing N-BCNT leads to a greater more conductive inside polymer matrix. Therefore, a larger amount of N-BCNTs, more of this conductive path created in the sensor, contributing to an increase in the overall resistance change at a given pressure. These results suggest that N-BCNT is an efficient nanofiller for FPS to enhance sensitivity and performance due to the high aspect ratio and high electrical conductivity [182].

Table 7. The pressure sensitivity of N-BCNT: CB/PU-SR pressure sensor samples in different pressure ranges

Samples	***S* in the range of 0-75 kPa^{-1}**	***S* in the range of 180-500 kPa^{-1}**
1	$3.5 *10^{-3}$	$8*10^{-4}$
2	$2.1*10^{-3}$	$6.5*10^{-4}$
3	$1.9*10^{-3}$	$5.7*10^{-4}$

DOI: 10.14750/ME.2024.016

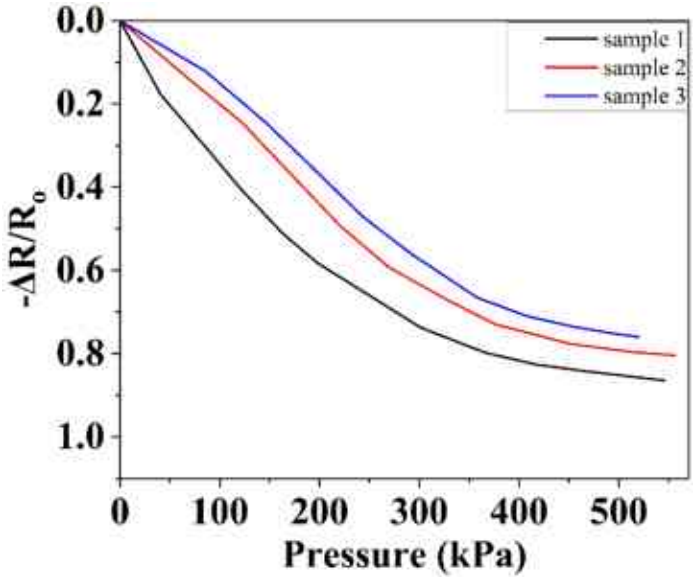

Figure 21. Applied pressure vs $\Delta R/R_o$ of sample 1, sample 2, and sample 3 in an N-BCNT-PU/SR pressure sensor.

The gauge factor (GF) is an important parameter for studying the performance of FPS, as it describes the change in resistance in response to strain. The GF is defined as the change in relative electrical resistance as a function of applied strain. The GF of the N-BCNT/PU-SR sensors was also determined according to the following equation:

$$GF = (\Delta R/R_o)/\varepsilon \quad (2)$$

where ΔR the resistance change, R_0 is the initial resistance, and ε is the strain. The $\Delta R/R_0$ increases monotonically with the applied pressure for all samples. As shown in Figure 22 and Table 8 the $\Delta R/R_o$ increases with the applied strain for sample 1, sample 2, and sample 3. However, sample 1 has greater GF, because high N-BCNT leads to lower initial resistance, resulting in a greater shift in $\Delta R/R_o$ under a given strain.

DOI: 10.14750/ME.2024.016

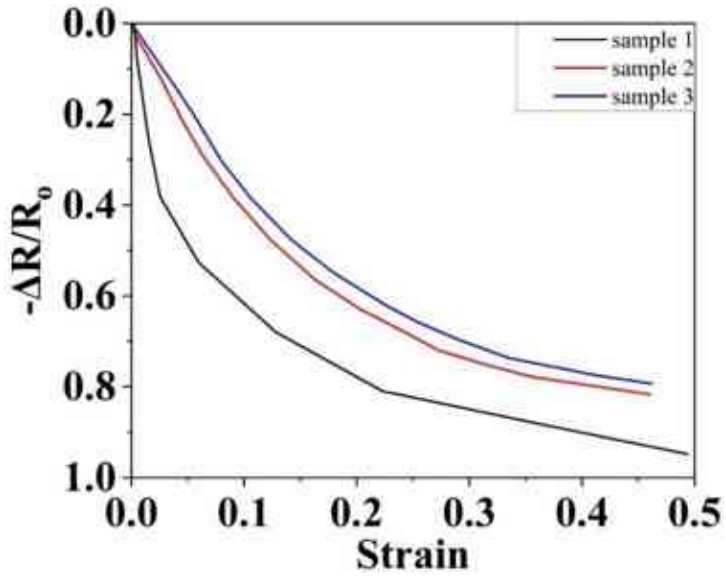

Figure 22. strain and the change in relative electrical resistance of sample 1, sample 2, and sample 3 in an N-BCNT-PU/SR pressure sensor.

Table 8. The gauge factor of N-BCNT /PU-SR pressure sensor samples in different pressure ranges

Samples	GF in strain range of 0.0-0.02	GF in strain range of 0.2-0.43
1	3.00	0.50
2	1.70	0.42
3	1.60	0.37

3.2.2 Stress-strain curve for N-BCNT-PU/SR flexible pressure sensor

The stress-strain curve of N- BCNT-PU /SR of sample 1, sample 2, and sample 3 is shown in Figure 23. The modulus for samples 1, 2, and 3 was measured to be 1.3 MPa, 1.2 MPa, and 1 MPa, respectively. The results show that sample 1, which has the highest N-BCNT loading, has a higher elastic modulus. This is due to the fact that N-BCNT is used for reinforcing the polymer matrix, and more N-BCNT leads to more improvement in the load transfer in the sensor due to the high strength and aspect ratio of N-BCNT [183] [184]. Furthermore, the unique characteristics of N-BCNT allow it to withstand high tension and compression, contributing to enhancing the

stiffness and subsequently improving the modulus of elasticity in the sensor that has higher concentrations of N-BCNT.

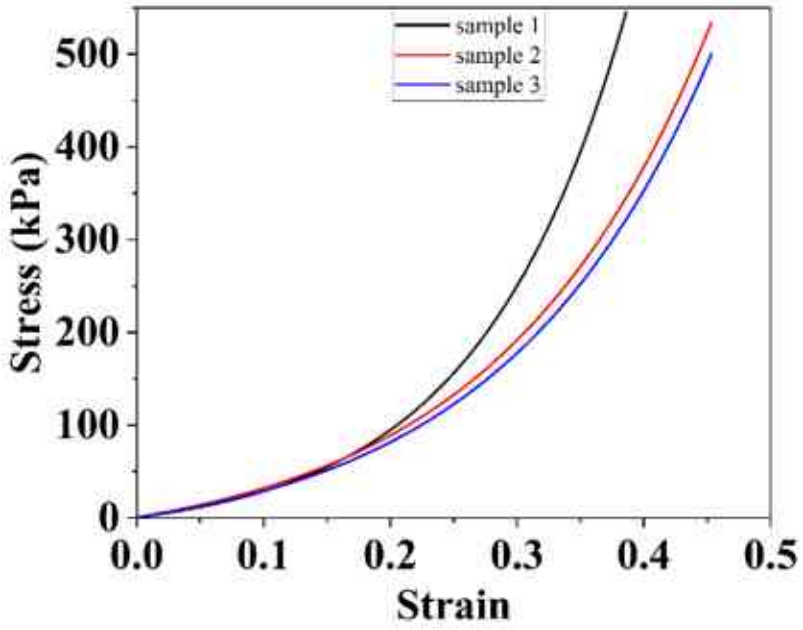

Figure 23. the stress-strain behavior of N-BCNT-PU/SR flexible pressure sensor for sample 1, sample 2, and sample 3)

3.2.3 Cyclic load test of N-BCNT-PU/SR flexible pressure sensor

Cyclic load testing is a crucial methodology for evaluating the performance of flexible pressure sensors. The technique involves the application of a series of cyclic loads and the measurement of the sensor's response over time, enabling the assessment of the sensor's durability, reliability, and overall performance under varying conditions[185]. The significance of this method is particularly relevant for flexible pressure sensors, as they are frequently utilized in applications that involve repeated loading and unloading, such as in wearable devices, medical implants, and industrial process control systems. By simulating real-world conditions in the laboratory, engineers and researchers can gain a more profound understanding of the sensor's performance in the field. Figure 24 investigated the repeatability and recoverability of nanocomposites using the N-BCNT-PU/SR flexible pressure sensor for sample 1, sample 2, and sample 3. The experiments comprised ramping up the pressure on the samples from 10 to 30 strain% and holding the pressure for two minutes after each cycle, under compressive loading and unloading conditions. The results of the study showed that the sensor had an outstanding ability to

DOI: 10.14750/ME.2024.016

detect signal outputs with different pressures. The cycles and peak amplitudes were uniform and stable after a few cycles for sample 1. However, for sample 2 and sample 3, stable peaks were only achieved after two and four cycles, respectively. The fluctuations and signal drifting observed in the first cycles when N-BCNT was present in the system at a lower concentration may be attributed to nano- or microcrack formation in the nanotube layers of the sensor. These results indicate that high N-BCNT loading leads to improved sensor performance under cyclic load [186]. This may be because carbon nanotubes create a more robust structure within the sensor, allowing it to sustain its performance under high pressures and cyclical loading conditions. The experiment highlights the significance of evaluating the concentration of N-BCNT in the development of flexible pressure sensors, as well as its potential impact on sensor performance under cyclic loading circumstances.

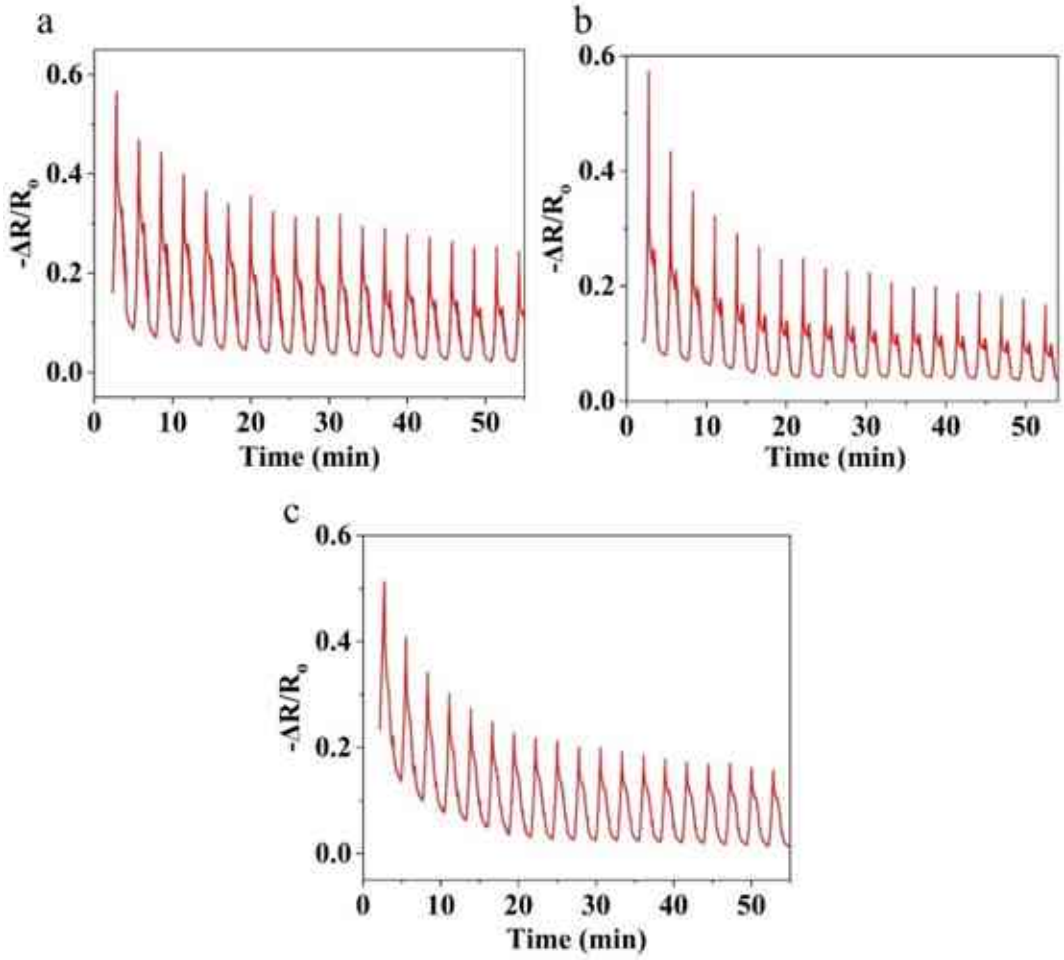

Figure 24. Cyclic load test for sample 1 (a), sample 2 (b), and sample (3) N-BCNT-PU/SR flexible pressure sensor.

DOI: 10.14750/ME.2024.016

3.2.4 Morphological Characterization of the N-BCNT-PU system and N-BCNT-PU/SR system

The structure and morphology of the N-BCNT/PU system have also been examined by optical microscopy and scanning electron microscopy as shown in Figure 25a and Figure 25b. The high quantity of micro-pores in PU has been validated with optical microscopy as well, and the surface area is high and fully covered by N-BCNTs. The PU skeleton displayed a wrinkled structure due to the presence of N-BCNT, which indicated that the nanotubes were attached to the foam through the dip-coating process. The SEM images confirmed that the PU structure has been coated successfully with N-BCNTs. Figure 25c and Figure 25d show the final pressure sensor and optical images of the N-BCNT-PU/SR flexible pressure sensor. PU acts as a supporting skeleton for the N-BCNT, which is responsible for creating a conductive path inside the insulator silicone rubber. The N-BCNTs serve as a 3D conductive network in the PU which will change its electrical features when pressure is applied to the system.

SEM was used to investigate the N-BCNT-PU/SR cross-section area (Figure 26a-f). These images offer a close-up view of the internal structure of the sensor, showing how SR filled in pores within N-BCNT/PU foam as seen in Figure 26a. This impregnation of silicone rubber creates a homogenous distribution of material throughout the PU foam structure, improving its mechanical properties. Figure 26b-c illustrates the distinct structural relationship between SR and N-BCNT/PU foam by way of element mapping. The orange color denotes carbon from N-BCNTs and PU, while purple denotes silicone. The element mapping offers a detailed view of the distribution of materials within a nanocomposite. Pores in the PU are filled with silicone rubber (Figure 26a-f), which serves primarily to increase the structural stiffness of the sensor. The filled PU pores by SR are due to a large number of micropores present in both PU and N-BCNTs coating, enabling SR to effectively fill those spaces. Overall, there was good adhesion among the constituents of this nanocomposite as evidenced by their performance under cyclic load. Furthermore, the SEM images provide visual proof of the internal structure of the N-BCNT-PU system, impregnation of SR inside the PU foam structure, and excellent adhesion between materials.

The N-BCNT-PU/SR cross-section area was studied using SEM (Figure 26a-f). These images provide a detailed examination of the internal structure of the sensor. The SR filled the pores of

DOI: 10.14750/ME.2024.016

the N-BCNT/PU foam as seen in Figure 26a. This impregnation of silicone rubber creates a homogenous distribution of the material throughout the PU foam structure, which improves the overall mechanical properties of the composite. The SR and the N-BCNT/PU foam can be clearly distinguished in two layers on the element mapping of the nanocomposite (Figure 26b,c). The orange color represents carbon (from N-BCNTs and PU), while the purple represents silicone. This element mapping allows for a clear understanding of the distribution of different materials within the composite. The pores of the PU are filled by silicone rubber (Figure 26 d-f), whose primary role is to improve the structural stiffness of the sensor. The filled PU pores by SR can be attributed to the high quantity of micro-pores in PU and N-BCNTs coating, which allows the SR to fill the pores effectively. Overall, good adhesion was detected among the constituents of the nanocomposite as observed in the performance of the samples under cyclic load. In addition, the SEM images provide visual evidence of the internal structure of the N-BCNT-PU system, the impregnation of the SR inside the PU foam structure, and the good adhesion of the materials.

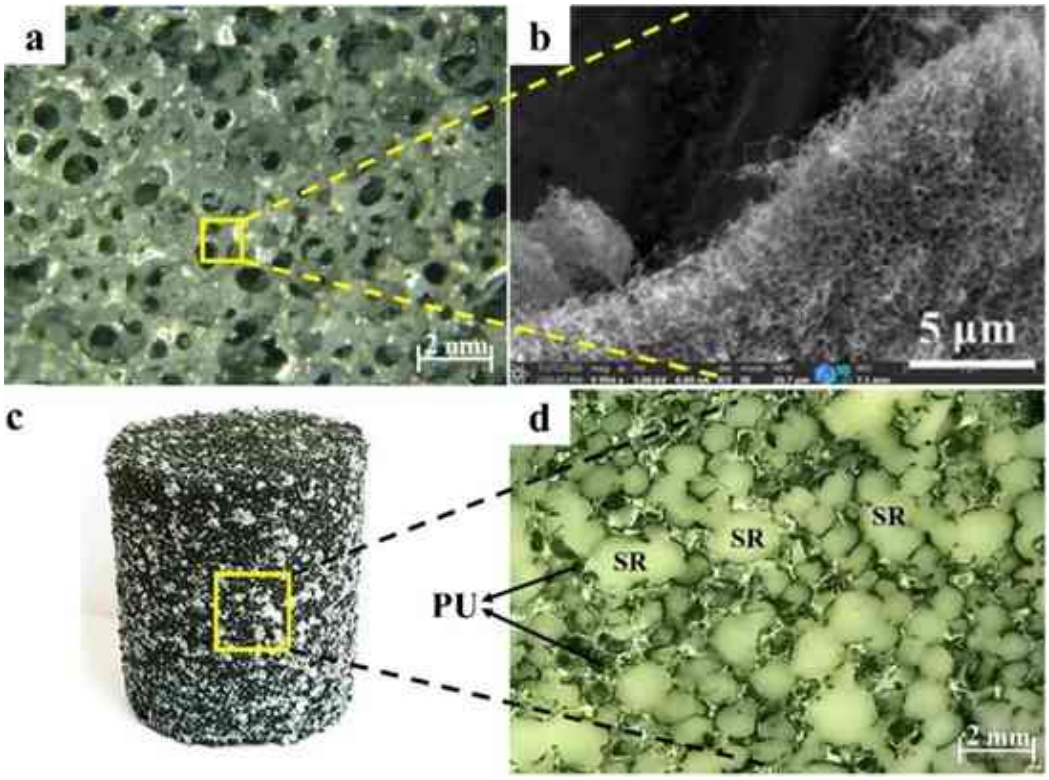

Figure 25. Examining the N-BCNT-PU system and final pressure sensor via optical microscopy and SEM revealed: an optical image of N-BCNT distribution on PU (a), SEM image of N-BCNT/PU(b) the final pressure sensor structure and silicone rubber impregnation within PU foam (c-d).

DOI: 10.14750/ME.2024.016

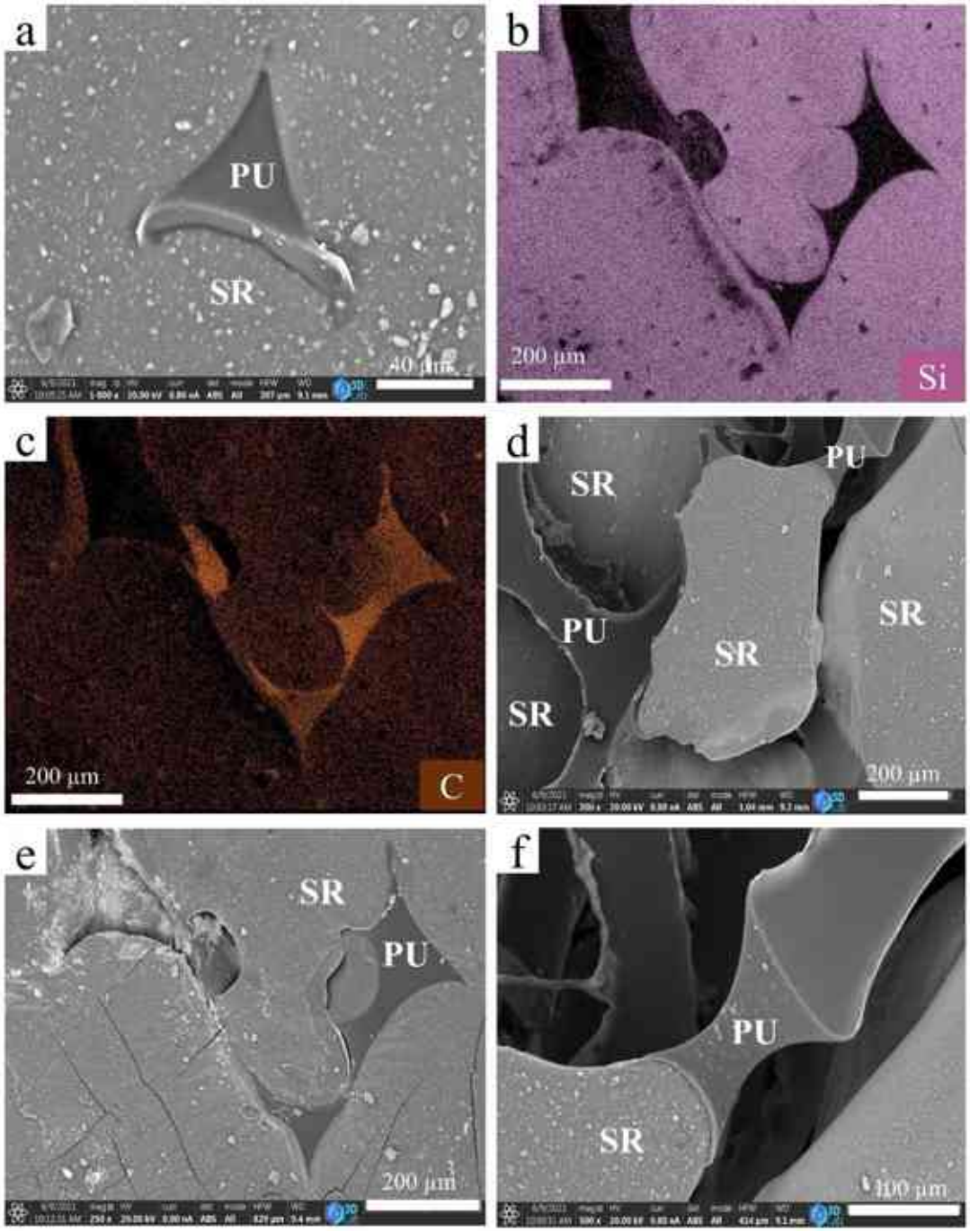

Figure 26. SEM images and mapping of a cross-section of N-BCNT-PU/SR flexible pressure sensor (a-f)

3.2.5 X-ray micro-CT characterization of the PU and N-BCNT/PU-SR

A pure PU foam sample was scanned with micro-CT to obtain a comprehensive understanding of its cell structure. This imaging approach provides the non-destructive mapping

DOI: 10.14750/ME.2024.016

of internal structures within a material, allowing for the examination of foam's porosity and pore size distribution. A micro-CT scan was used to map the cell structure of the pure PU foam. The applied scan plane was 8 µm on the upper half portion of the sample. The norm of the mapping plane is parallel to the sample's long axis. The scan indicates that the majority of the pores in the PU were open and available to be filled with silicone rubber (Figure 27a-d). Most of the pores (90%) are >50 µm, but <1000 µm, while the average diameter of the cells is 620 ± 329 µm. This finding is crucial as it indicates that silicone rubber may easily permeate PU foam. The capacity to fill PU foam pores with silicone rubber can be used to optimize the production of pressure sensors. Due to their porous structure and flexibility, PU foams are frequently utilized as the supporting skeleton for N-BCNT in pressure sensors. A greater number of open holes in the PU foam facilitates the entry of nanofillers, resulting in a more uniform dispersion of the filler throughout the foam. To optimize the performance and durability of the sensor, it is necessary to fill the pores with a substance that will not degrade with time. Filling the PU foam's pores with silicone rubber increases the sensor's durability and stability.

The N-BCNT/PU-SR were also characterized by using micro-CT scans (Figure 28a-f). The PU foam was the least filled in the case of sample 3 (air volume 5.6 vol%), while sample 2 was the one that was filled the most with silicone rubber (air volume 1.6 vol%). In the absence of silicone rubber, the nanotubes could be removed unintentionally from the N-BCNT/PU system when pressure was applied, as only van der Waals forces keep them together. However, when the N-BCNT-coated PU is impregnated with silicone rubber, the position of the nanotubes will be fixed and the structural integrity will be preserved during mechanical impact. These findings have significant implications for the manufacture of FPS with high performance. The utilization of N-BCNT/PU-SR could lead to the development of sensors that are more resilient and resistant to mechanical stress and impact.

DOI: 10.14750/ME.2024.016

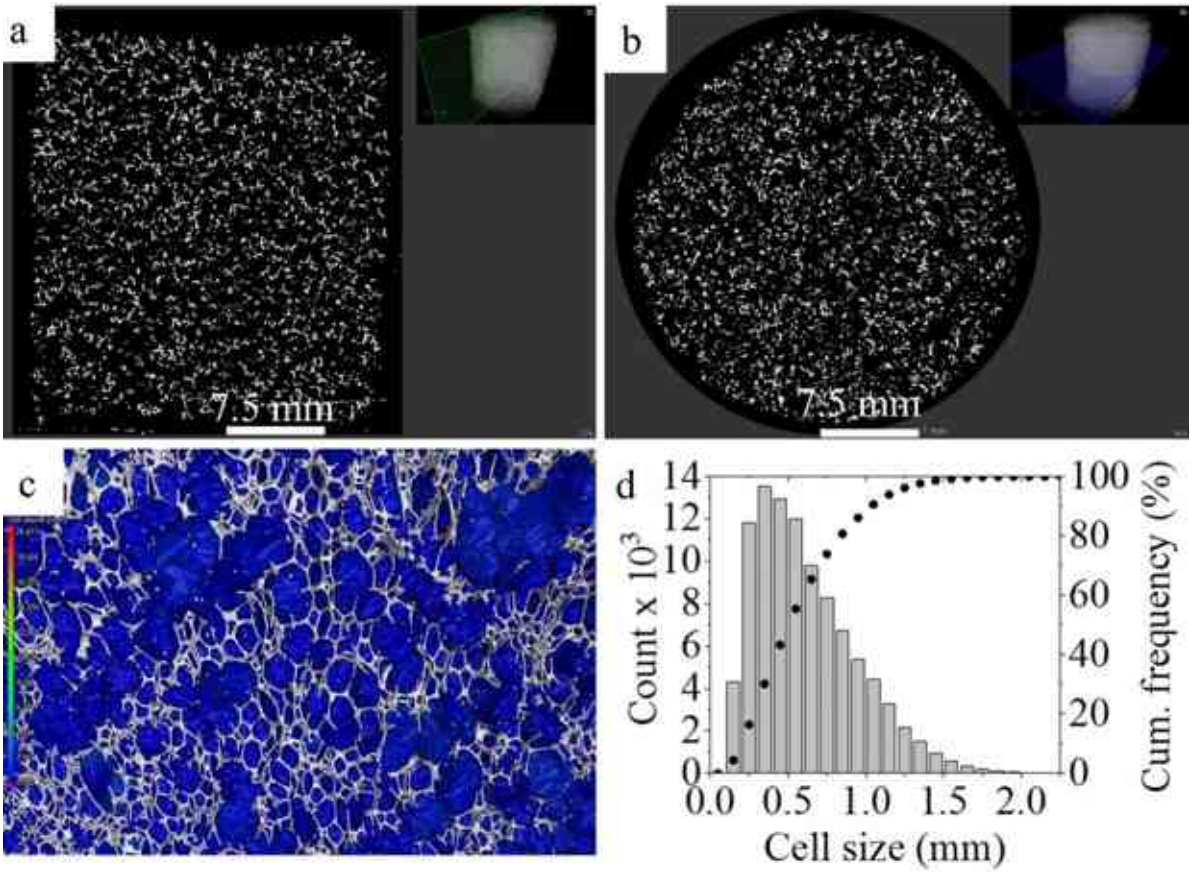

Figure 27. A micro-CT image of PU foam, depicting its vertical and horizontal location within the sample is shown in panels (a) and (b). Cell structure, represented by blue and grey colorations denoting pores and walls respectively, is highlighted. Furthermore, panel (c) displays cell size distribution within the foam (d).

DOI: 10.14750/ME.2024.016

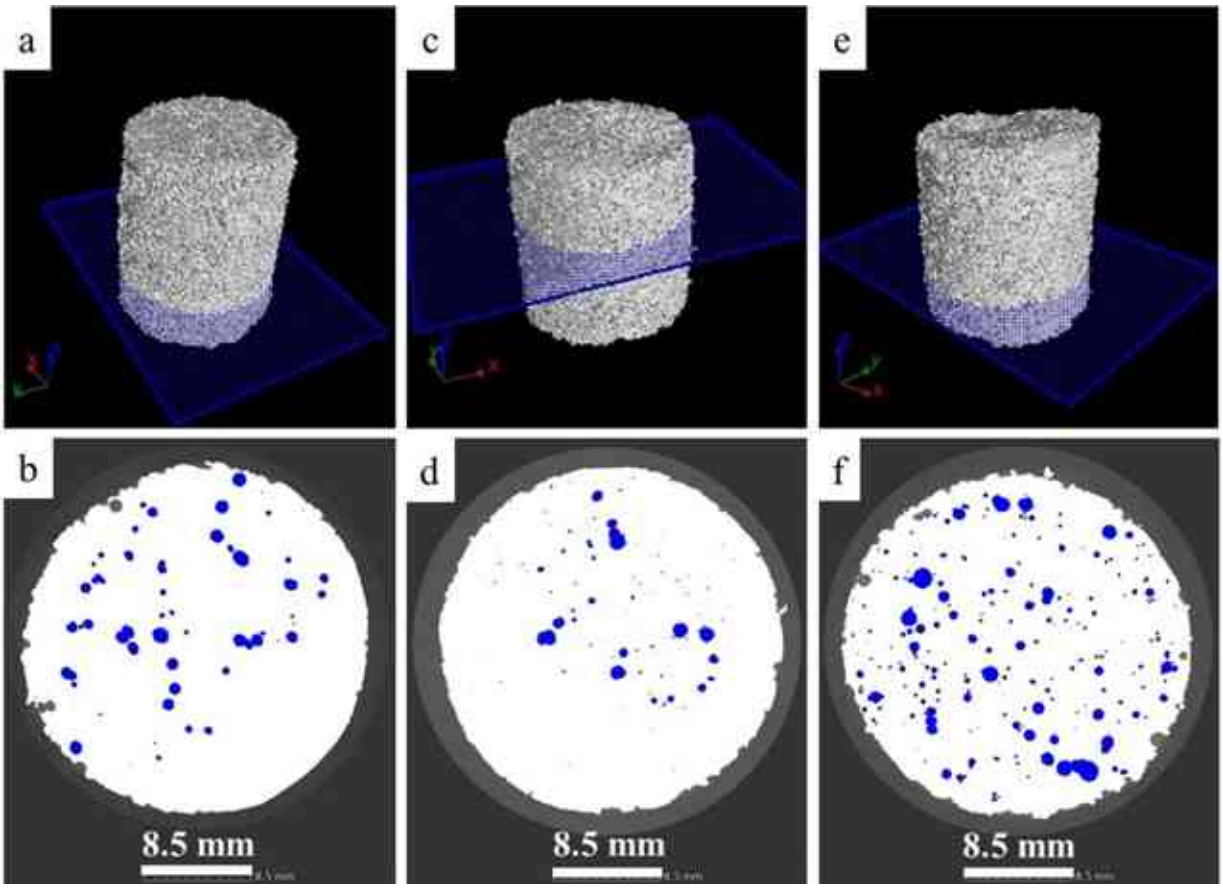

Figure 28. Micro-CT images of N-BCNT/PU-silicone rubber nanocomposites. Mapping plane and CT scan of sample 1(a,b), sample 2(c,d), and sample 3(e,f). White zones represent regions filled with silicone rubber; blue zones indicate no silicone rubber present.

3.2.6 Application of N-BCNT-PU/SR

As shown in Figure 29 a-b the N-BC/PUR pressure sensor show good performance in motion and finger touch detection. The sensor possesses exceptional piezoresistive and compressibility properties, making it well-suited for movement detection applications. To detect the motion and finger touch detection the sensor was placed between two electrodes and the electrical resistance signals were collected during the loading and unloading pressure sequence. The peak amplitudes were dependent on the amount of pressure applied on the sensor by the foot or finger recorded for each movement. These results prove the sensor has the potential to be developed and used precisely, and capable of detecting a wide range of motions owing to remarkable piezoresistive, electrical, and compressibility properties.

DOI: 10.14750/ME.2024.016

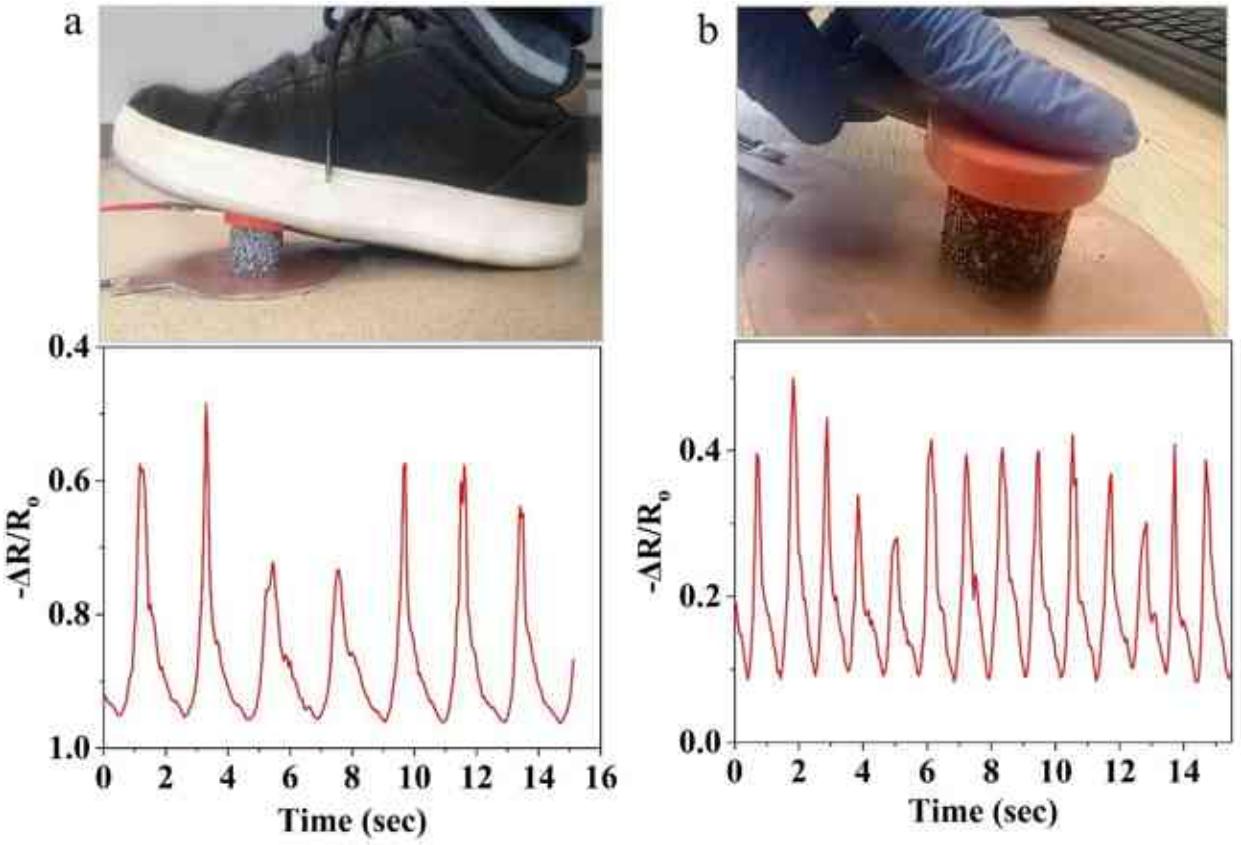

Figure 29. The various range of applications for N-BCNT-PU/SR, including motion detection (a) and finger touch detection (b).

3.4 N-BCNT: CB-PU/SR flexible pressure sensor evaluation

This section will discuss and analyze the N-BCNT: CB-PU/SR flexible pressure sensor as the manufacturing process displayed in section 2.3.4. The sensor uses a hybrid nanofiller with different mixing (5:5, 6:4, 7:3, 8:2, 9:1) of N-BCNT: CB ratios at fixed nanofiller loading to demonstrate the best mixing ratio for sensor performance. The results show that the optimal mixing ratio of 7:3 N-BCNT: CB performs better than another mixing ratio and N-BCNT alone. In addition, the surface morphology of the sensor was analyzed and its relationship with performance results was investigated.

3.4.1 Piezoresistive and electrical properties of N-BCNT: CB-PU/SR flexible pressure sensor

The electrical and piezoresistive properties of the prepared N-BCNT: CB/PU-SR hybrid nanofiller were measured. Each sensor contained an equal weight ratio of N-BCNT and CB (0.4%) with different mixing of (N-BCNT: CB 5:5, 6:4, 7:3, 8:2, and 9:1). In Figure 30, samples with N-BCNT: CB ratios of 5:5, 6:4, 7:3, 8:2 and 9:1 had initial electrical resistances of (446, 442, 308,

DOI: 10.14750/ME.2024.016

435, and 449) kΩ respectively. As expected, electrical resistance decreased when compressive pressure was applied to these same N-BCNT: CB/PU-SR samples. For example, when pressure is increased from 66 kPa to 75 kPa, the resistance drops from 150 kΩ to 100 kΩ. Such effects could occur as the distance between nanofillers decreases, creating more conductive paths and thus higher electrical conductivity. The electrical behavior is almost identical for samples with 5:5, 6:4, 8:2, and 9:1 N-BCNT: CB ratios. However, in the case of the sensor with a 7:3 NBCNT: CB ratio, electrical resistance significantly drops. Thus, this mixing ratio is optimum since electrical conductivity reaches its maximum due to the synergistic effect of nanofillers. By increasing the N-BCNT: CB ratio beyond 7:3, it becomes harder for N-BCNT to align and expand, while decreasing its relative amount of CB, leading to minimal contact between fillers. On the contrary, decreasing N-BCNT content reduces electrical charge transport over long distances along aligned and extended nanotubes [187]. Thus, even with its high aspect ratio, it may still not be possible for perfect conductive networks to form. CB can fill the gaps between N-BCNT to enhance electrical conductivity, leading to a decrease in resistance for the nanocomposite. Furthermore, this shows that nanotubes are essential in creating conductive networks; thus, N-BCNT forms the backbone for electrical conductivity within hybrid nanofillers, while CB further reinforces these areas [183]

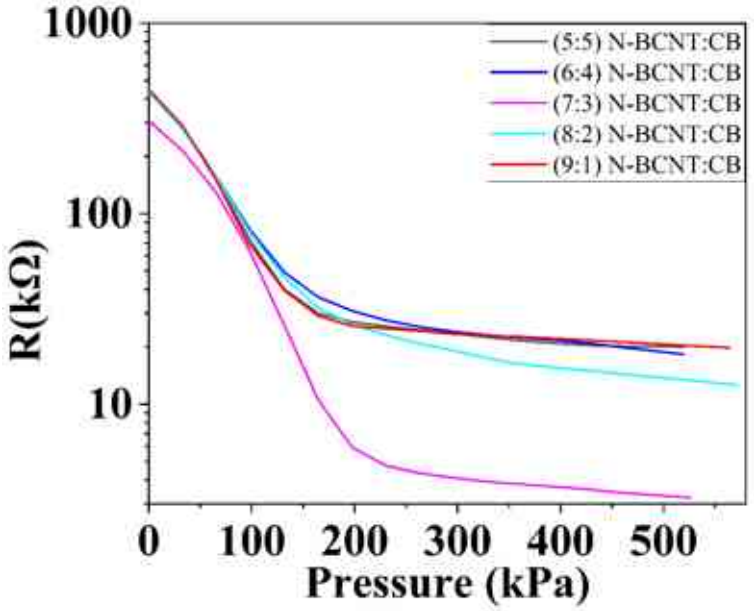

Figure 30. This graph displays the relationship between resistance and pressure for N-BCNT: CB-PU/SR composites with N-BCNT: CB mixing ratios of 5:5, 6:4, 7:3, 8:2, and 9:1.

DOI: 10.14750/ME.2024.016

As shown in Figure 31 and Figure 32, the S and GF value of N-BCNT: CB-PU/SR flexible pressure sensors was conducted. The $\Delta R/R_0$ increases monotonically with the applied pressure/strain for all samples. The S and GF are almost the same for the 5:5, 6:4, 8:2, and 9:1 N-BCNT: CB/PU-SR sensors (Table 9). However, the sample with 7:3 N-BCNT: CB ratio has the highest S and GF, because this sensor has the lowest initial resistance. Here, the low initial resistance plays a crucial role in changing the relative resistance during pressure/strain application. Therefore, compression of the sensor would cause a rapid change in relative resistance. All in all, it can be concluded that the 7:3 N-BCNT: CB sensor has good overall performance in both low and high pressure/strain ranges. This may be due to the synergistic effect of the N-BCNT and CB nanofillers, which could interact in a manner that enhances the overall performance of the pressure sensor. The specific properties of N-BCNT and CB, such as their electrical conductivity, surface area, and mechanical strength, may also contribute to the observed improvement in GF at this mixing ratio. The ratio of the two nanofillers may also affect the distribution and orientation of the nanofillers within the silicone rubber matrix, which could influence the sensor's performance.

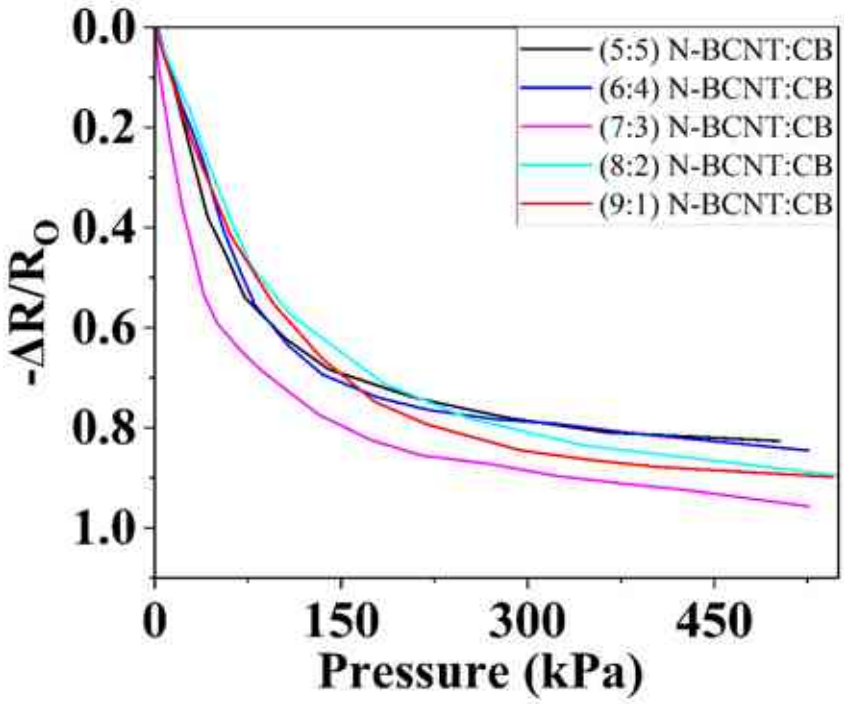

Figure 31. This figure illustrates the relationship between applied pressure and changes in relative electrical resistance (ΔR/Ro) for a (5:5, 6:4, 7:3, 8:2, 9:1) N-BCNT: CB mixing ratio in an N-BCNT-PU/SR flexible pressure sensor.

DOI: 10.14750/ME.2024.016

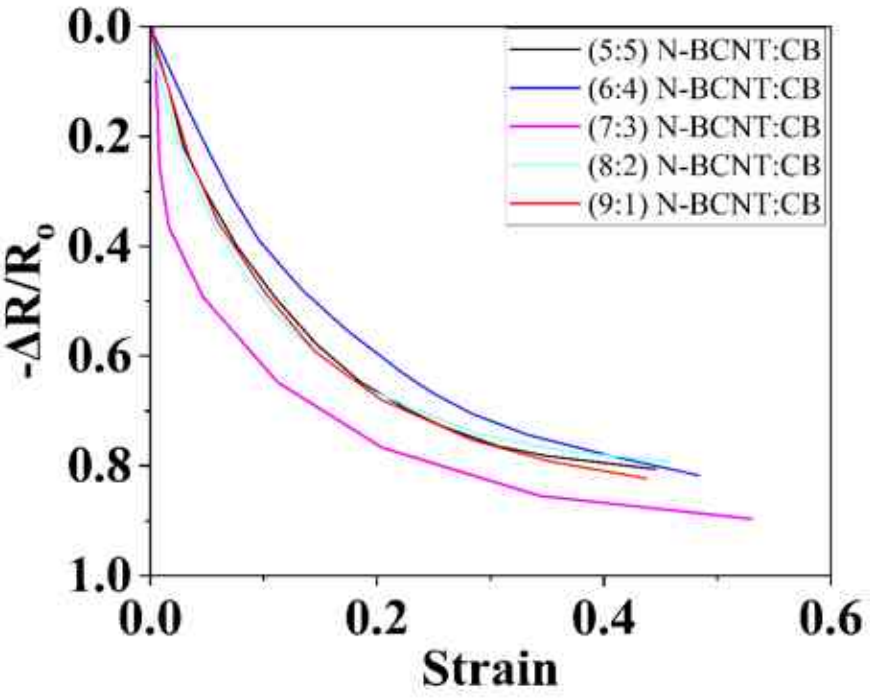

Figure 32. The relationship between strain and the change in relative electrical resistance ($\Delta R/R_o$) of (5:5, 6:4, 7:3, 8:2, 9:1) N-BCNT: CB mixing ratio in an N-BCNT-PU/SR pressure sensor.

Table 9. The *S* and GF N-BCNT: CB/PU-SR pressure sensor samples in different pressure and strain ranges

N-BCNT: CB mixing ratio	***S* in the range of 0-75 kPa^{-1}**	***S* in the range of 179-525 kPa^{-1}**	**GF in strain range of 0.000-0.018**	**GF in strain range of 0.14-0.43**
5:5	$7.8*10^{-3}$	$2.9*10^{-4}$	5.00	0.59
6:4	$7.1*10^{-3}$	$2.9*10^{-4}$	4.00	0.40
7:3	$1.3*10^{-2}$	$4.0*10^{-4}$	25.00	0.69
8:2	$5.4*10^{-3}$	$3.6*10^{-4}$	4.67	0.49
9:1	$5.7*10^{-3}$	$3.0*10^{-4}$	4.70	0.60

DOI: 10.14750/ME.2024.016

3.4.2 Cyclic load test of N-BCNT: CB/SR flexible pressure sensor

The repeatability under compressive loading and unloading was investigated (Figure 33). The strain ramped from 10% to 30%, with a hold time of two minutes after each cycle. The samples were tested under these conditions to evaluate the performance and stability of the pressure sensor. The samples are tested in twenty compression cycles with a hold time of two minutes after each cycle. The relative electrical resistance decreased with increasing pressure and returned to baseline after the pressure was removed. The signal drift in the 1-3 cycles may be related to the CB and N-BCNT layers being significantly damaged at high pressure due to the increasing distance between the adjacent carbon nanofillers. These defects can disrupt the electrical conductivity of the composite, leading to a drift in the signals. The presence of microcracks may be more likely to occur during cyclic loading, as the repeated stressing of the material can lead to the formation of cracks. With the addition of CB particles, the N-BCNT network becomes more compact and forms a more stable hybrid conductive network. During compression, the CB nanoparticles can repair the damaged N-BCNT pathways by filling the gaps between the nanotubes, which is due to their greater mobility in the polymer matrix [186]. In general, the excellent recoverability and repeatability of the pressure sensors are due to the extreme flexibility of SR and the ability of the hybrid nanofillers to establish conductive networks.

DOI: 10.14750/ME.2024.016

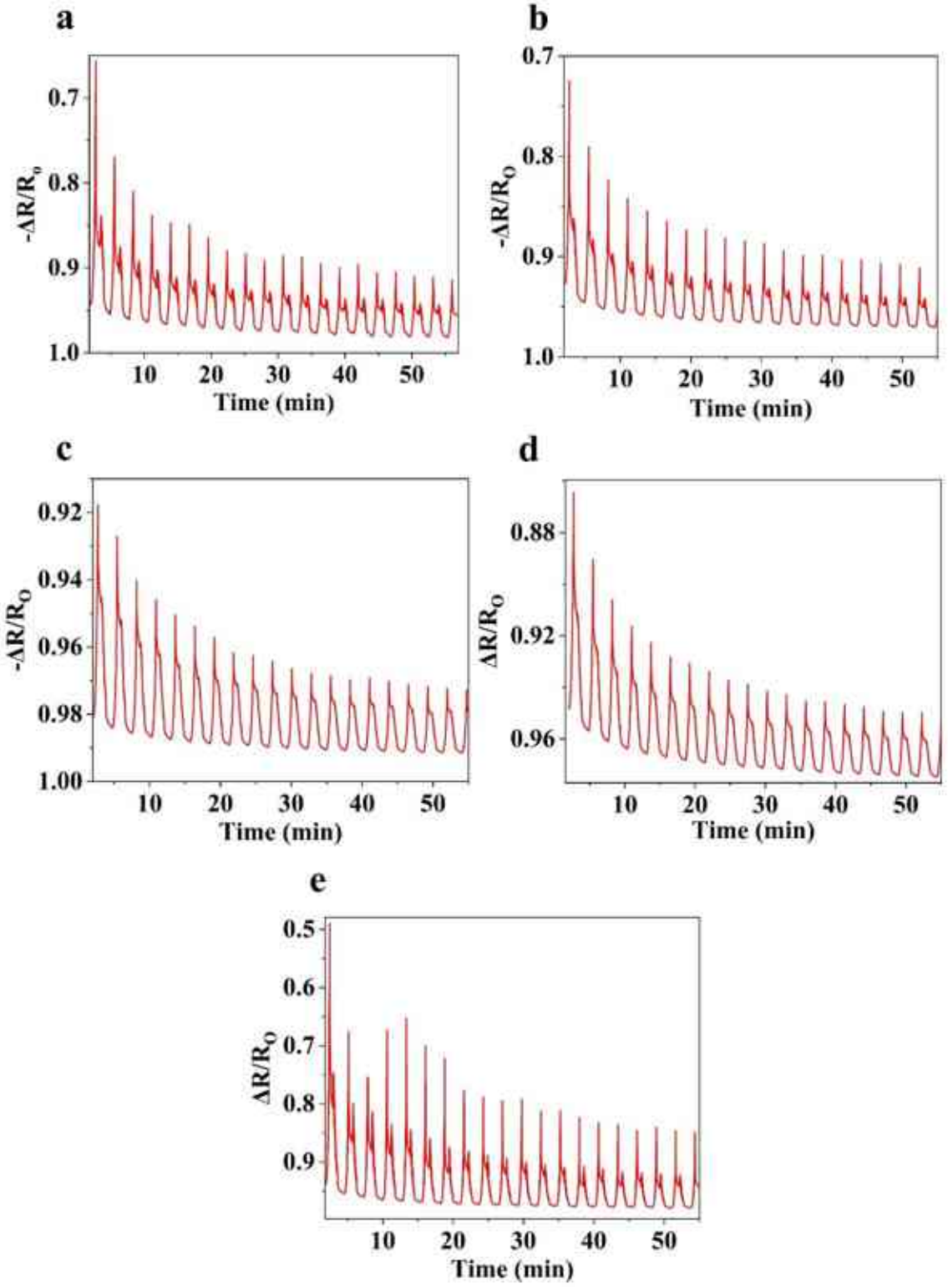

Figure 33. Cyclic load tests of the N-BCNT: CB/PU-SR pressure sensors with different N-BCNT: CB ratios of 5:5 (a), 6:4 (b), 7:3 (c), 8:2 (d), and 9:1 (e).

DOI: 10.14750/ME.2024.016

3.4.3 Stress-strain curve for N-BCNT: CB/SR flexible pressure sensor

The results for pressure and strain show that the behavior of all samples is similar, and the pressure for all samples is in the range of 495-573 kPa below the applied strain (Figure 34). This similarity could be related to the stability and robustness of the conductive nanofiller network in the sensors. The addition of N-BCNT: CB improves the electrical conductivity and stability of the sensors, resulting in similar mechanical behavior. Moreover, the ratio of N-BCNT to CB has been shown to have little effect on the stress-strain behavior of the conductive sensor network compared to its overall stability. Thus, the mechanical properties of the samples remain similar despite the changes in the ratio of N-BCNT to CB.

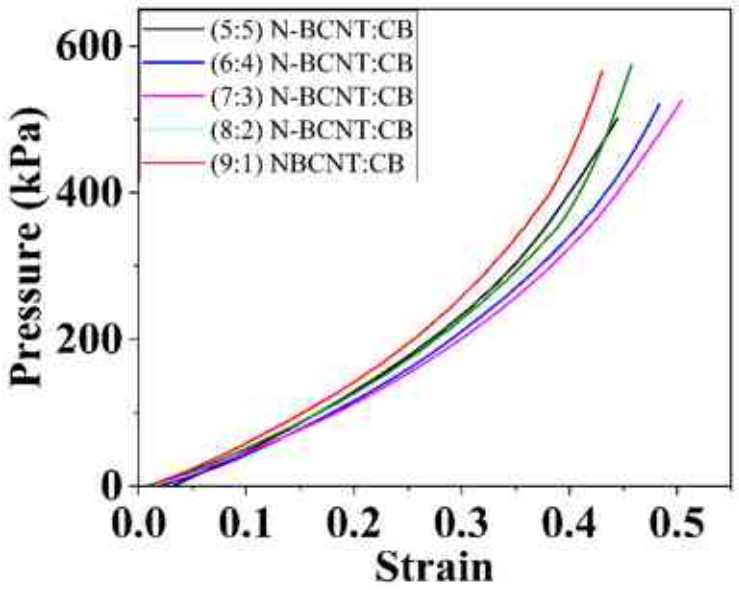

Figure 34. Stress vs strain curve to N-BCNT: CB/SR for different mixing ratios (5:5, 6:4, 7:3, 8:2, 9:1) N-BCNT: CB.

3.4.4 Morphological characterization of the N-BCNT: CB/PU-SR system

The morphology of the pressure sensor and dispersion state of the nanofiller were evaluated by SEM for 7:3 N-BCNT: CB samples as shown in Figure 35. The PU skeleton shows a wrinkled surface due to the incorporation of N-BCNT and CB (Figure 35 a). Indicating that the N-BCNT and CB were bonded to the foam by the dip coating process. At higher magnification, the nanofiller coating on the PU structure is visible, and the CBs are close to the N-BCNT which leads to the formation of a synergistic conductive network (Figure 35 b). This hybrid nanofiller can efficiently improve the piezoresistive performance of nanocomposites ([188] by creating a grape-cluster-like

DOI: 10.14750/ME.2024.016

between N-BCNT and CB (Figure 35 c-d) [187]. CB acts as a bridging point between N-BCNTs and would improve electrical conductivity and pressure sensitivity. As it is shown on the cross section of the 7:3 N-BCNT: CB/ PUSR sensor, the SR fills the pores of PU (Figure 35 e). In addition, the SR and the N-BCNT: CB/PU can be clearly distinguished into two layers on the elemental mapping of the nanocomposite (Figure 35 f). The green color represents N-BCNT and CB, which were deposited onto the surface of PU, while the purple color represents silicone.

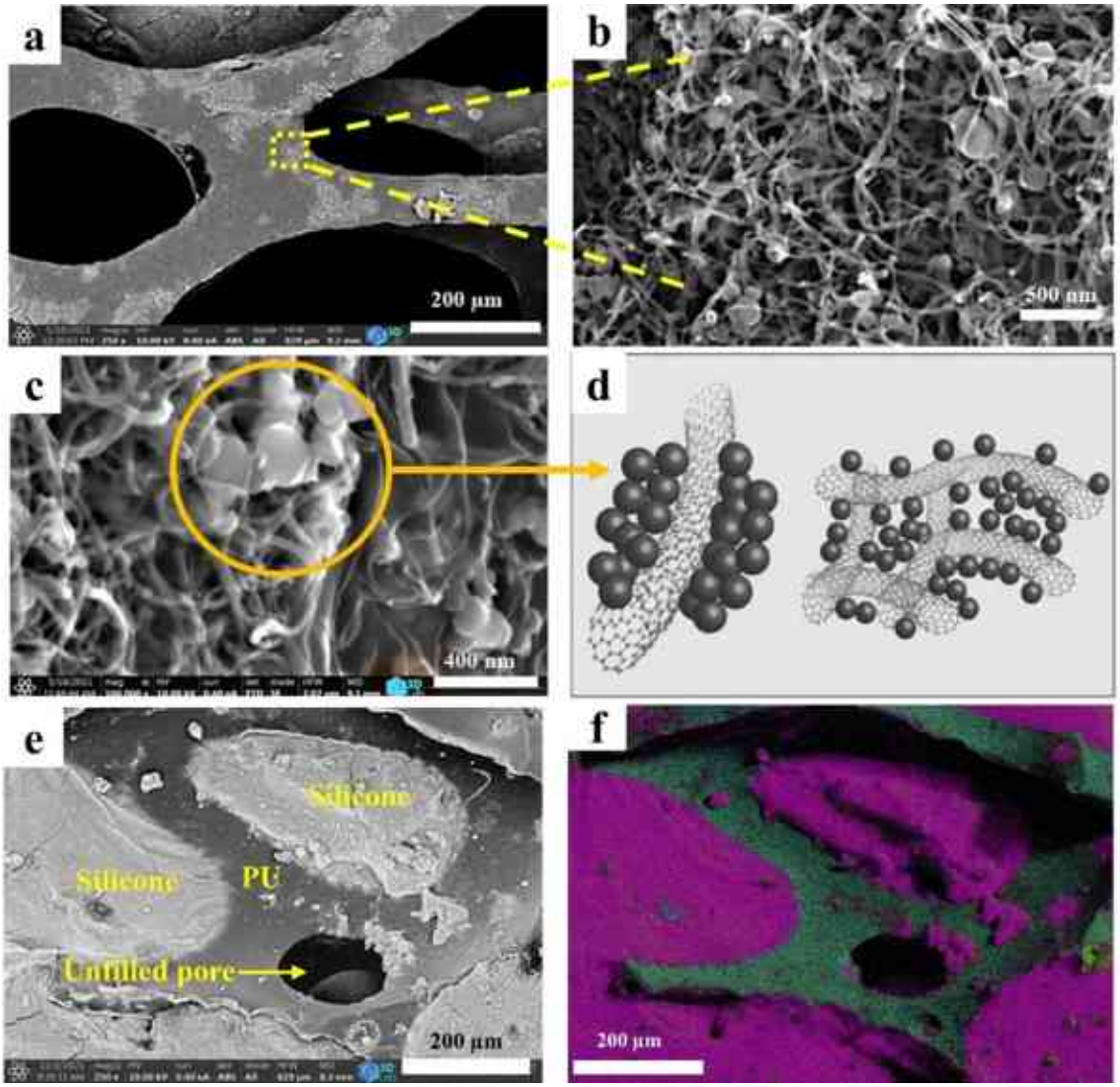

Figure 35.SEM image of the dispersed N-BCNT: CB on the PU skeleton (a-b), nanofiller coating of PU and the grape-cluster-like model of the hybrid N-BCNT: CB nanofiller (c-d), cross-section and elemental mapping of the N-BCNT: CB/PU-SR sensor (e-f).

DOI: 10.14750/ME.2024.016

All in all, good adhesion was observed between the components of the nanocomposite, which is clearly reflected in the performance of the sensor. Overall, the SEM analysis of the pressure sensor provides insight into the morphology and dispersion state of the nanofiller, which is crucial for understanding the performance of the sensor.

3.4.5 Structural analysis of the PU and the N-BCNT: CB/PU-SR pressure sensor

A micro-CT was used to map and characterize the cell structure of the pure PU foam and the N-BCNT: CB/PU-SR nanocomposites (Figure 36). The size of 90% of the total pores ranged from 50 to 1000 mm, and the average cell diameter was 620 ± 329 mm. These results show that the pure PU foam exhibited a high degree of open porosity, which is beneficial for the subsequent impregnation of SR.

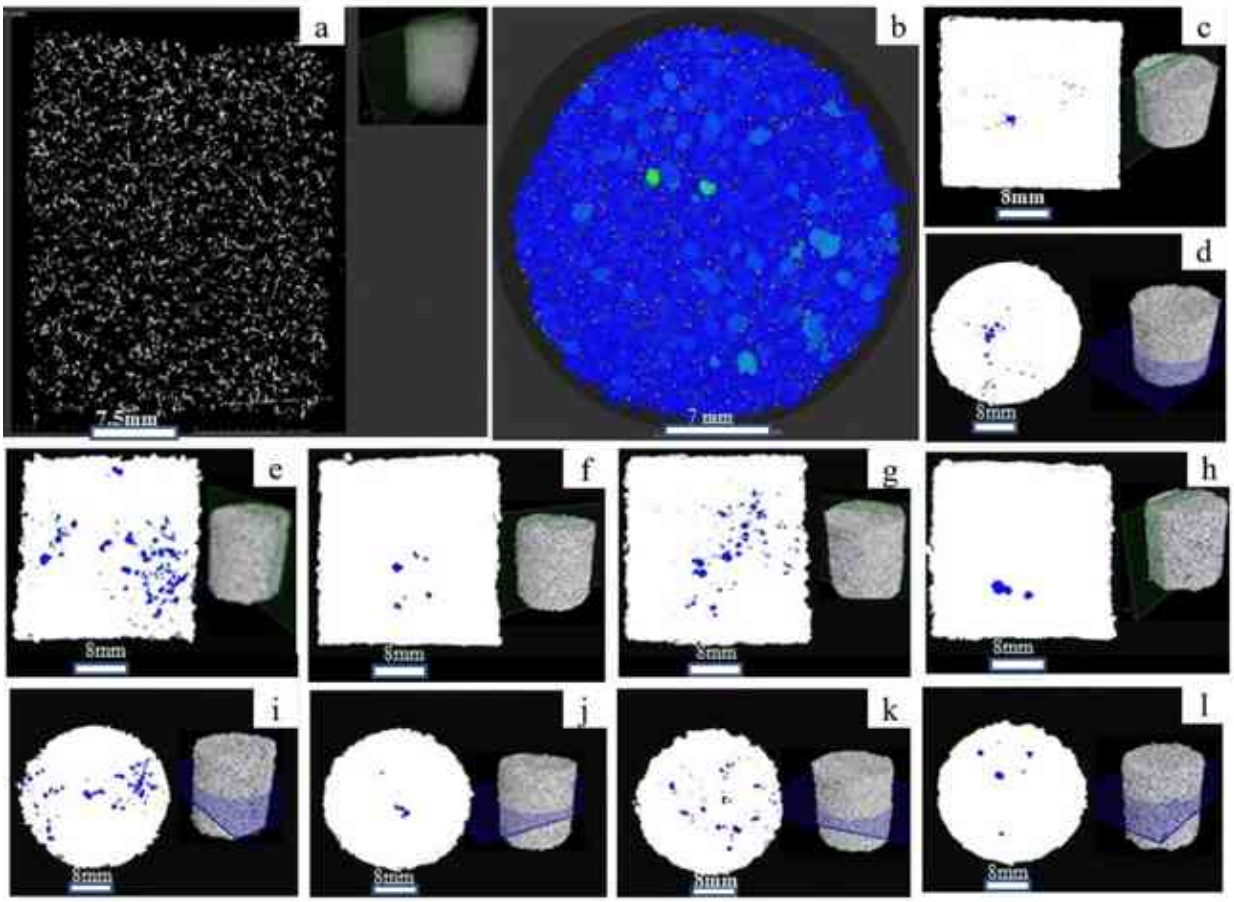

Figure 36. Horizontal and vertical mapping of CT plane position of pure PU (a-b), and the N-BCNT: CB/PU-SR flexible pressure sensors with different N-BCNT: CB ratios of 5:5 (c,d), 6:4 (e, i), 7:3 (f, j), 8:2 (g, k), and 9:1 (h, l).

Furthermore, the volume of the pressure sensors that were not filled with SR was also evaluated (Figure 36 c-j and Table 10). The white areas refer to the PU foam filled with SR and the blue areas refer to PU, which is not filled with silicone rubber. In general, only a small portion of the total volume is not filled with SR which does not affect the applicability of the sensors. By using a better vacuum during the preparation, the volume without SR could be further decreased. If pressure is applied to the N-BCNT: CB/PU system in the absence of SR, the nanofiller may be unintentionally removed. This is because only van der Waals forces hold the system together. However, by applying SR, the position of the nanofiller is fixed and the structural integrity of the sensor is maintained.

Table 10. Volume % of pressure sensors which is not filled with SR.

Pressure sensors	vol%
5:5 N-BCNT:CB/PU-SR	1.0
6:4 N-BCNT:CB/PU-SR	3.2
7:3 N-BCNT:CB/PU-SR	1.7
8:2 N-BCNT:CB/PU-SR	2.2
9:1 N-BCNT: CB/PU-SR	1.2

3.4.5 Application of N-BCNT: CB/SR flexible pressure sensor

The N-BCNT: CB/SR flexible pressure sensor demonstrates excellent repeatability and sensitivity, making it well-suited for monitoring human activity (Figure 37 a-b). It can successfully record different pressure levels for various activities, such as motion detection, and finger touch detection. To measure the movement (or step-counter) and detect finger touch, the pressure sensor was placed between two electrodes and the relative change in resistance was recorded during the pressure sequence of loading and unloading. The relative change in the resistance of the sensor was due to the tunneling of the resistance between the nanofillers and the loss of the connections between them. The peak amplitudes are indicated by the amount of pressure applied to the sensor during each movement with the finger or foot. Overall, these flexible pressure sensors have the potential to enable various touch and motion detection applications in a wide range of fields, from consumer electronics to healthcare.

DOI: 10.14750/ME.2024.016

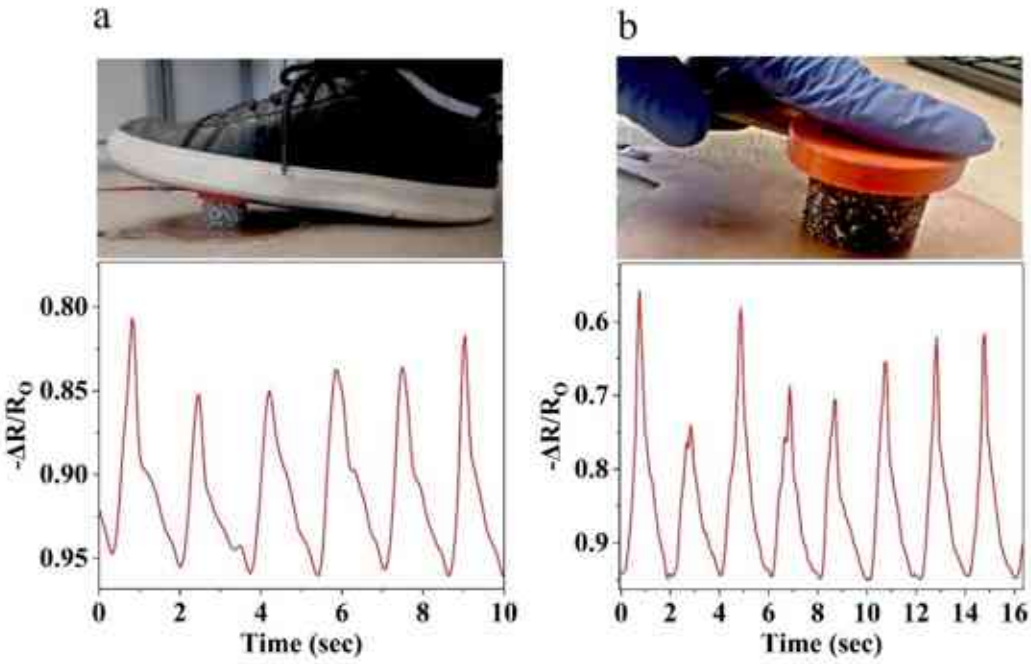

Figure 37. The application of 7:3 N-BCNT: CB/PU-SR sensor in motion and finger touch detection (a-b).

3.5 N-BCNT-PU flexible pressure sensor evaluation

This section will discuss and analyze the N-BCNT-PU flexible pressure sensor as the manufacturing process displayed in section 2.3.5. Three different PU foams were prepared by mixing commonly used isocyanate and polyol with different isocyanate indices (1.0:0.8, 1.0:1.0, 1.0:1.1) to create PU foam samples with different pore volumes (Table 6). The PU was then coated with by dip coating the same N-BCNT percentage for all samples to study the effect of varying pore volumes on pressure sensor performance while keeping other parameters constant like the type of nanofiller added, and without impregnation in silicone rubber. By precisely adjusting the pore volume while fixing all other parameters constant, the influence of pore volume on the performance of the pressure sensor may be measured with increased precision and reliability. By changing the pore volume of PU foam, the outcomes of these studies will provide useful insights into enhancing the performance of pressure sensors.

3.5.1 Piezoresistive and electrical properties of N-BCNT-PU flexible pressure sensor

The changes in electrical resistance of the N-BCNT/PU flexible pressure sensors were investigated as a function of compression pressure (Figure 38). The results show that the electrical resistance decreases as the applied compression pressure increases. This could be related to the

DOI: 10.14750/ME.2024.016

fact that the distance between the N-BCNTs becomes smaller, resulting in a more electrically conductive pathway in the PU system. In addition, the change in the initial resistance of the samples is also recorded (Figure 38). The initial resistance was 310 in the case of sample 1 to 1034 and 5200 in the case of sample 2 and sample 3, respectively. This phenomenon indicates that the volume of the pores is a critical factor and can drastically change the resistance. Therefore, the pore volume of the samples (Figure 39) was examined using the Micro-CT instrument to investigate the relationship between pore volume and resistivity values. The total pore content of sample 1, sample 2, and sample 3 are 91.6, 85.3, and 78.1 volume percent, respectively. The most interesting result is that a sensor with larger pores has lower electrical resistance. This can be explained by the fact that the larger the pores, the smaller the total PU scaffold, and density. Consequently, more N-BCNTs are interconnected, resulting in more conductive paths and a larger effective conductive area across the PU scaffold. As can be clearly seen in Figure 39, the plateau is described by a progressive compressive deformation at a relatively constant compressive stress due to the elastic buckling of the PU scaffold[189][190]. The plateau region appears clearly in the ranges of 9-17 kPa and 7-14 kPa for sample 2 and sample 3, respectively (Figure 38).

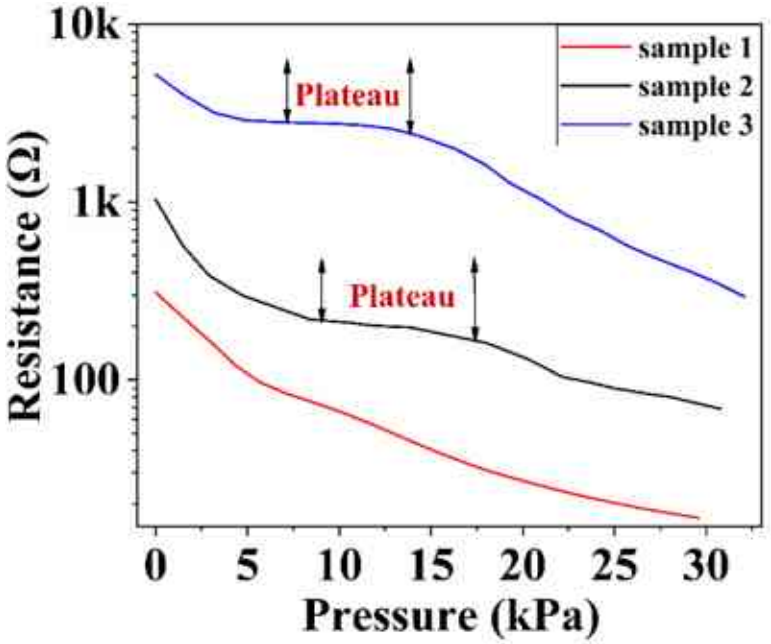

Figure 38. Resistance vs. pressure plots of the N-BCNT/PU composite (sample 1, sample 2, and sample 3).

DOI: 10.14750/ME.2024.016

On the other hand, there is no clear plateau for sample 1, which means that PU provides a suitable spatial for the elastic deformation of the foam due to its large pore volume. These results are useful in the improvement of flexible pressure sensor performance by adjusting the pore volume of PU foam and demonstrating the relationship between the electrical resistance value and the pore volume of the samples.

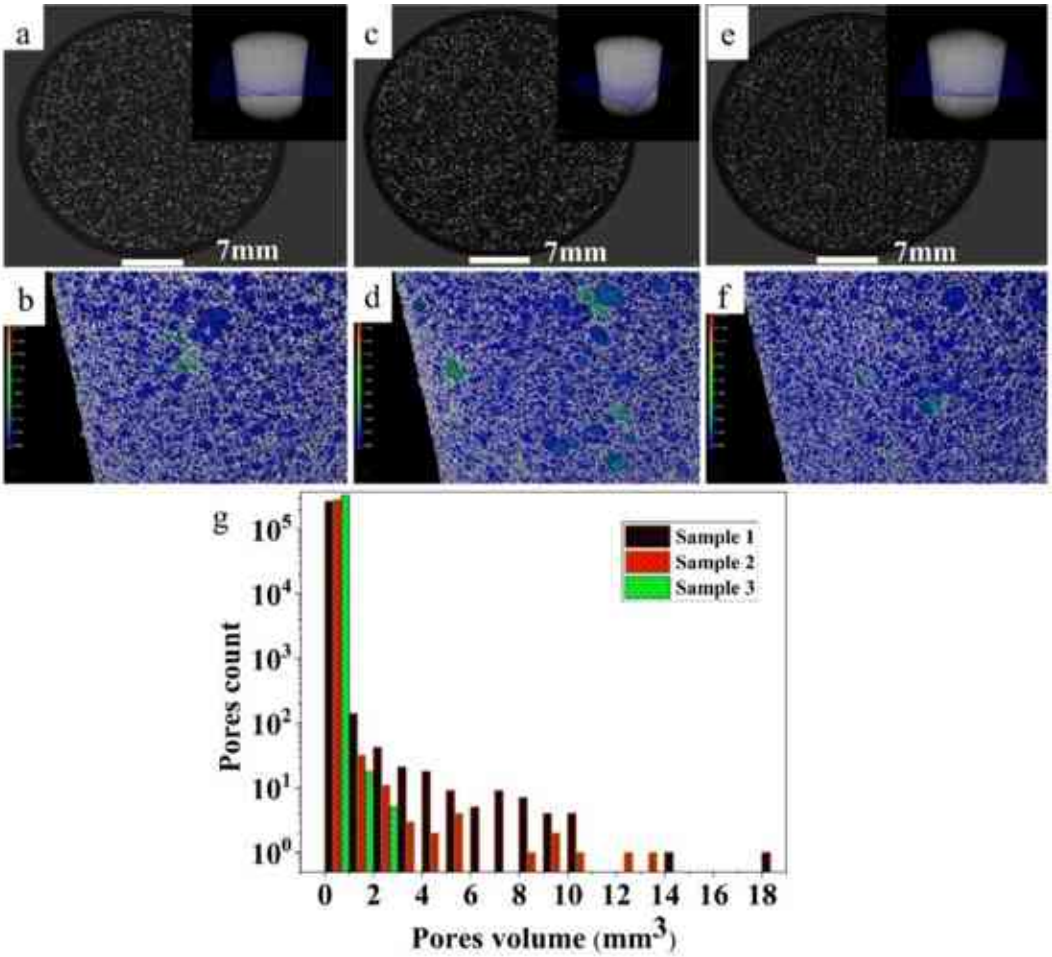

Figure 39. Micro-CT mapping plane and images of sample 1 (a-b), sample 2 (c-d), and sample 3 (e-f) along with the pore volume distribution (g).

As shown in Figure 40 and Table 11 the pressure sensitivity of the N-BCNT/PU flexible pressure sensor was measured in the range (0-30) kPa. The pressure sensitivity was calculated by using Equation 1. In the range (0-15) kPa sample 1 revealed higher pressure sensitivity than sample 2 and sample 3. Such phenomena could be related to sample 1 having a lower initial resistance. Therefore, high changes in the resistance in response to the applied pressure led to a large variation in pressure sensitivity. On another hand, sample 3 possesses a greater initial resistance than

samples 1 and 2. Consequently, it is not particularly sensitive to tiny pressure variations (0–15 kPa). However, at higher pressures (15–30 kPa), sample 3 exhibits larger changes in the electrical resistance in pressure variation, yielding a larger change in resistance value and, hence, a larger pressure sensitivity value.

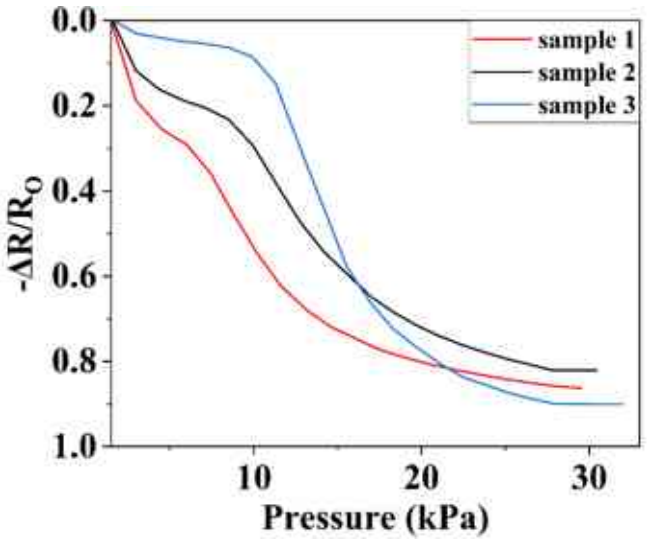

Figure 40. The change in relative resistance vs pressure of N-BCNT-PU for sample 1, sample 2, and sample 3.

Table 11. The S and GF of all samples are in different pressure and strain ranges.

Samples	S in Pressure Range 0–3 kPa^{-1}	S in Pressure Range 6–15 kPa^{-1}	S in Pressure Range 16–30 kPa^{-1}	GF in Strain Range (0.00–0.08)	GF in Strain Range (0.18–0.27)	GF in Strain Range (0.27–0.57)
Sample 1	0.12 kPa^{-1}	0.05 kPa^{-1}	0.008 kPa^{-1}	3.17	2.87	0.58
Sample 2	0.08 kPa^{-1}	0.04 kPa^{-1}	0.017 kPa^{-1}	1.68	3.91	1.09
Sample 3	0.02 kPa^{-1}	0.09 kPa^{-1}	0.019 kPa^{-1}	0.75	4.58	1.27

The GF is represented by the slope of the curve between relative change in resistance and strain, as shown in Figure 41. The gauge factor was calculated according to Equation 2. The gauge factor in the strain range of 0.00–0.25 for sample 1 is higher than that of samples 2 and 3 (Table 11). As mentioned above, sample 1 has a high pore volume. Therefore, this phenomenon could be related to the fact that the increase in $\Delta R/R_o$ at a low compressive strain is mainly determined by the interconnection of the pores, which leads to the formation of a more effective conductive

DOI: 10.14750/ME.2024.016

structure. In the strain range of 2.5–0.6, sample 3 has the highest GF compared to samples 2 and 1. This phenomenon could be related to the fact that at high compressive strain, the PU foam becomes denser, and the contact area increases. Hence, the sensor with the smaller pore volume (sample 3) plays a crucial role in reducing the $\Delta R/R_o$ of the foam structure.

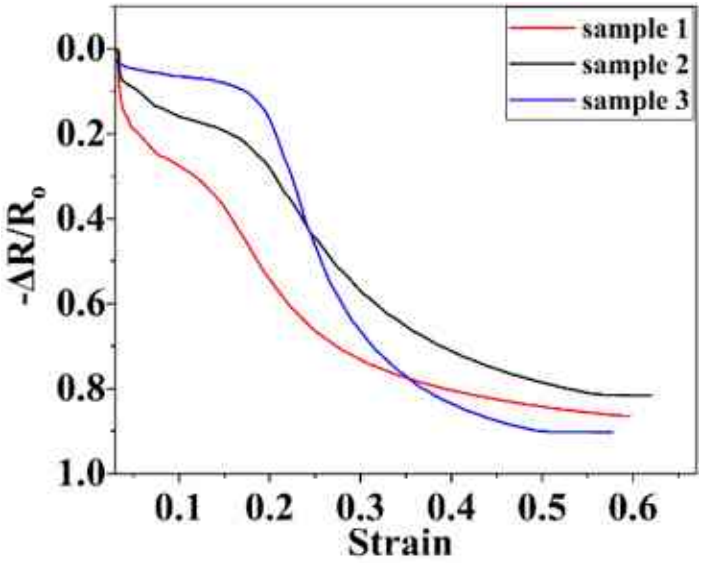

Figure 41. The relative change in resistance vs strain of N-BCNT-PU for sample 1, sample 2, and sample 3.

The corresponding stress–strain curves were also recorded for the prepared sensors (Figure 42). The compressive modulus of the sensors is 0.064, 0.095, and 0.15 MPa for sample 1, sample 2, and sample 3, respectively. Such results correspond to the high pore volume of sample 1, which makes the stiffness decrease. Moreover, the compressive strength is also improved by increasing the isocyanate content. Thus, the compressive strength of the PU foam can be improved by increasing the isocyanate index. These results support the idea that decreasing the diisocyanate content leads to an increase in the total pores of the PU foam.

DOI: 10.14750/ME.2024.016

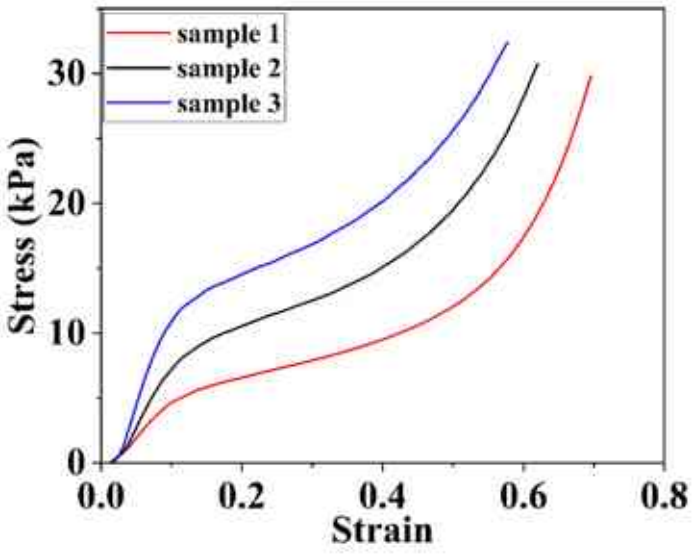

Figure 42. Stress-strain curve of N-BCNT/PU for sample 1, sample 2, and sample 3

3.5.2 Cyclic load of N-BCNT-PU composite

To investigate the repeatability and recoverability of the sensors, a cyclic load was applied to them as shown in Figure 43. The pressure on the N-BCNT/PU nanocomposite sensors was repeatedly increased and removed at two-minute intervals for 55 min with a ramp of 10% to 30%. The samples show different behavior in terms of output signal stability and peak amplitude. There are several fluctuations and a gradual increase in peak amplitude over time in sample 1 and sample 2 compared to sample 3. Sample 1 has a large pore volume and, thus, has more N-BCNT layers deposited than sample 2 and sample 3. Hence, too many N-BCNT layers in the PU scaffold increase the probability that the system will fracture under cyclic pressure [84].

DOI: 10.14750/ME.2024.016

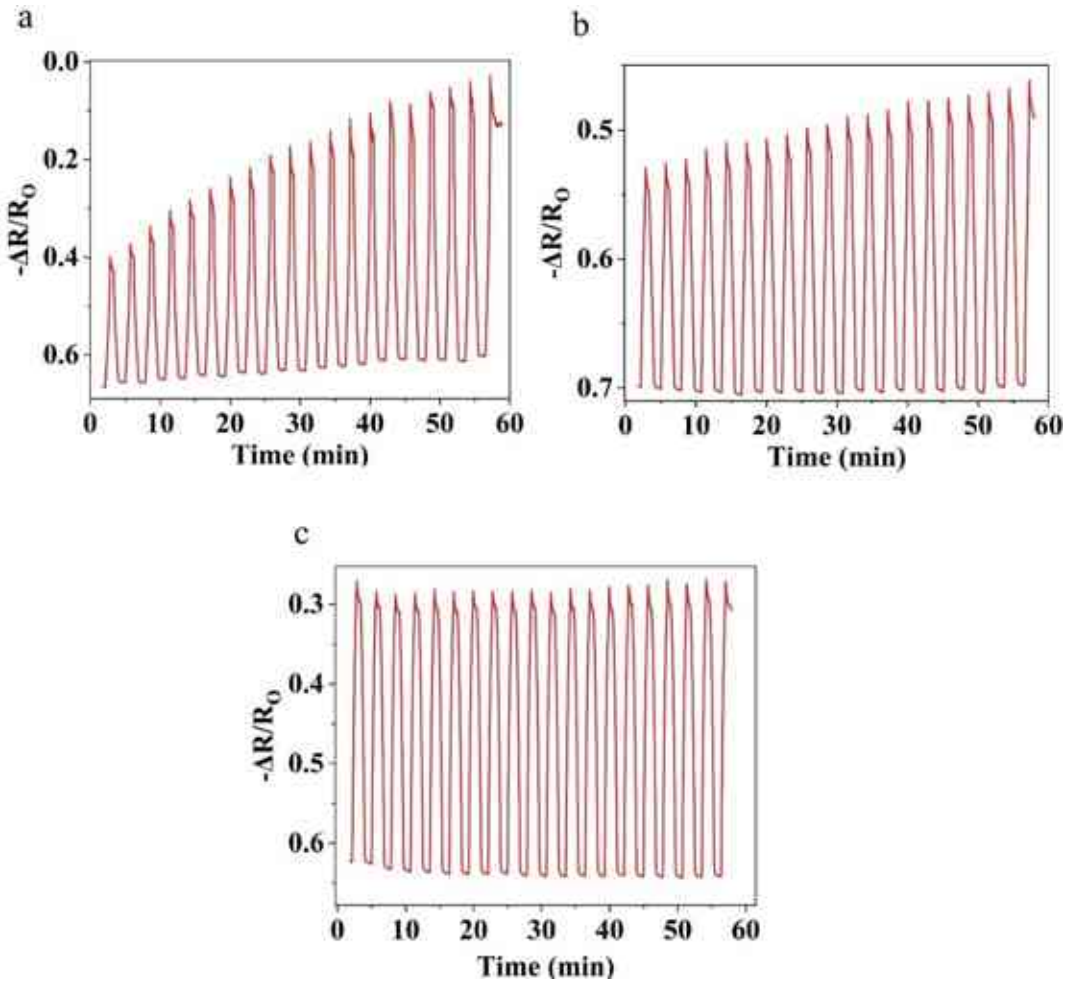

Figure 43. Cyclic load of N-BCNT-PU composite for sample 1(a), sample 2 (b), and sample 3 (c).

3.5.3 Morphology of N-BCNT-PU composite

The morphology of the N-BCNT/PU was investigated as shown in Figure 44, and it was found that the PU foams are completely coated with N-BCNT, and the structure reveals a wrinkle due to the presence of N-BCNTs. This could indicate that the nanotubes are bound to the foam by the dip-coating process. In addition, sample 1 is more wrinkled than samples 2 and 3, due to the larger total pore volume, which leads to a lower total PU scaffold and density. Consequently, more interconnected N-BCNTs lead to more wrinkles and burrs. The burrs and wrinkles serve as "microswitches", which regulate the electrical resistance [191]. Therefore, the electrical resistance of sample 1 is expected to be lower than that of sample 2 and sample 3. In addition, the surface of sample 1 is rich and covered with more carbon nanotubes. Thus, sample 1 has a higher electrical conductivity and lower electrical resistance than sample 2 and sample 3.

DOI: 10.14750/ME.2024.016

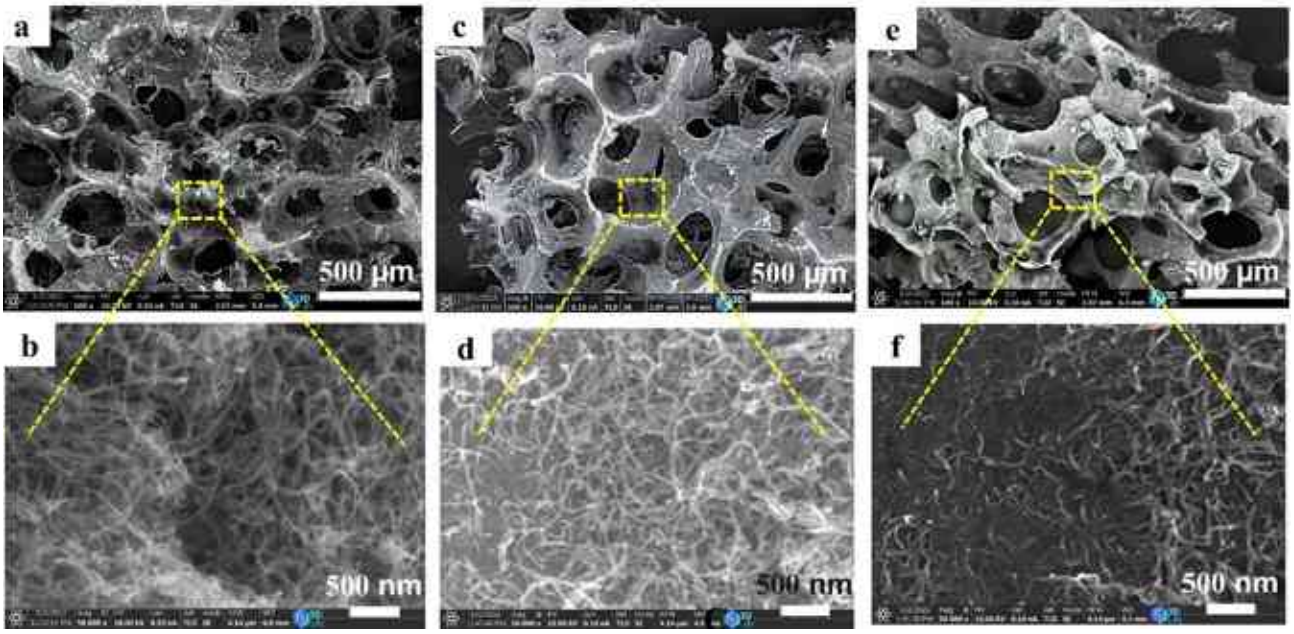

Figure 44. SEM images of N-BCNT/PU sensors for samples 1 (a-b), sample 2 (c-d), and sample 3 (e-f).

3.5.4 Application of N-BCNT-PU composite

The PU/N-BCNT pressure sensors were tested in different applications to prove their applicability (Figure 45). The detection of motion and finger touch is possible as shown in Figure 45 a-b. The resistance changes in the sensor was recorded during the pressure sequence during loading and unloading. The amount of pressure applied to the sensor during each movement with the finger or foot determines the peak amplitudes. This demonstrates the developed sensors' ability to detect different types of motion. In addition, the sensor shows high performance in detecting the low-pressure range, even for noncontact pressure modes such as the detection of breath (Figure 45c). Moreover, gentle breathing results in a nearly identical and repetitive change in resistance, while rapid breath leads to irregular patterns. To prove the piezoresistive effect of one of the pressure sensors, a LED -containing pressure sensor circuit was also created by using sample 1 (Figure 45 d). The brightness of the light from the LED increases when pressure is applied to the sensor. This also shows that the developed N-BCNT/PU nanocomposite has a piezoresistive effect and can be utilized as a pressure sensor. All in all, the properties of the developed sensors are very promising and indicate that these could be utilized in wearable device applications.

DOI: 10.14750/ME.2024.016

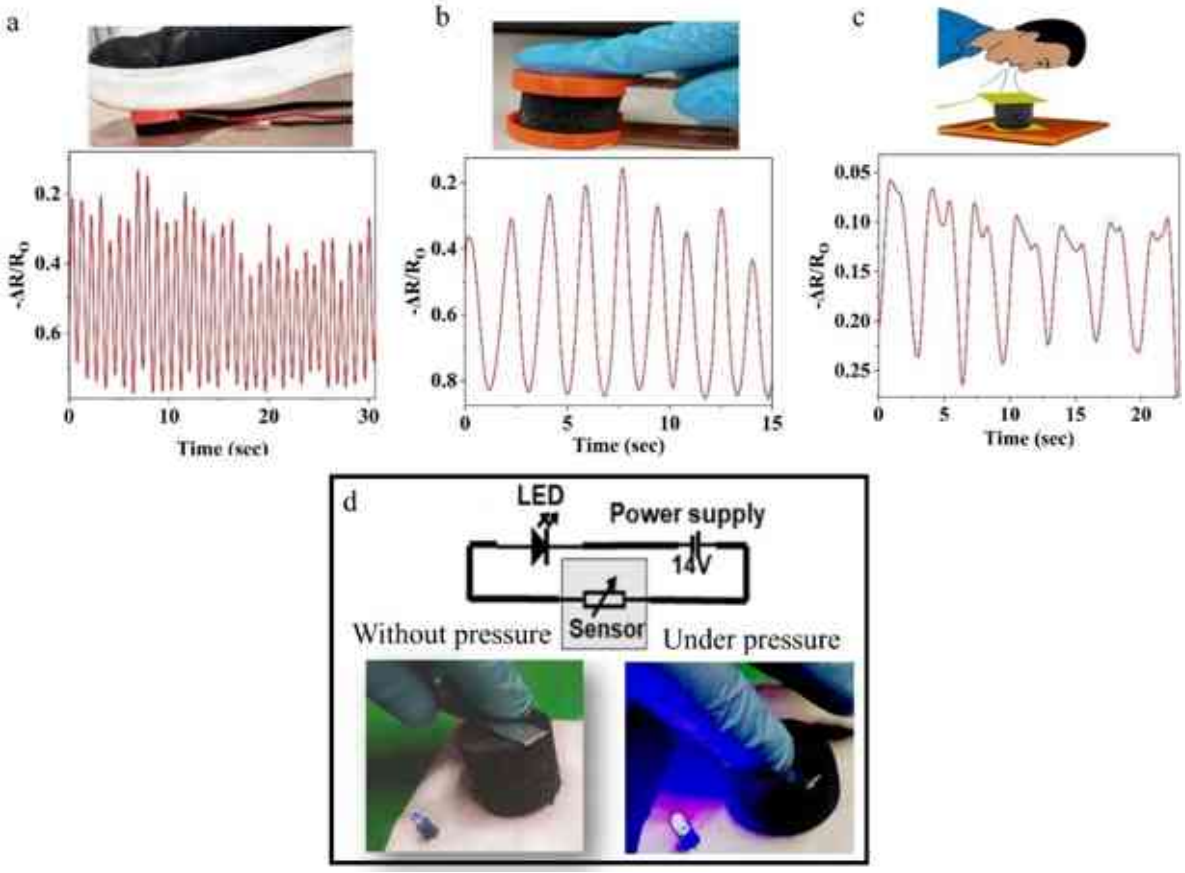

Figure 45. The N-BCNT/PU (sample 1) pressure sensor was tested in motion detection (a) finger touch detection (b), and breath detection (c), and a LED-containing pressure sensor circuit was successfully created (d).

3.6 N-BCNT: CB-PU/PU flexible pressure sensor for e-skin application evaluation

The fabrication process of the flexible pressure sensor for e-skin application is detailed in section 2.3.6. The preparation of e-skin required high reliability in the selection of materials and methodology used. The optimum methodology was selected as described in section 3.2.1 because this approach ensures the high quality of dispersion on the nanofiller in the polymer matrix. The optimum selection of nanofiller based on results described in section 3.4.1 by utilizing a 7:3 N-BCNT: CB mixing ratio. The best PU foam type was selected according to results described in section 3.5.1 by using 1.0:0.8 isocyanate: polyol mixing ratio because this type of PU foam is characterized by the large size of the pores, which ensures the best sensitivity to pressure, as well as allows subsequently penetration of the largest amount of silicone rubber easily into the PU pore.

DOI: 10.14750/ME.2024.016

3.6.1 Piezoelectric and electrical properties of e-skin

Figure 46 revealed the relationship between relative change in resistance and applied pressure. The relative change in resistance as the pressure increased, and vice versa. This phenomenon could be explained by the decreasing distance between nanofillers, creating more conductive paths and giving e-skin a higher electrical conductivity. Pressure sensitivity is one of the key parameters that define sensor performance. To measure pressure sensitivity, one would calculate the slope of the curve of relative change in resistance and apply pressure using Equation 1. Results showed that in the range of 0-120 kPa, the pressure sensitivity was 0.04 kPa^{-1}; similarly, in the 180-1000 kPa range it was also 0.07 kPa^{-1}. These findings demonstrate the versatility of the e-skin in terms of pressure detection. The high sensitivity of the e-skin is due to a synergistic effect between N-BCNT and CB, which enhances pressure sensitivity and performance. N-BCNTs have high electrical conductivity and a large surface area [192] [193][194], thus increasing sensitivity even further. Although N-BCNTs have a high aspect ratio, their conducting networks may not be perfect in the polymer matrix. CB can fill in any gaps between N-BCNTs to enhance electrical conductivity and lower the skin's electrical resistance. Furthermore, this indicates that nanotubes are crucial in the formation of conductive networks. N-BCNTs serve as the backbone for electrical conductivity in hybrid nanofillers while CB fills any gaps between them to further improve electrical conductivity [187][183]. The combined electrical and mechanical properties of these materials may enhance sensitivity to changes in pressure. Furthermore, CB's high surface area may increase sensitivity by providing more points of contact with the matrix material, providing a more sensitive response when pressure changes occur. Overall, N-BCNT and CB combine for excellent pressure sensor sensitivity when combined.

DOI: 10.14750/ME.2024.016

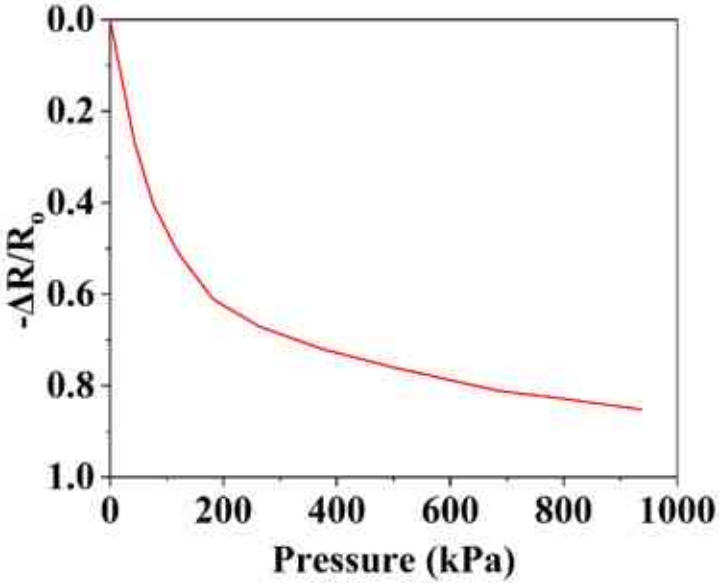

Figure 46. Relative change resistance vs pressure to demonstrate the pressure sensitivity of e-skin

Figure 47 illustrates an investigation of pressure's effect on signal stability for the e-skin using relative change in resistance as a function of time. Results revealed an inversely proportional relationship between applied pressure and noise level. Hence, noise levels are higher at low pressures and reduced at high pressures. This pattern could be due to two possible reasons. First, signal noise is highly dependent on the pressure sensitivity of the pressure sensor. Low pressure causes high-pressure sensitivity, leading to a strong output signal and plenty of noise. On the other hand, high pressure has low sensitivity; thus, we get a weak output signal with reduced noise levels. The second explanation for the inverse relationship between pressure and signal noise can be explained by considering the distances between nanofillers in the polymer matrix and their source of electrical current flow. Conversely, at high pressure, the distances between nanofiller particles in a polymer matrix are decreased, leading to new conductive networks and greater current flow - ultimately leading to lower signal noise. The relationship between pressure and signal noise in e-skin is determined by both sensor sensitivity and how far apart each nanofiller is within its matrix.

DOI: 10.14750/ME.2024.016

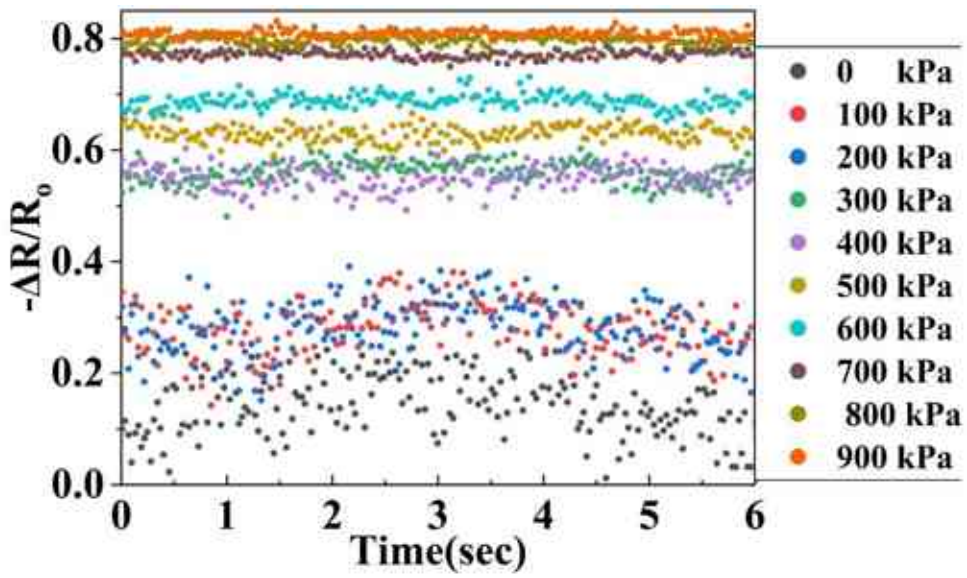

Figure 47. depicts the relationship between relative resistance and time under various pressure levels, emphasizing how pressure affects noise signals in e-skin.

The hysteretic behavior of the e-skin sensor was evaluated across a pressure range of 0 to 1000 kPa by measuring relative change in resistance (Figure 48). Analysis of the hysteresis loop revealed the minimal difference between ascending and descending pressure paths due to the viscoelastic characteristics of the SR matrix. Combining PU with SR in the sensor structure resulted in a significant reduction of this loop, showing improved precision when measuring pressure changes within a specified pressure range. Furthermore, the N-BCNT: CB hybrid nanofiller further enhanced sensor performance by blocking noise out while increasing signal integrity for better measurement purposes.

DOI: 10.14750/ME.2024.016

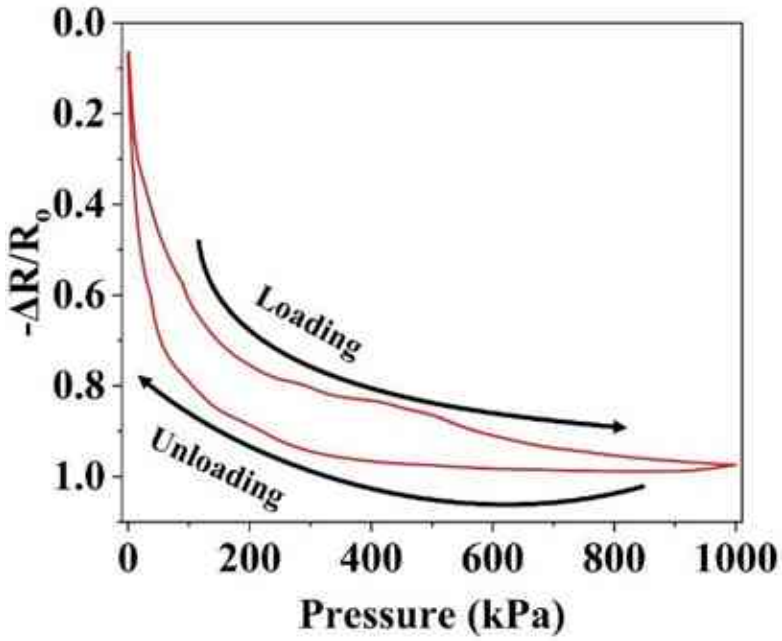

Figure 48. Demonstrates the hysteresis loop of the e-skin through the representation of relative change in resistance as a function of applied pressure.

A cyclic test was conducted to evaluate the performance and stability of a pressure sensor under repeated loading and unloading conditions. Figure 49 depicts the results, showing that after pressure was removed from the sensor, its relative resistance returned to a certain degree. This confirms its consistency and repeatability. The addition of N-BCNT and CB as nanofillers in the pressure sensor significantly enhanced its electrical conductivity. It demonstrated excellent recoverability and reproducibility due to strong bonding at the interface between CB and N-BCNT in the sensor. Compression enabled CBs to repair damaged N-BCNT pathways by filling gaps between nanotubes due to their greater mobility in the polymer matrix[186][186]. In conclusion, pressure sensor performance was exceptional due to SR's extreme flexibility and hybrid nanofillers' capacity to create conductive networks.

DOI: 10.14750/ME.2024.016

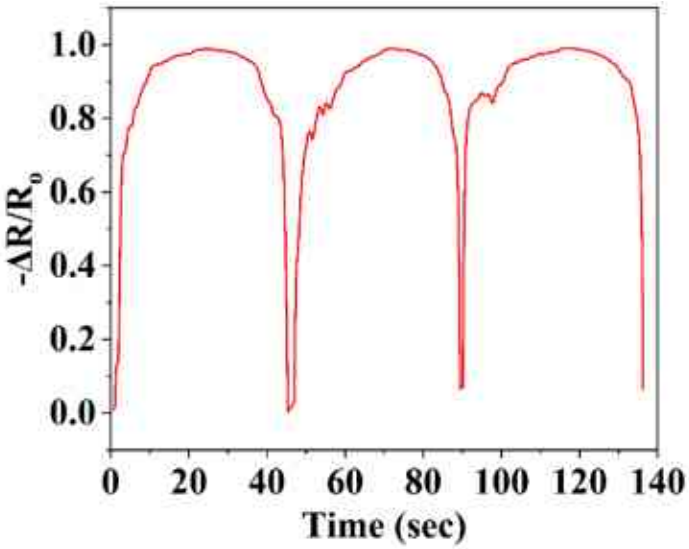

Figure 49. Cyclic load of e-skin

3.6.2 Morphology and structure characterization of e-skin

Figure 50 (a-e) provides an analysis of the performance and morphology of an e-skin sensor through SEM imaging. These images demonstrate a PU coating with a nanofiller that surrounds a flexible SR, giving it electrical conductivity thanks to its nanofiller coating. Meanwhile, the SR provides durability and flexibility so it can withstand various environments without damage or breakage. Figure 50 (c-d) illustrates this uniform dispersion of nanofiller through PU foam. This homogenous structure improves sensor performance by offering higher electrical conductivity and enhanced data transmission. In addition, Figure 50e displays the superior performance of N-BCNT: CB at a 7:3 mixing ratio on a pressure sensor. This combination increases its conductivity, enabling it to accurately measure and transmit pressure data. As all parts work in synergy, N-BCNT: CB increases both the reliability and durability of the device. Figure 51a depicts a Micro-CT scan of the e-skin, the plane from which this sample has been examined, while Figure 51b gives an understanding of e-skin's architecture. Micro CT scan results reveal that SR had penetrated and filled every pore space of PU foam, providing improved flexibility and durability. Micro CT scan results demonstrate that SR had penetrated and filled every pore space of PU foam, leading to improved flexibility and durability.

DOI: 10.14750/ME.2024.016

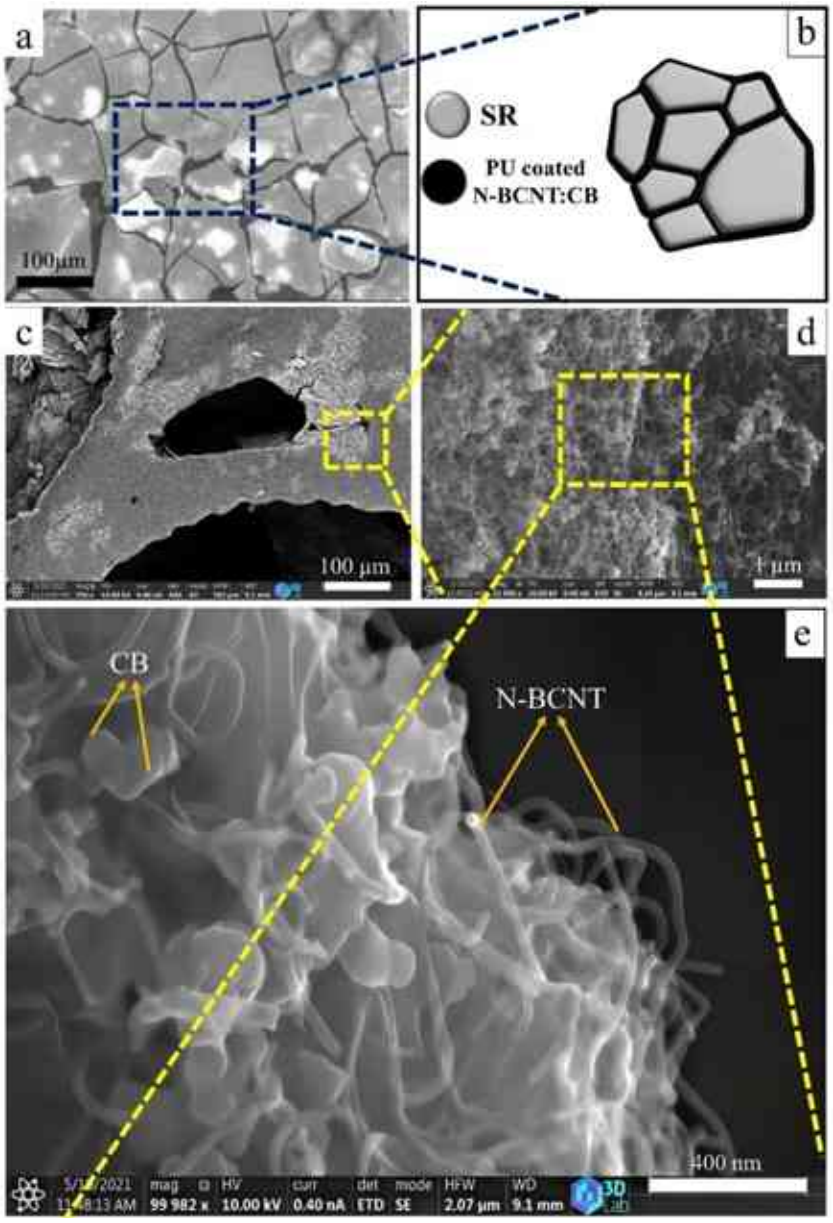

Figure 50. The morphology of e-skin (a). A schematic representation of an SR surrounding the PU (b). SEM images of N-BCNT: CB hybrid structures (c-d) and demonstrate their synergistic effect when combined (e).

DOI: 10.14750/ME.2024.016

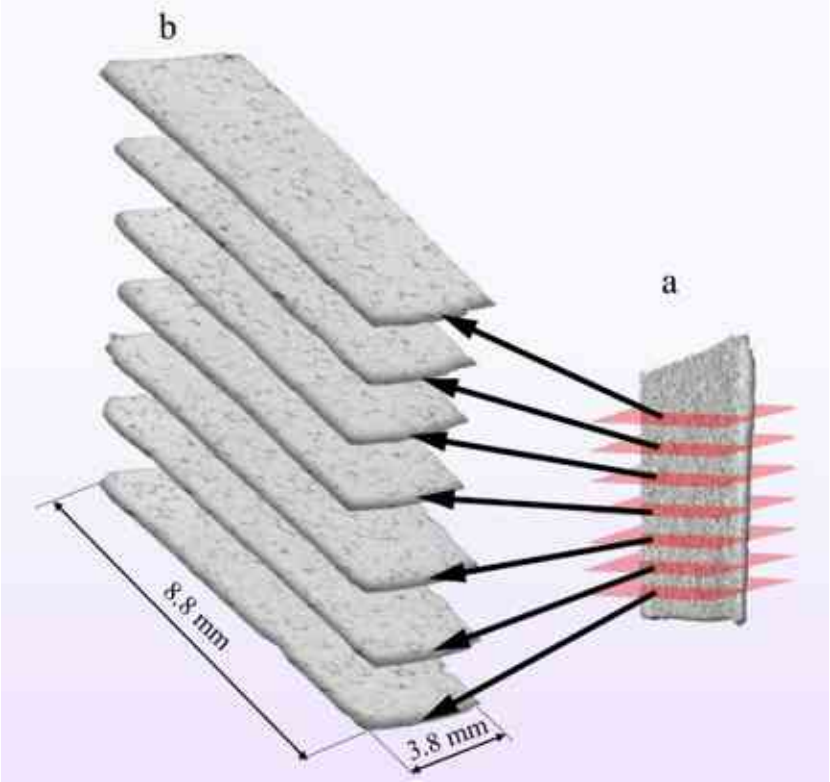

Figure 51. Micro-CT imaging allows us to view the internal microstructure of an e-skin. Panels depict various planes of the skin (a), while cross-sectional views reveal its intricate microarchitecture (b).

3.6.3 Application of e-skin

Figure 52 and Figure 53 demonstrate the relative change in resistance over time for a flexible pressure sensor designed to detect finger, wrist, elbow, and knee movements as well as twisting and stretching. The data demonstrate the sensor's excellent sensitivity and responsiveness to different movements, as evidenced by the distinct waveforms on each curve for each motion. The pressure sensor's high sensitivity is achieved through the combination of N-BCNT and CB, with N-BCNT providing electrical conductivity while CB fills any gaps between them. This working relationship enables the sensor to detect and respond to various movements. Additionally, the good dispersion of the nanofiller and the high flexibility of the SR contribute to the sensor's sensitivity. The efficient transfer of movements within the SR facilitates efficient detection, further increasing its response. On the other hand, the high flexibility of the SR enables it to detect movements even when deformed. These findings indicate that pressure sensors have potential

DOI: 10.14750/ME.2024.016

applications beyond e-skin applications where accuracy in detection and response to different movements is essential.

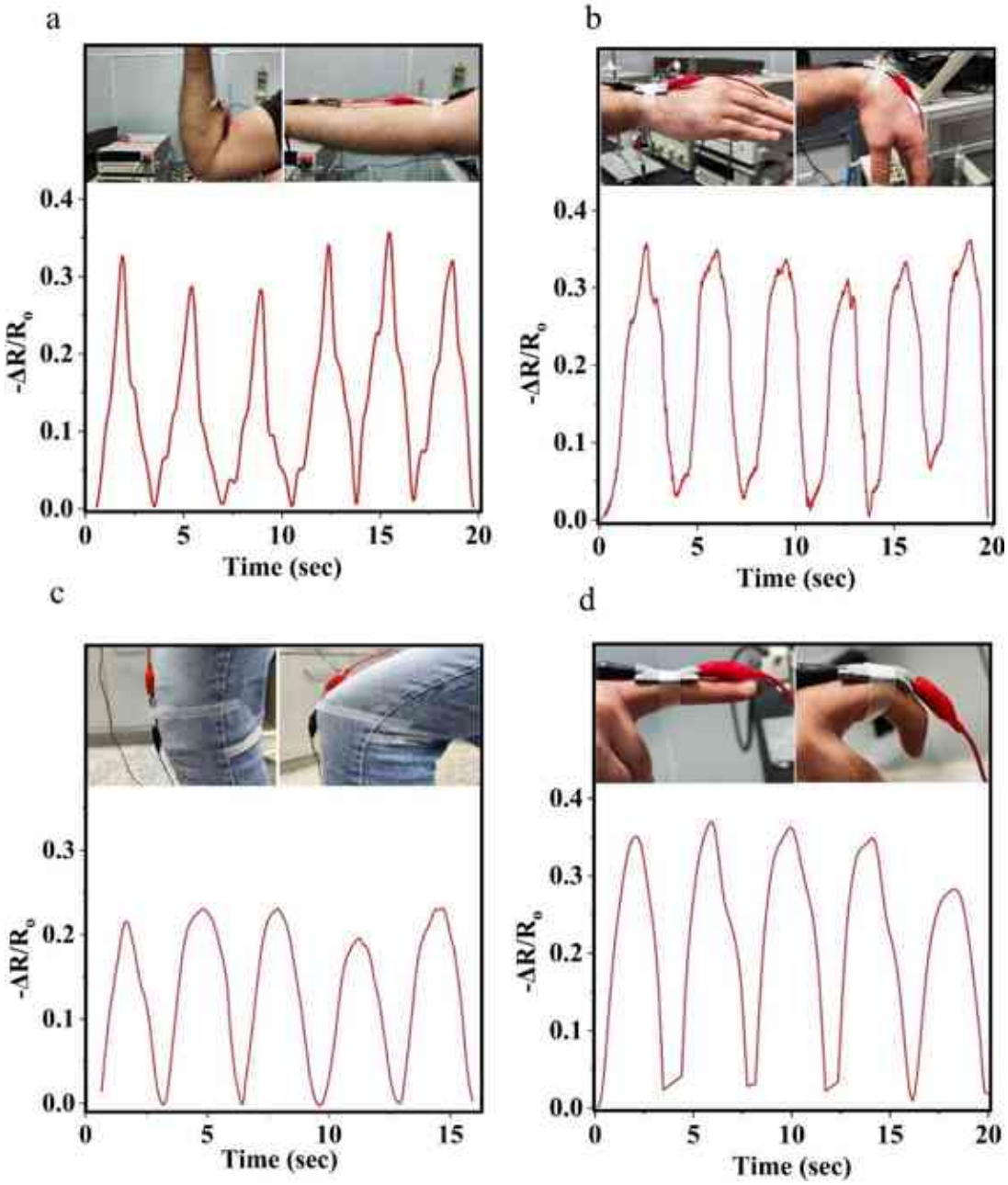

Figure 52. The illustration shows a pressure sensor suitable for use in an e-skin application. It can detect movement at the elbow joint (a), the wrist joint(b), the knee (c), and the index finger joint(d).

DOI: 10.14750/ME.2024.016

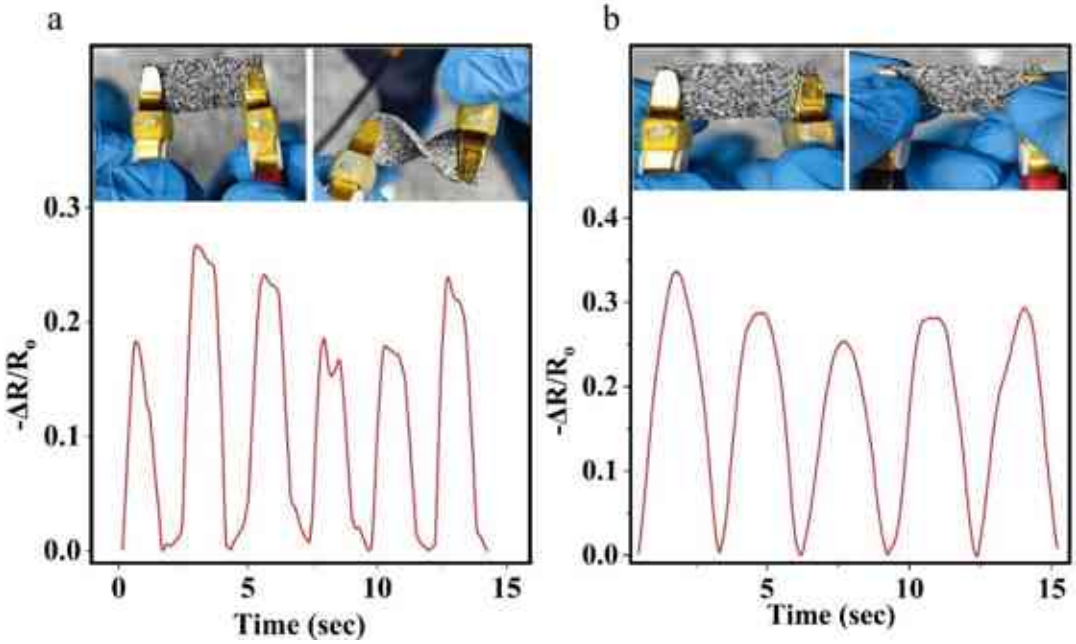

Figure 53. The twisting (a) and stretching movements (b) of e-skin.

DOI: 10.14750/ME.2024.016

Chapter 4

4. Conclusion

Flexible pressure sensors have a wide range of applications in areas such as e-skin and wearable technology. Nanocomposites consisting of nanofillers combined with a polymer matrix have shown tremendous potential and are more cost-effective than other conventional methods. Fabrication of flexible pressure sensors using nanocomposite technology primarily involves converting insulating polymers into conductive ones by mixing them with conductive nanofillers to sense the change in electrical resistance in response to applied pressure. To efficiently utilize the properties of nanofillers in FPS, it is critical to create a continuous conductive network pathway within the polymer matrix and achieve an electrical conductivity percolation threshold. In conventional approaches such as direct mixing and mixing in solution, the nanofiller loading must be increased to reach the electrical threshold. However, when the nanofiller loading is high, bundles are more likely to occur, this bundling causes an increase in the viscosity of the polymer matrix, which affects sensor performance. Also, the use of high-power ultrasonication and shear mixing to achieve uniform dispersion of nanofillers in the polymer matrix. However, this approach can lead to thermal degradation and structural damage, which affects the durability of the sensor. This is because the high power can cause the polymer chains to break in the center point or at the structurally weakest points. An alternative approach is to disperse nanofillers on a foam skeleton using an immersion process. This structure is then impregnated and combined with a polymer to produce the final sensor system. In this approach, the nanofiller spans the entire volume of the polymer and provides electrical conductivity in the macroscopic dimension of the sensor. It also minimizes the negative impact on the sensor's performance since no further processing is required. Using this approach, a flexible pressure sensor was fabricated for use in e-skin applications, with the lowest added weight percentage (0.4) compared to previous research.

DOI: 10.14750/ME.2024.016

New Scientific Results

Thesis 1

Fabrication of a novel flexible pressure sensor for e-skin applications with very low nanofiller loading. Moreover, compared to other works, our pressure sensor satisfies the electrical conductivity at nano-filler loading as low as (0.4 wt.%).

Thesis 2

Improve the dispersibility of the nanofiller through a unique technique for the first time by dispersing it on the PU foam skeleton to create a continuous conductive network, which is then impregnated in silicone rubber. This approach is like an implanted conductor network in the insulating silicone rubber. Each of these materials has a specific role: PU serves as the supporting skeleton, the nanofiller provides the electrical conductivity to measure the change in resistance when pressure is applied, and the silicone rubber serves as the matrix and provides the flexibility and elasticity of the nanocomposite.

Thesis 3

A novel investigation of the effect of the pore volume of PU foam by designing three different types of PU prepared as the supporting skeleton for the nanofiller, using isocyanate indices of 1.0:0.8, 1.0:1.0, and 1.0:1.1 to obtain different pore volumes of PU foam. Our work revealed that the best isocyanate index was 1.0:0.8 because the synthesized PU foam has a higher pore volume than the others. Regarding the pressure sensitivity of the pressure sensor, the results show that the PU foam with high pore volume has the highest pressure sensitivity when used as a supporting skeleton for the nanofiller. Since a high total pore volume leads to a lower PU foam scaffold, more nanofillers are consequently interconnected, resulting in more conductive paths and a larger effective conductive area in the PU scaffold. In addition, a large pore volume provides suitable spatial pores for elastic deformation of flexible pressure sensors.

Thesis 4

Using cutting- edge technology, I evaluate the pore volume from PU is based for the first time on micro-CT, which offers higher accuracy than conventional methods such as mercury intrusion porosimeter, gas adsorption, and SEM. Micro-CT is the best choice because scanning the sample produces a 3D image that enables highly accurate measurements for the analysis of pore size and polyurethane distribution. Micro-CT technology offers a highly accurate method to

precisely measure the pore volume within polyurethane foam. Its excellent technology in visualizing each individual pore, a unique advantage over traditional techniques. With its detailed imaging, it preserves the foam's structure without causing damage. Thus, Micro-CT is considered a valuable tool, to in-depth exploration of the foam's pore structure and providing critical insights into pressure sensor behavior and performance. In addition, micro-CT provides a complete understanding of the pore size and distribution of polyurethane foams, which allowed us to accurately investigate the relationship between pore size and pressure sensitivity.

Thesis 5

Novel design of a flexible pressure sensor by impregnation with silicone rubber to fill all pores of the PU foam. In the absence of silicone rubber, the nanofiller could be unintentionally removed from the nanofiller/ PU system when pressure is applied, as only van der Waals forces hold them together. Furthermore, impregnation with silicone rubber can mitigate the toxicity of CNTs in several ways. First, it can create a barrier that prevents CNTs from entering the environment. Second, it can interact with the surface of the CNTs and change their surface chemistry, making them less toxic. I believe that my work makes an important contribution to CNT research by proposing a method to reduce the toxicity of CNTs. This is an important topic as it could enable the use of CNTs in a wider range of applications, including those where humans may be at risk. While my work proposes a technique to reduce CNT toxicity, further research is needed to fully understand the long-term health effects of exposure to CNT-silicone rubber composites.

Thesis 6

Optimization of nanofiller using different mixing ratios (5:5, 6:4, 7:3, 8:2, 9:1) of N-BCNT: CB on the behavior of the flexible pressure sensor investigated. The results show that the optimal mixing ratio is 7:3 N-BCNT: CB, which is even better than N-BCNT alone. This mixing ratio is optimal for pressure sensitivity due to the synergistic effect of the nanofillers. When the ratio of N-BCNT to CB goes beyond 7:3, it becomes more difficult for the N-BCNT to align and expand, and the relative amount of CB also decreases, resulting in minimal contact between the fillers. On the other hand, the reduction of the N-BCNT fraction decreases the ability of electrical charge transport over long distances along the aligned and extended nanotubes.

List of publications

1) **Mohammed Nabeel**, Mousa, M., Viskolcz, B., Fiser, B., & Vanyorek, L. Recent Advances in Flexible Foam Pressure Sensors: Manufacturing, Characterization, and Applications – a Review. *Polymer Reviews*, 2023, 1–41. https://doi.org/10.1080/15583724.2023.2262558 . **Q1 (IF: 14.5)**

2) **Mohammed Nabeel**, László Kuzsella, Béla Viskolcz, Mariann Kollar, Béla Fiser, László Vanyorek, 2023. Synergistic Effect of Carbon Nanotubes and Carbon Black as Nanofillers of Silicone Rubber Pressure Sensors. Arabian Journal of Chemistry 104594. https://doi.org/10.1016/j.arabjc.2023.104594. **Q1 (IF: 6.21)**
3) **Mohammed Nabeel**, Miklós Varga, László Kuzsela, Béla Fiser, Béla Viskolcz, László Vanyorek, 2022. The Effect of Pore, Volume on the Behavior of Polyurethane-Foam-Based Pressure Sensors. Polymers (Basel) 14, 3652. doi.org/10.3390/polym14173652. **Q1 (IF: 4.9)**
4) **Mohammed Nabeel**, Miklós Varga, László Kuzsela, Ádám Filep, Béla Fiser, Béla Visklocz, Mariann Kollar, László Vanyorek, 2021. Preparation of bamboo-like carbon nanotube loaded piezoresistive polyurethane-silicone rubber composite. Polymers (Basel) 13, 2144. https://doi.org/10.3390/polym13132144 . **Q1 (IF: 4.9)**
5) **Mohammed Nabeel**, Ali J. Addie, Béla Viskolcz, Mariann Kollar, Béla Fiser, László Vanyorek, Development of Flexible Pressure Sensors Based on Polyurethane-Silicone Rubber-Nanocomposite Systems, Arabian Journal of Chemistry. **Under review Q1 (IF: 6.21).**

References

1. Wang, X.; Yu, J.; Cui, Y.; Li, W. Research Progress of Flexible Wearable Pressure Sensors. *Sens Actuators A Phys* **2021**, *330*, 112838, doi:10.1016/j.sna.2021.112838.
2. Pierre Claver, U.; Zhao, G. Recent Progress in Flexible Pressure Sensors Based Electronic Skin. *Adv Eng Mater* **2021**, *23*, 2001187, doi:10.1002/adem.202001187.
3. Wang, M.; Wang, T.; Luo, Y.; He, K.; Pan, L.; Li, Z.; Cui, Z.; Liu, Z.; Tu, J.; Chen, X. Fusing Stretchable Sensing Technology with Machine Learning for Human–Machine Interfaces. *Adv Funct Mater* **2021**, *31*, 2008807, doi:10.1002/adfm.202008807.
4. Guo, Y.; Li, H.; Li, Y.; Wei, X.; Gao, S.; Yue, W.; Zhang, C.; Yin, F.; Zhao, S.; Kim, N.; et al. Wearable Hybrid Device Capable of Interactive Perception with

Pressure Sensing and Visualization. *Adv Funct Mater* **2022**, *32*, 2203585, doi:10.1002/adfm.202203585.

5. Shintake, J.; Cacucciolo, V.; Floreano, D.; Shea, H. Soft Robotic Grippers. *Advanced Materials* **2018**, *30*, 1707035, doi:10.1002/adma.201707035.

6. Tang, Y.-D.; Wang, P.; Li, G.-X.; Wang, G.-Y.; Yu, W.; Meng, C.-Z.; Guo, S.-J. Flexible and Ultra-Sensitive Planar Supercapacitive Pressure Sensor Based on Porous Ionic Foam. *Adv Eng Mater* **2023**, *25*, 2200814, doi:10.1002/adem.202200814.

7. Guo, K.; Gao, S.; Li, Y.; Yin, J.; Yue, W.; Zhao, S.; Zhang, C.; Liu, J.; Li, S.; Wu, S.; et al. A P(VDF-TrFE) Nanofiber Composites Based Multilayer Structured Dual-Functional Flexible Sensor for Advanced Pressure-Humidity Sensing. *Chemical Engineering Journal* **2023**, *461*, 141970, doi:10.1016/j.cej.2023.141970.

8. He, W.; Dai, Z.; Zou, K.; Li, X.; Hao, S.; Wang, H. Flexible Piezoelectric PVDF Nanofiber Film Sensor by Blow Spinning. *Sci China Technol Sci* **2023**, *66*, 863–868, doi:10.1007/s11431-022-2267-8.

9. Lei, X.; Ma, L.; Li, Y.; Cheng, Y.; Cheng, G.J.; Liu, F. Highly Sensitive and Wide-Range Flexible Pressure Sensor Based on Carbon Nanotubes-Coated Polydimethylsiloxane Foam. *Mater Lett* **2022**, *308*, 131151, doi:10.1016/j.matlet.2021.131151.

10. Liu, M.-Y.; Zhao, X.-F.; Hang, C.-Z.; Zhu, L.-Y.; Wu, X.-Y.; Wen, X.-H.; Wang, J.-C.; Lu, H.-L. A Stretchable Pressure Sensor with Interlinked Interfaces Prepared by a Template-Free Process. *Compos Part A Appl Sci Manuf* **2022**, *162*, 107144, doi:10.1016/j.compositesa.2022.107144.

11. Ma, Z.; Zhang, K.; Yang, S.; Zhang, Y.; Chen, X.; Fu, Q.; Deng, H. High-Performance Capacitive Pressure Sensors Fabricated by Introducing Dielectric Filler and Conductive Filler into a Porous Dielectric Layer through a Biomimic Strategy. *Compos Sci Technol* **2022**, *227*, 109595, doi:10.1016/j.compscitech.2022.109595.

12. Hwang, J.; Kim, Y.; Yang, H.; Oh, J.H. Fabrication of Hierarchically Porous Structured PDMS Composites and Their Application as a Flexible Capacitive Pressure Sensor. *Compos B Eng* **2021**, *211*, 108607, doi:10.1016/j.compositesb.2021.108607.

13. Chhetry, A.; Sharma, S.; Yoon, H.; Ko, S.; Park, J.Y. Enhanced Sensitivity of Capacitive Pressure and Strain Based on CaCu3Ti4O12 Wrapped Hybrid Sponge for Wearable Applications. *Adv Funct Mater* **2020**, *30*, 1910020, doi:10.1002/adfm.201910020.

14. Han, C.; Zhang, H.; Chen, Q.; Li, T.; Kong, L.; Zhao, H.; He, L. A Directional Piezoelectric Sensor Based on Anisotropic PVDF/MXene Hybrid Foam Enabled by

Unidirectional Freezing. *Chemical Engineering Journal* **2022**, *450*, 138280, doi:10.1016/j.cej.2022.138280.

15. Li, R.; Zhou, Q.; Bi, Y.; Cao, S.; Xia, X.; Yang, A.; Li, S.; Xiao, X. Research Progress of Flexible Capacitive Pressure Sensor for Sensitivity Enhancement Approaches. *Sens Actuators A Phys* **2021**, *321*, 112425, doi:10.1016/j.sna.2020.112425.

16. Xu, D.; Zhang, H.; Pu, L.; Li, L. Fabrication of Poly(Vinylidene Fluoride)/Multiwalled Carbon Nanotube Nanocomposite Foam via Supercritical Fluid Carbon Dioxide: Synergistic Enhancement of Piezoelectric and Mechanical Properties. *Compos Sci Technol* **2020**, *192*, 108108, doi:10.1016/j.compscitech.2020.108108.

17. Ruth, S.R.A.; Beker, L.; Tran, H.; Feig, V.R.; Matsuhisa, N.; Bao, Z. Rational Design of Capacitive Pressure Sensors Based on Pyramidal Microstructures for Specialized Monitoring of Biosignals. *Adv Funct Mater* **2020**, *30*, 1903100, doi:10.1002/adfm.201903100.

18. Gao, K.; Zhang, Z.; Weng, S.; Zhu, H.; Yu, H.; Peng, T. Review of Flexible Piezoresistive Strain Sensors in Civil Structural Health Monitoring. *Applied Sciences* **2022**, *12*, 9750, doi:10.3390/app12199750.

19. Kumar, V.; Kumar, A.; Han, S.S.; Park, S.-S. RTV Silicone Rubber Composites Reinforced with Carbon Nanotubes, Titanium-Di-Oxide and Their Hybrid: Mechanical and Piezoelectric Actuation Performance. *Nano Materials Science* **2021**, *3*, 233–240, doi:10.1016/j.nanoms.2020.12.002.

20. Zheng, S.; Jiang, Y.; Wu, X.; Xu, Z.; Liu, Z.; Yang, W.; Yang, M. Highly Sensitive Pressure Sensor with Broad Linearity via Constructing a Hollow Structure in Polyaniline/Polydimethylsiloxane Composite. *Compos Sci Technol* **2021**, *201*, 108546, doi:10.1016/j.compscitech.2020.108546.

21. Zhou, H.; Wang, Z.; Zhao, W.; Tong, X.; Jin, X.; Zhang, X.; Yu, Y.; Liu, H.; Ma, Y.; Li, S.; et al. Robust and Sensitive Pressure/Strain Sensors from Solution Processable Composite Hydrogels Enhanced by Hollow-Structured Conducting Polymers. *Chemical Engineering Journal* **2021**, *403*, 126307, doi:10.1016/j.cej.2020.126307.

22. Veeramuthu, L.; Venkatesan, M.; Benas, J.-S.; Cho, C.-J.; Lee, C.-C.; Lieu, F.-K.; Lin, J.-H.; Lee, R.-H.; Kuo, C.-C. Recent Progress in Conducting Polymer Composite/Nanofiber-Based Strain and Pressure Sensors. *Polymers (Basel)* **2021**, *13*, 4281, doi:10.3390/polym13244281.

23. Sang, Z.; Ke, K.; Manas-Zloczower, I. Effect of Carbon Nanotube Morphology on Properties in Thermoplastic Elastomer Composites for Strain Sensors. *Compos Part A Appl Sci Manuf* **2019**, *121*, 207–212, doi:10.1016/j.compositesa.2019.03.007.

24. Gong, M.; Zhang, L.; Wan, P. Polymer Nanocomposite Meshes for Flexible Electronic Devices. *Prog Polym Sci* **2020**, *107*, 101279, doi:10.1016/j.progpolymsci.2020.101279.

25. Li, Y.; Chen, W.; Lu, L. Wearable and Biodegradable Sensors for Human Health Monitoring. *ACS Appl Bio Mater* **2020**, *4*, 122–139.

26. Cheng, H.; Wang, B.; Tan, Y.; Yin, Y.; Wang, C. Low-Cost, Highly Sensitive, and Flexible Piezoresistive Pressure Sensor Characterized by Low-Temperature Interfacial Polymerization of Polypyrrole on Latex Sponge. *Macromol Mater Eng* **2021**, *306*, 2000772, doi:10.1002/mame.202000772.

27. Badatya, S.; Bharti, D.K.; Sathish, N.; Srivastava, A.K.; Gupta, M.K. Humidity Sustainable Hydrophobic Poly(Vinylidene Fluoride)-Carbon Nanotubes Foam Based Piezoelectric Nanogenerator. *ACS Appl Mater Interfaces* **2021**, *13*, 27245–27254, doi:10.1021/acsami.1c02237.

28. Tewari, A.; Gandla, S.; Bohm, S.; McNeill, C.R.; Gupta, D. Highly Exfoliated MWNT–RGO Ink-Wrapped Polyurethane Foam for Piezoresistive Pressure Sensor Applications. *ACS Appl Mater Interfaces* **2018**, *10*, 5185–5195, doi:10.1021/acsami.7b15252.

29. Devnani, G.L.; Sinha, S. Effect of Nanofillers on the Properties of Natural Fiber Reinforced Polymer Composites. *Mater Today Proc* **2019**, *18*, 647–654, doi:10.1016/j.matpr.2019.06.460.

30. Dios, J.R.; Garcia-Astrain, C.; Gonçalves, S.; Costa, P.; Lanceros-Méndez, S. Piezoresistive Performance of Polymer-Based Materials as a Function of the Matrix and Nanofiller Content to Walking Detection Application. *Compos Sci Technol* **2019**, *181*, 107678, doi:10.1016/j.compscitech.2019.107678.

31. Ke, K.; Yue, L.; Shao, H.; Yang, M.-B.; Yang, W.; Manas-Zloczower, I. Boosting Electrical and Piezoresistive Properties of Polymer Nanocomposites via Hybrid Carbon Fillers: A Review. *Carbon N Y* **2021**, *173*, 1020–1040, doi:10.1016/j.carbon.2020.11.070.

32. Hu, J.; Yu, J.; Li, Y.; Liao, X.; Yan, X.; Li, L. Nano Carbon Black-Based High Performance Wearable Pressure Sensors. *Nanomaterials* **2020**, *10*, 664, doi:10.3390/nano10040664.

33. Han, Z.; Li, H.; Xiao, J.; Song, H.; Li, B.; Cai, S.; Chen, Y.; Ma, Y.; Feng, X. Ultralow-Cost, Highly Sensitive, and Flexible Pressure Sensors Based on Carbon Black and Airlaid Paper for Wearable Electronics. *ACS Appl Mater Interfaces* **2019**, *11*, 33370–33379, doi:10.1021/acsami.9b12929.

34. Hong, J.; Moon, H.; Kim, J.; Lee, B.; Kim, G.-B.; Lee, H.; Kim, Y. Differentiation of Carbon Black from Black Carbon Using a Ternary Plot Based on Elemental

Analysis. *Chemosphere* **2021**, *264*, 128511, doi:10.1016/j.chemosphere.2020.128511.

35. Gómez-Hernández, R.; Panecatl-Bernal, Y.; Méndez-Rojas, M.Á. High Yield and Simple One-Step Production of Carbon Black Nanoparticles from Waste Tires. *Heliyon* **2019**, *5*, e02139, doi:10.1016/j.heliyon.2019.e02139.

36. Sun, X.; Yao, F.; Li, J. Nanocomposite Hydrogel-Based Strain and Pressure Sensors: A Review. *J Mater Chem A Mater* **2020**, *8*, 18605–18623, doi:10.1039/D0TA06965E.

37. Li, S.-X.; Xia, H.; Xu, Y.-S.; Lv, C.; Wang, G.; Dai, Y.-Z.; Sun, H.-B. Gold Nanoparticle Densely Packed Micro/Nanowire-Based Pressure Sensors for Human Motion Monitoring and Physiological Signal Detection. *Nanoscale* **2019**, *11*, 4925–4932, doi:10.1039/C9NR00595A.

38. Habibullah, G.; Viktorova, J.; Ruml, T. Current Strategies for Noble Metal Nanoparticle Synthesis. *Nanoscale Res Lett* **2021**, *16*, 47, doi:10.1186/s11671-021-03480-8.

39. Mmaduka Obodo, R.; Ahmad, I.; Ifeanyichukwu Ezema, F. Introductory Chapter: Graphene and Its Applications. In *Graphene and Its Derivatives - Synthesis and Applications*; IntechOpen, 2019.

40. Chamoli, P.; Banerjee, S.; Raina, K.K.; Kar, K.K. Characteristics of Graphene/Reduced Graphene Oxide. In *Handbook of Nanocomposite Supercapacitor Materials I*; Springer, 2020; pp. 155–177.

41. Güler, Ö.; Bağcı, N. A Short Review on Mechanical Properties of Graphene Reinforced Metal Matrix Composites. *Journal of Materials Research and Technology* **2020**, *9*, 6808–6833, doi:10.1016/j.jmrt.2020.01.077.

42. Zhu, Y.; Cai, H.; Ding, H.; Pan, N.; Wang, X. Fabrication of Low-Cost and Highly Sensitive Graphene-Based Pressure Sensors by Direct Laser Scribing Polydimethylsiloxane. *ACS Appl Mater Interfaces* **2019**, *11*, 6195–6200, doi:10.1021/acsami.8b17085.

43. Lu, Y.; Tian, M.; Sun, X.; Pan, N.; Chen, F.; Zhu, S.; Zhang, X.; Chen, S. Highly Sensitive Wearable 3D Piezoresistive Pressure Sensors Based on Graphene Coated Isotropic Non-Woven Substrate. *Compos Part A Appl Sci Manuf* **2019**, *117*, 202–210, doi:10.1016/j.compositesa.2018.11.023.

44. Rennhofer, H.; Zanghellini, B. Dispersion State and Damage of Carbon Nanotubes and Carbon Nanofibers by Ultrasonic Dispersion: A Review. *Nanomaterials* **2021**, *11*, 1469, doi:10.3390/nano11061469.

45. Song, P.; Song, J.; Zhang, Y. Stretchable Conductor Based on Carbon Nanotube/Carbon Black Silicone Rubber Nanocomposites with Highly Mechanical,

Electrical Properties and Strain Sensitivity. *Compos B Eng* **2020**, *191*, 107979, doi:10.1016/j.compositesb.2020.107979.

46. Taylor, L.W.; Dewey, O.S.; Headrick, R.J.; Komatsu, N.; Peraca, N.M.; Wehmeyer, G.; Kono, J.; Pasquali, M. Improved Properties, Increased Production, and the Path to Broad Adoption of Carbon Nanotube Fibers. *Carbon N Y* **2021**, *171*, 689–694, doi:10.1016/j.carbon.2020.07.058.

47. Sun, X.; Qin, Z.; Ye, L.; Zhang, H.; Yu, Q.; Wu, X.; Li, J.; Yao, F. Carbon Nanotubes Reinforced Hydrogel as Flexible Strain Sensor with High Stretchability and Mechanically Toughness. *Chemical Engineering Journal* **2020**, *382*, 122832, doi:10.1016/j.cej.2019.122832.

48. Huang, L.; Chen, J.; Xu, Y.; Hu, D.; Cui, X.; Shi, D.; Zhu, Y. Three-Dimensional Light-Weight Piezoresistive Sensors Based on Conductive Polyurethane Sponges Coated with Hybrid CNT/CB Nanoparticles. *Appl Surf Sci* **2021**, *548*, 149268, doi:10.1016/j.apsusc.2021.149268.

49. Jagannatham, M.; Chandran, P.; Sankaran, S.; Haridoss, P.; Nayan, N.; Bakshi, S.R. Tensile Properties of Carbon Nanotubes Reinforced Aluminum Matrix Composites: A Review. *Carbon N Y* **2020**, *160*, 14–44, doi:10.1016/j.carbon.2020.01.007.

50. Takakura, A.; Beppu, K.; Nishihara, T.; Fukui, A.; Kozeki, T.; Namazu, T.; Miyauchi, Y.; Itami, K. Strength of Carbon Nanotubes Depends on Their Chemical Structures. *Nat Commun* **2019**, *10*, 3040, doi:10.1038/s41467-019-10959-7.

51. Zare, Y.; Rhee, K.Y. Evaluation of the Tensile Strength in Carbon Nanotube-Reinforced Nanocomposites Using the Expanded Takayanagi Model. *JOM* **2019**, *71*, 3980–3988, doi:10.1007/s11837-019-03536-2.

52. He, Y.; Zhou, M.; Mahmoud, M.H.H.; Lu, X.; He, G.; Zhang, L.; Huang, M.; Elnaggar, A.Y.; Lei, Q.; Liu, H.; et al. Multifunctional Wearable Strain/Pressure Sensor Based on Conductive Carbon Nanotubes/Silk Nonwoven Fabric with High Durability and Low Detection Limit. *Adv Compos Hybrid Mater* **2022**, *5*, 1939–1950, doi:10.1007/s42114-022-00525-z.

53. Gou, X.; Zhao, D.; Wu, C. Catalytic Conversion of Hard Plastics to Valuable Carbon Nanotubes. *J Anal Appl Pyrolysis* **2020**, *145*, 104748, doi:10.1016/j.jaap.2019.104748.

54. Sumfleth, J.; Buschhorn, S.T.; Schulte, K. Comparison of Rheological and Electrical Percolation Phenomena in Carbon Black and Carbon Nanotube Filled Epoxy Polymers. *J Mater Sci* **2011**, *46*, 659–669, doi:10.1007/s10853-010-4788-6.

55. Zhang, R.; Pan, P.; Dai, Q.; Yang, X.; Yang, Z.; Wei, J.; Liu, J.; Yuan, Q. Sensitive and Wearable Carbon Nanotubes/Carbon Black Strain Sensors with Wide Linear Ranges for Human Motion Monitoring. *Journal of Materials Science: Materials in Electronics* **2018**, *29*, 5589–5596, doi:10.1007/s10854-018-8528-z.

56. Lu, Y.; Biswas, M.C.; Guo, Z.; Jeon, J.-W.; Wujcik, E.K. Recent Developments in Bio-Monitoring via Advanced Polymer Nanocomposite-Based Wearable Strain Sensors. *Biosens Bioelectron* **2019**, *123*, 167–177, doi:10.1016/j.bios.2018.08.037.

57. Xu, F.; Li, X.; Shi, Y.; Li, L.; Wang, W.; He, L.; Liu, R. Recent Developments for Flexible Pressure Sensors: A Review. *Micromachines (Basel)* **2018**, *9*, 580, doi:10.3390/mi9110580.

58. Zhuang, Y.; Guo, Y.; Li, J.; Jiang, K.; Yu, Y.; Zhang, H.; Liu, D. Preparation and Laser Sintering of a Thermoplastic Polyurethane Carbon Nanotube Composite-Based Pressure Sensor. *RSC Adv* **2020**, *10*, 23644–23652, doi:10.1039/D0RA04479B.

59. Lee, B.-Y.; Kim, J.; Kim, H.; Kim, C.; Lee, S.-D. Low-Cost Flexible Pressure Sensor Based on Dielectric Elastomer Film with Micro-Pores. *Sens Actuators A Phys* **2016**, *240*, 103–109, doi:10.1016/j.sna.2016.01.037.

60. Tripathy, A.R.; Choudhury, A.; Dash, A.; Panigrahi, P.; Kumar, S.S.; Pancham, P.P.; Sahu, S.K.; Mallik, S. Polymer Matrix Composite Engineering for PDMS Based Capacitive Sensors to Achieve High-Performance and Broad-Range Pressure Sensing. *Applied Surface Science Advances* **2021**, *3*, 100062, doi:10.1016/j.apsadv.2021.100062.

61. Hashim, A.; Hadi, A. Novel Pressure Sensors Made from Nanocomposites (Biodegradable Polymers–Metal Oxide Nanoparticles): Fabrication and Characterization. *Ukrainian Journal of Physics* **2018**, *63*, 754, doi:10.15407/ujpe63.8.754.

62. Yang, Y.-J.; Cheng, M.-Y.; Chang, W.-Y.; Tsao, L.-C.; Yang, S.-A.; Shih, W.-P.; Chang, F.-Y.; Chang, S.-H.; Fan, K.-C. An Integrated Flexible Temperature and Tactile Sensing Array Using PI-Copper Films. *Sens Actuators A Phys* **2008**, *143*, 143–153, doi:10.1016/j.sna.2007.10.077.

63. Jiang, G. Design Challenges of Implantable Pressure Monitoring System. *Front Neurosci* **2010**, 2, doi:10.3389/neuro.20.002.2010.

64. Wang, L.; Wang, X.; Li, Y. Relation between Repeated Uniaxial Compressive Pressure and Electrical Resistance of Carbon Nanotube Filled Silicone Rubber Composite. *Compos Part A Appl Sci Manuf* **2012**, *43*, 268–274, doi:10.1016/j.compositesa.2011.10.017.

65. Giffney, T.; Bejanin, E.; Kurian, A.S.; Travas-Sejdic, J.; Aw, K. Highly Stretchable Printed Strain Sensors Using Multi-Walled Carbon Nanotube/Silicone Rubber Composites. *Sens Actuators A Phys* **2017**, *259*, 44–49, doi:10.1016/j.sna.2017.03.005.

66. Dittrich, B.; Wartig, K.-A.; Hofmann, D.; Mülhaupt, R.; Schartel, B. Flame Retardancy through Carbon Nanomaterials: Carbon Black, Multiwall Nanotubes,

Expanded Graphite, Multi-Layer Graphene and Graphene in Polypropylene. *Polym Degrad Stab* **2013**, *98*, 1495–1505, doi:10.1016/j.polymdegradstab.2013.04.009.

67. Tamayo-Vegas, S.; Muhsan, A.; Liu, C.; Tarfaoui, M.; Lafdi, K. The Effect of Agglomeration on the Electrical and Mechanical Properties of Polymer Matrix Nanocomposites Reinforced with Carbon Nanotubes. *Polymers (Basel)* **2022**, *14*, 1842, doi:10.3390/polym14091842.

68. Dai, S.-W.; Gu, Y.-L.; Zhao, L.; Zhang, W.; Gao, C.-H.; Wu, Y.-X.; Shen, S.-C.; Zhang, C.; Kong, T.-T.; Li, Y.-T.; et al. Bamboo-Inspired Mechanically Flexible and Electrically Conductive Polydimethylsiloxane Foam Materials with Designed Hierarchical Pore Structures for Ultra-Sensitive and Reliable Piezoresistive Pressure Sensor. *Compos B Eng* **2021**, *225*, 109243, doi:10.1016/j.compositesb.2021.109243.

69. Huang, L.; Wang, H.; Zhan, D.; Fang, F. Flexible Capacitive Pressure Sensor Based on Laser–Induced Graphene and Polydimethylsiloxane Foam. *IEEE Sens J* **2021**, *21*, 12048–12056, doi:10.1109/JSEN.2021.3054985.

70. Kim, D.H.; Jung, Y.; Jung, K.; Kwak, D.H.; Park, D.M.; Shin, M.G.; Tak, H.J.; Ko, J.S. Hollow Polydimethylsiloxane (PDMS) Foam with a 3D Interconnected Network for Highly Sensitive Capacitive Pressure Sensors. *Micro and Nano Systems Letters* **2020**, *8*, 24, doi:10.1186/s40486-020-00127-8.

71. Zhai, W.; Xia, Q.; Zhou, K.; Yue, X.; Ren, M.; Zheng, G.; Dai, K.; Liu, C.; Shen, C. Multifunctional Flexible Carbon Black/Polydimethylsiloxane Piezoresistive Sensor with Ultrahigh Linear Range, Excellent Durability and Oil/Water Separation Capability. *Chemical Engineering Journal* **2019**, *372*, 373–382, doi:10.1016/j.cej.2019.04.142.

72. Xu, M.; Gao, Y.; Yu, G.; Lu, C.; Tan, J.; Xuan, F. Flexible Pressure Sensor Using Carbon Nanotube-Wrapped Polydimethylsiloxane Microspheres for Tactile Sensing. *Sens Actuators A Phys* **2018**, *284*, 260–265, doi:10.1016/j.sna.2018.10.040.

73. Bhatt, B.B.; Kumar, L.; Kushwaha, A.; Gupta, D. An Ultra-Compressible Piezoresistive Strain and Pressure Sensor Based on RGO-CNT-Melamine Foam Composite for Biomedical Sensing. *Sens Actuators A Phys* **2021**, *331*, 112875, doi:10.1016/j.sna.2021.112875.

74. Xiong, Y.; Zhu, Y.; Liu, X.; Zhu, P.; Hu, Y.; Sun, R.; Wong, C.-P. A Flexible Pressure Sensor Based on Melamine Foam Capped by Copper Nanowires and Reduced Graphene Oxide. *Mater Today Commun* **2020**, *24*, 100970, doi:10.1016/j.mtcomm.2020.100970.

75. Cai, B.; Wang, L.; Yu, F.; Jia, jianming; Li, J.; Li, X.; Yang, X.; Jiang, Y.; Lü, W. Compressible Piezoresistive Pressure Sensor Based on Ag Nanowires Wrapped

Conductive Carbonized Melamine Foam. *Applied Physics A* **2022**, *128*, 6, doi:10.1007/s00339-021-05143-y.

76. Li, Z.-X.; Gao, X.-Y.; Huang, P.; Li, Y.-Q.; Fu, S.-Y. A Flexible Carbonized Melamine Foam/Silicone/Epoxy Composite Pressure Sensor with Temperature and Voltage-Adjusted Piezoresistivity for Ultrawide Pressure Detection. *J Mater Chem A Mater* **2022**, *10*, 9114–9120, doi:10.1039/D1TA10965K.

77. Veeralingam, S.; Praveen, S.; Vemula, M.; Badhulika, S. One-Step Synthesis of Carbon-Doped PPy Nanoparticles Interspersed in 3D Porous Melamine Foam as a High-Performance Piezoresistive Pressure, Strain, and Breath Sensor. *Mater Chem Front* **2022**, *6*, 570–579, doi:10.1039/D1QM01427G.

78. Yang, J.; Ye, Y.; Li, X.; Lü, X.; Chen, R. Flexible, Conductive, and Highly Pressure-Sensitive Graphene-Polyimide Foam for Pressure Sensor Application. *Compos Sci Technol* **2018**, *164*, 187–194, doi:10.1016/j.compscitech.2018.05.044.

79. Zhong, A.; Li, J.; Zhang, Y.; Zhang, F.; Wang, T.; Zhang, G.; Sun, R.; Wong, C.-P. Low Temperature Microwave Fabrication of Three-Dimensional Graphene/Polyimide Foams with Flexibility Strain Responsivity. *Compos Part A Appl Sci Manuf* **2020**, *137*, 105995, doi:10.1016/j.compositesa.2020.105995.

80. Zhai, Y.; Yu, Y.; Zhou, K.; Yun, Z.; Huang, W.; Liu, H.; Xia, Q.; Dai, K.; Zheng, G.; Liu, C.; et al. Flexible and Wearable Carbon Black/Thermoplastic Polyurethane Foam with a Pinnate-Veined Aligned Porous Structure for Multifunctional Piezoresistive Sensors. *Chemical Engineering Journal* **2020**, *382*, 122985, doi:10.1016/j.cej.2019.122985.

81. Yang, H.; Shang, J.-C.; Wang, W.-F.; Yang, Y.-F.; Yuan, Y.-N.; Lei, H.-S.; Fang, D.-N. Polyurethane Sponges-Based Ultrasensitive Pressure Sensor via Bioinspired Microstructure Generated by Pre-Strain Strategy. *Compos Sci Technol* **2022**, *221*, 109308, doi:10.1016/j.compscitech.2022.109308.

82. Zhu, H.; Dai, S.; Cao, J.; Bai, H.; Zhong, Y.; Zhang, Z.; Cheng, G.; Yuan, N.; Ding, J. A High-Performance Textile Pressure Sensor Based on Carbon Black/Carbon Nanotube-Polyurethane Coated Fabrics with Porous Structure for Monitoring Human Motion. *Mater Today Commun* **2022**, *33*, 104541, doi:10.1016/j.mtcomm.2022.104541.

83. Zhu, G.; Li, H.; Peng, M.; Zhao, G.; Chen, J.; Zhu, Y. Highly-Stretchable Porous Thermoplastic Polyurethane/Carbon Nanotubes Composites as a Multimodal Sensor. *Carbon N Y* **2022**, *195*, 364–371, doi:10.1016/j.carbon.2022.04.033.

84. Wang, T.; Li, J.; Zhang, Y.; Liu, F.; Zhang, B.; Wang, Y.; Jiang, R.; Zhang, G.; Sun, R.; Wong, C. Highly Ordered 3D Porous Graphene Sponge for Wearable Piezoresistive Pressure Sensor Applications. *Chemistry – A European Journal* **2019**, *25*, 6378–6384, doi:10.1002/chem.201900014.

85. Jothi, L.; Nageswaran, G. Plasma Modified Polymeric Materials for Biosensors/Biodevice Applications. In *Non-Thermal Plasma Technology for Polymeric Materials*; Elsevier, 2019; pp. 409–437.

86. Wang, Q.; Chen, A.; Gu, H.; Qin, G.; Zhang, J.; Xu, J.; Jiang, G.; Liu, W.; Zhang, Z.; Huang, H. Highly Interconnected Porous PDMS/CNTs Sandwich Sponges with Anti-Icing/Deicing Microstructured Surfaces. *J Mater Sci* **2021**, *56*, 11723–11735, doi:10.1007/s10853-021-06052-4.

87. Zhou, L.; Rada, J.; Zhang, H.; Song, H.; Mirniaharikandi, S.; Ooi, B.S.; Gan, Q. Sustainable and Inexpensive Polydimethylsiloxane Sponges for Daytime Radiative Cooling. *Advanced Science* **2021**, *8*, 2102502, doi:10.1002/advs.202102502.

88. Pharino, U.; Sinsanong, Y.; Pongampai, S.; Charoonsuk, T.; Pakawanit, P.; Sriphan, S.; Vittayakorn, N.; Vittayakorn, W. Influence of Pore Morphologies on the Mechanical and Tribo-Electrical Performance of Polydimethylsiloxane Sponge Fabricated via Commercial Seasoning Templates. *Radiation Physics and Chemistry* **2021**, *189*, 109720, doi:10.1016/j.radphyschem.2021.109720.

89. Pruvost, M.; Smit, W.J.; Monteux, C.; Poulin, P.; Colin, A. Polymeric Foams for Flexible and Highly Sensitive Low-Pressure Capacitive Sensors. *npj Flexible Electronics* **2019**, *3*, 7, doi:10.1038/s41528-019-0052-6.

90. Wang, H.; Zhang, R.; Yuan, D.; Xu, S.; Wang, L. Gas Foaming Guided Fabrication of 3D Porous Plasmonic Nanoplatform with Broadband Absorption, Tunable Shape, Excellent Stability, and High Photothermal Efficiency for Solar Water Purification. *Adv Funct Mater* **2020**, *30*, 2003995, doi:10.1002/adfm.202003995.

91. Drozdov, A.D.; Claville Christiansen, J. The Effect of Porosity on Elastic Moduli of Polymer Foams. *J Appl Polym Sci* **2020**, *137*, 48449, doi:10.1002/app.48449.

92. Liu, C.; Le, L.; Zhang, M.; Ding, J. Tunable Large-Scale Compressive Strain Sensor Based on Carbon Nanotube/Polydimethylsiloxane Foam Composites by Additive Manufacturing. *Adv Eng Mater* **2022**, *24*, 2101337, doi:10.1002/adem.202101337.

93. Timusk, M.; Nigol, I.A.; Vlassov, S.; Oras, S.; Kangur, T.; Linarts, A.; Šutka, A. Low-Density PDMS Foams by Controlled Destabilization of Thixotropic Emulsions. *J Colloid Interface Sci* **2022**, *626*, 265–275, doi:10.1016/j.jcis.2022.06.150.

94. Bélanger, M.-C.; Marois, Y. Hemocompatibility, Biocompatibility, Inflammatory and *in Vivo* Studies of Primary Reference Materials Low-Density Polyethylene and Polydimethylsiloxane: A Review. *J Biomed Mater Res* **2001**, *58*, 467–477, doi:10.1002/jbm.1043.

95. Lötters, J.C.; Olthuis, W.; Veltink, P.H.; Bergveld, P. The Mechanical Properties of the Rubber Elastic Polymer Polydimethylsiloxane for Sensor Applications. *Journal*

of Micromechanics and Microengineering **1997**, *7*, 145–147, doi:10.1088/0960-1317/7/3/017.

96. Mata, A.; Fleischman, A.J.; Roy, S. Characterization of Polydimethylsiloxane (PDMS) Properties for Biomedical Micro/Nanosystems. *Biomed Microdevices* **2005**, *7*, 281–293, doi:10.1007/s10544-005-6070-2.

97. García-Valverde, M.; Chatzimitakos, T.; Lucena, R.; Cárdenas, S.; Stalikas, C. Melamine Sponge Functionalized with Urea-Formaldehyde Co-Oligomers as a Sorbent for the Solid-Phase Extraction of Hydrophobic Analytes. *Molecules* **2018**, *23*, 2595, doi:10.3390/molecules23102595.

98. Khan, Md.R.R.; An, T.K.; Lee, H.S. A Battery-Free, Chipless, Highly Sensitive LC Pressure Sensor Tag Using PEDOT: PSS and Melamine Foam. *IEEE Sens J* **2021**, *21*, 2184–2193, doi:10.1109/JSEN.2020.3021076.

99. Cui, W.; Li, X.; Li, X.; Si, T.; Lu, L.; Ma, T.; Wang, Q. Thermal Performance of Modified Melamine Foam/Graphene/Paraffin Wax Composite Phase Change Materials for Solar-Thermal Energy Conversion and Storage. *J Clean Prod* **2022**, *367*, 133031, doi:10.1016/j.jclepro.2022.133031.

100. Yan, L.; Fu, L.; Chen, Y.; Tian, H.; Xiang, A.; Rajulu, A.V. Improved Thermal Stability and Flame Resistance of Flexible Polyimide Foams by Vermiculite Reinforcement. *J Appl Polym Sci* **2017**, *134*, doi:10.1002/app.44828.

101. Gu, W.; Wang, G.; Zhou, M.; Zhang, T.; Ji, G. Polyimide-Based Foams: Fabrication and Multifunctional Applications. *ACS Appl Mater Interfaces* **2020**, *12*, 48246–48258, doi:10.1021/acsami.0c15771.

102. Zhu, Z.; Yao, H.; Dong, J.; Qian, Z.; Dong, W.; Long, D. High-Mechanical-Strength Polyimide Aerogels Crosslinked with 4, 4′-Oxydianiline-Functionalized Carbon Nanotubes. *Carbon N Y* **2019**, *144*, 24–31, doi:10.1016/j.carbon.2018.11.057.

103. Pan, L.-Y.; Shen, Y.-X.; Zhan, M.-S.; Wang, K.; Gao, D.-L. Visualization Study of Foaming Process for Polyimide Foams and Its Reinforced Foams. *Polym Compos* **2008**, *31*, NA-NA, doi:10.1002/pc.20764.

104. Li, Y.; Liu, X.-Y.; Zhan, M.-S.; Wang, K. Effects of 3,4′-Oxydianiline on the Structures and Properties of a Novel Aromatic Polyimide Foam. *J Appl Polym Sci* **2012**, *125*, 4128–4134, doi:10.1002/app.35683.

105. Huang, W.; Dai, K.; Zhai, Y.; Liu, H.; Zhan, P.; Gao, J.; Zheng, G.; Liu, C.; Shen, C. Flexible and Lightweight Pressure Sensor Based on Carbon Nanotube/Thermoplastic Polyurethane-Aligned Conductive Foam with Superior Compressibility and Stability. *ACS Appl Mater Interfaces* **2017**, *9*, 42266–42277, doi:10.1021/acsami.7b16975.

106. Liu, H.; Gao, J.; Huang, W.; Dai, K.; Zheng, G.; Liu, C.; Shen, C.; Yan, X.; Guo, J.; Guo, Z. Electrically Conductive Strain Sensing Polyurethane Nanocomposites with Synergistic Carbon Nanotubes and Graphene Bifillers. *Nanoscale* **2016**, *8*, 12977–12989, doi:10.1039/C6NR02216B.

107. Liu, H.; Li, Y.; Dai, K.; Zheng, G.; Liu, C.; Shen, C.; Yan, X.; Guo, J.; Guo, Z. Electrically Conductive Thermoplastic Elastomer Nanocomposites at Ultralow Graphene Loading Levels for Strain Sensor Applications. *J Mater Chem C Mater* **2016**, *4*, 157–166, doi:10.1039/C5TC02751A.

108. Lan, Y.; Liu, H.; Cao, X.; Zhao, S.; Dai, K.; Yan, X.; Zheng, G.; Liu, C.; Shen, C.; Guo, Z. Electrically Conductive Thermoplastic Polyurethane/Polypropylene Nanocomposites with Selectively Distributed Graphene. *Polymer (Guildf)* **2016**, *97*, 11–19, doi:10.1016/j.polymer.2016.05.017.

109. Yilgör, I.; Yilgör, E.; Wilkes, G.L. Critical Parameters in Designing Segmented Polyurethanes and Their Effect on Morphology and Properties: A Comprehensive Review. *Polymer (Guildf)* **2015**, *58*, A1–A36.

110. Soto, M.; Sebastián, R.M.; Marquet, J. Photochemical Activation of Extremely Weak Nucleophiles: Highly Fluorinated Urethanes and Polyurethanes from Polyfluoro Alcohols. *J Org Chem* **2014**, *79*, 5019–5027, doi:10.1021/jo5005789.

111. Oppon, C.; Hackney, P.M.; Shyha, I.; Birkett, M. Effect of Varying Mixing Ratios and Pre-Heat Temperature on the Mechanical Properties of Polyurethane (PU) Foam. *Procedia Eng* **2015**, *132*, 701–708, doi:10.1016/j.proeng.2015.12.550.

112. Chen, K.-S.; Leon Yu, T.; Chen, Y.-S.; Lin, T.-L.; Liu, W.-J. Soft-and Hard-Segment Phase Segregation of Polyester-Based Polyurethane. *Journal of Polymer Research* **2001**, *8*, 99–109, doi:10.1007/s10965-006-0139-3.

113. Tang, Y.W.; Labow, R.S.; Santerre, J.P. Enzyme-Induced Biodegradation of Polycarbonate Polyurethanes: Dependence on Hard-Segment Concentration. *J Biomed Mater Res* **2001**, *56*, 516–528, doi:10.1002/1097-4636(20010915)56:4<516::AID-JBM1123>3.0.CO;2-B.

114. Verdolotti, L.; Di Caprio, M.R.; Lavorgna, M.; Buonocore, G.G. Polyurethane Nanocomposite Foams. In *Polyurethane Polymers*; Elsevier, 2017; pp. 277–310.

115. Society, A.C. *Polyurethane Chemistry: Renewable Polyols and Isocyanates*; ACS Publications, 2021; ISBN 0841298408.

116. Ng, Z.C.; Roslan, R.A.; Lau, W.J.; Gürsoy, M.; Karaman, M.; Jullok, N.; Ismail, A.F. A Green Approach to Modify Surface Properties of Polyurethane Foam for Enhanced Oil Absorption. *Polymers (Basel)* **2020**, *12*, 1883, doi:10.3390/polym12091883.

117. Tay, R.Y.; Li, H.; Lin, J.; Wang, H.; Lim, J.S.K.; Chen, S.; Leong, W.L.; Tsang, S.H.; Teo, E.H.T. Lightweight, Superelastic Boron Nitride/Polydimethylsiloxane Foam as Air Dielectric Substitute for Multifunctional Capacitive Sensor Applications. *Adv Funct Mater* **2020**, *30*, 1909604, doi:10.1002/adfm.201909604.

118. Grande, J.B.; Fawcett, A.S.; McLaughlin, A.J.; Gonzaga, F.; Bender, T.P.; Brook, M.A. Anhydrous Formation of Foamed Silicone Elastomers Using the Piers–Rubinsztajn Reaction. *Polymer (Guildf)* **2012**, *53*, 3135–3142, doi:10.1016/j.polymer.2012.05.033.

119. Mu, L.; Yue, X.; Hao, B.; Wang, R.; Ma, P.-C. Facile Preparation of Melamine Foam with Superhydrophobic Performance and Its System Integration with Prototype Equipment for the Clean-up of Oil Spills on Water Surface. *Science of The Total Environment* **2022**, *833*, 155184, doi:10.1016/j.scitotenv.2022.155184.

120. Patel, P.S.; Shepherd, D.E.; Hukins, D.W. Compressive Properties of Commercially Available Polyurethane Foams as Mechanical Models for Osteoporotic Human Cancellous Bone. *BMC Musculoskelet Disord* **2008**, *9*, 137, doi:10.1186/1471-2474-9-137.

121. Cuenca, J.; Van der Kelen, C.; Göransson, P. A General Methodology for Inverse Estimation of the Elastic and Anelastic Properties of Anisotropic Open-Cell Porous Materials—with Application to a Melamine Foam. *J Appl Phys* **2014**, *115*, 84904, doi:10.1063/1.4865789.

122. Silcox, R.; Bolton, J.S.; Kim, N.; Cano, R.; Howerton, B. Development of Polyimide Foam for Aircraft Sidewall Applications. In Proceedings of the 51st AIAA Aerospace Sciences Meeting Including the New Horizons Forum and Aerospace Exposition; 2013; p. 213.

123. Zhang, H.; Fan, X.; Chen, W.; Wang, Y.; Liu, C.; Cui, B.; Li, G.; Song, J.; Zhao, D.; Wang, D.; et al. A Simple and Green Strategy for Preparing Flexible Thermoplastic Polyimide Foams with Exceptional Mechanical, Thermal-Insulating Properties, and Temperature Resistance for High-Temperature Lightweight Composite Sandwich Structures. *Compos B Eng* **2022**, *228*, 109405, doi:10.1016/j.compositesb.2021.109405.

124. Teixeira, I.; Castro, I.; Carvalho, V.; Rodrigues, C.; Souza, A.; Lima, R.; Teixeira, S.; Ribeiro, J. Polydimethylsiloxane Mechanical Properties: A Systematic Review. *AIMS Mater Sci* **2021**, *8*, 952–973, doi:10.3934/matersci.2021058.

125. Jia, H.; Kong, Q.-Q.; Liu, Z.; Wei, X.-X.; Li, X.-M.; Chen, J.-P.; Li, F.; Yang, X.; Sun, G.-H.; Chen, C.-M. 3D Graphene/ Carbon Nanotubes/ Polydimethylsiloxane Composites as High-Performance Electromagnetic Shielding Material in X-Band. *Compos Part A Appl Sci Manuf* **2020**, *129*, 105712, doi:10.1016/j.compositesa.2019.105712.

126. Cao, X.; Liu, H.; Cai, J.; Chen, L.; Yang, X.; Liu, M. Chinese Ink Coated Melamine Foam with Joule Heating and Photothermal Effect for Strain Sensor and Seawater Desalination. *Compos Part A Appl Sci Manuf* **2021**, *149*, 106535, doi:10.1016/j.compositesa.2021.106535.

127. Li, C.; Ma, H.; Zhou, Z.; Xu, W.; Ren, F.; Yang, X. Preparation and Properties of Melamine-Formaldehyde Rigid Closed-Cell Foam Toughened by Ethylene Glycol/Carbon Fiber. *Cellular Polymers* **2021**, *40*, 55–72, doi:10.1177/0262489320929232.

128. Shi, Y.; Hu, A.; Wang, Z.; Li, K.; Yang, S. Closed-Cell Rigid Polyimide Foams for High-Temperature Applications: The Effect of Structure on Combined Properties. *Polymers (Basel)* **2021**, *13*, 4434, doi:10.3390/polym13244434.

129. Xu, M.; Yang, L.; Zhang, L.; Yan, S. *Innovative Technologies for Printing and Packaging*; Springer Nature, 2023; Vol. 991; ISBN 9811990247.

130. Fan, L.; Wang, R.; Zhang, Q.; Liu, S.; He, R.; Zhang, R.; Shen, M.; Xiang, X.; Zhou, Y. *In Situ* Self-Foaming Preparation of Hydrophobic Polyurethane Foams for Oil/Water Separation. *New Journal of Chemistry* **2021**, *45*, 13902–13908, doi:10.1039/D0NJ05208F.

131. Borreguero, A.M.; Zamora, J.; Garrido, I.; Carmona, M.; Rodríguez, J.F. Improving the Hydrophilicity of Flexible Polyurethane Foams with Sodium Acrylate Polymer. *Materials* **2021**, *14*, 2197, doi:10.3390/ma14092197.

132. Trantidou, T.; Elani, Y.; Parsons, E.; Ces, O. Hydrophilic Surface Modification of PDMS for Droplet Microfluidics Using a Simple, Quick, and Robust Method via PVA Deposition. *Microsyst Nanoeng* **2017**, *3*, 16091, doi:10.1038/micronano.2016.91.

133. Park, E.J.; Cho, Y.K.; Kim, D.H.; Jeong, M.-G.; Kim, Y.H.; Kim, Y.D. Hydrophobic Polydimethylsiloxane (PDMS) Coating of Mesoporous Silica and Its Use as a Preconcentrating Agent of Gas Analytes. *Langmuir* **2014**, *30*, 10256–10262, doi:10.1021/la502915r.

134. Li, Q.; Sun, X.; Li, Y.; Xu, L. Hydrophobic Melamine Foam as the Solvent Holder for Liquid–Liquid Microextraction. *Talanta* **2019**, *191*, 469–478, doi:10.1016/j.talanta.2018.09.003.

135. Akhiani, A.R.; Cornelis Metselaar, H.S.; Ang, B.C.; Mehrali, M.; Mehrali, M. Highly Hydrophobic Silanized Melamine Foam for Facile and Uniform Assembly of Graphene Nanoplatelet towards Efficient Light-to-Thermal Energy Storage. *Mater Today Energy* **2022**, *28*, 101077, doi:10.1016/j.mtener.2022.101077.

136. Kausar, A. Emerging Polyimide and Graphene Derived Nanocomposite Foam: Research and Technical Tendencies. *Journal of Macromolecular Science, Part A* **2021**, *58*, 643–658, doi:10.1080/10601325.2021.1934011.

137. Gama, N.; Ferreira, A.; Barros-Timmons, A. Polyurethane Foams: Past, Present, and Future. *Materials* **2018**, *11*, 1841, doi:10.3390/ma11101841.

138. Hu, W.-J.; Xia, Q.-Q.; Pan, H.-T.; Chen, H.-Y.; Qu, Y.-X.; Chen, Z.-Y.; Zhang, G.-D.; Zhao, L.; Gong, L.-X.; Xue, C.-G.; et al. Green and Rapid Preparation of Fluorosilicone Rubber Foam Materials with Tunable Chemical Resistance for Efficient Oil–Water Separation. *Polymers (Basel)* **2022**, *14*, 1628, doi:10.3390/polym14081628.

139. Jun, Y.-S.; Sy, S.; Ahn, W.; Zarrin, H.; Rasen, L.; Tjandra, R.; Amoli, B.M.; Zhao, B.; Chiu, G.; Yu, A. Highly Conductive Interconnected Graphene Foam Based Polymer Composite. *Carbon N Y* **2015**, *95*, 653–658, doi:10.1016/j.carbon.2015.08.079.

140. Biron, M. Detailed Accounts of Thermoset Resins for Moulding and Composite Matrices. In *Thermosets and Composites*; 2004; pp. 183–327.

141. Williams, M.K.; Holland, D.B.; Melendez, O.; Weiser, E.S.; Brenner, J.R.; Nelson, G.L. Aromatic Polyimide Foams: Factors That Lead to High Fire Performance. *Polym Degrad Stab* **2005**, *88*, 20–27, doi:10.1016/j.polymdegradstab.2003.12.012.

142. Guelcher, S.A.; Patel, V.; Gallagher, K.M.; Connolly, S.; Didier, J.E.; Doctor, J.S.; Hollinger, J.O. Synthesis and *In Vitro* Biocompatibility of Injectable Polyurethane Foam Scaffolds. *Tissue Eng* **2006**, *12*, 1247–1259, doi:10.1089/ten.2006.12.1247.

143. Singhal, P.; Rodriguez, J.N.; Small, W.; Eagleston, S.; Van de Water, J.; Maitland, D.J.; Wilson, T.S. Ultra Low Density and Highly Crosslinked Biocompatible Shape Memory Polyurethane Foams. *J Polym Sci B Polym Phys* **2012**, *50*, 724–737, doi:10.1002/polb.23056.

144. Victor, A.; Ribeiro, J.; F. Araújo, F. Study of PDMS Characterization and Its Applications in Biomedicine: A Review. *Journal of Mechanical Engineering and Biomechanics* **2019**, *4*, 1–9, doi:10.24243/JMEB/4.1.163.

145. Yan, C.; Luo, Y.; Zhang, W.; Zhu, Z.; Li, P.; Li, N.; Chen, Y.; Jin, T. Preparation of a Novel Melamine Foam Structure and Properties. *J Appl Polym Sci* **2022**, *139*, 51992, doi:10.1002/app.51992.

146. Constantin, C.P.; Aflori, M.; Damian, R.F.; Rusu, R.D. Biocompatibility of Polyimides: A Mini-Review. *Materials* **2019**, *12*, 3166, doi:10.3390/ma12193166.

147. Rodrigues, I.C.P.; Woigt, L.F.; Pereira, K.D.; Luchessi, A.D.; Lopes, É.S.N.; Webster, T.J.; Gabriel, L.P. Low-Cost Hybrid Scaffolds Based on Polyurethane and Gelatin. *Journal of Materials Research and Technology* **2020**, *9*, 7777–7785, doi:10.1016/j.jmrt.2020.04.049.

148. Alatawi, L.; Abdullah, A.H.; Jamil, S.N.A.Md.; Yunus, R. A Facile and Green Synthesis of Hydrophobic Polydimethylsiloxane Foam for Benzene, Toluene, and Xylene Removal. *Separations* **2023**, *10*, 377, doi:10.3390/separations10070377.

149. Tian, C.; Li, B.; Hu, X.; Wu, J.; Li, P.; Xiang, X.; Zu, X.; Li, S. Melamine Foam Derived 2H/1T MoS_2 as Flexible Interlayer with Efficient Polysulfides Trapping and Fast Li^+ Diffusion to Stabilize Li–S Batteries. *ACS Appl Mater Interfaces* **2021**, *13*, 6229–6240, doi:10.1021/acsami.0c19725.

150. Behrisch, R.; Wittmaack, K. *Sputtering by Particle Bombardment I*; Behrisch, R., Ed.; Topics in Applied Physics; Springer Berlin Heidelberg: Berlin, Heidelberg, 1981; Vol. 47; ISBN 978-3-540-10521-3.

151. Wu, Y.; Liu, H.; Chen, S.; Dong, X.; Wang, P.; Liu, S.; Lin, Y.; Wei, Y.; Liu, L. Channel Crack-Designed Gold@PU Sponge for Highly Elastic Piezoresistive Sensor with Excellent Detectability. *ACS Appl Mater Interfaces* **2017**, *9*, 20098–20105, doi:10.1021/acsami.7b04605.

152. Krebs, F.C. Fabrication and Processing of Polymer Solar Cells: A Review of Printing and Coating Techniques. *Solar Energy Materials and Solar Cells* **2009**, *93*, 394–412, doi:10.1016/j.solmat.2008.10.004.

153. Zhang, P.; Chen, Y.; Li, Y.; Zhang, Y.; Zhang, J.; Huang, L. Erratum: A Flexible Strain Sensor Based on the Porous Structure of a Carbon Black/Carbon Nanotube Conducting Network for Human Motion Detection (Sensors, (2020) 20, 1154, 10.3390/S20041154). *Sensors (Switzerland)* 2020, *20*.

154. Aziz, F.; Ismail, A.F. Spray Coating Methods for Polymer Solar Cells Fabrication: A Review. *Mater Sci Semicond Process* **2015**, *39*, 416–425, doi:10.1016/j.mssp.2015.05.019.

155. Paszkiewicz, S.; Szymczyk, A. Graphene-Based Nanomaterials and Their Polymer Nanocomposites. In *Nanomaterials and Polymer Nanocomposites*; Elsevier, 2019; pp. 177–216.

156. Hu, Z.; Xin, Y.; Fu, Q. Ultrahigh Sensitivity and Wide Strain Range of Porous Pressure Sensor Based on Binary Conductive Fillers by In-Situ Polymerization. *Journal of Polymer Research* **2021**, *28*, 134, doi:10.1007/s10965-021-02484-3.

157. Nabeel, M.; Varga, M.; Kuzsella, L.; Fiser, B.; Vanyorek, L.; Viskolcz, B. The Effect of Pore Volume on the Behavior of Polyurethane-Foam-Based Pressure Sensors. *Polymers (Basel)* **2022**, *14*, 3652, doi:10.3390/polym14173652.

158. Davis, J.R. *Handbook Thermal Spray Technology*; Tucker, R.C., Ed.; ASM International, 2004; ISBN 978-1-62708-171-9.

159. Karthikeyan, J. Cold Spray Technology: The Cold Spray Process Has the Potential to Reduce Costs and Improve Quality in Both Coatings and Freeform Fabrication of near-Net-Shape Parts. *Advanced materials & processes* **2005**, *163*, 33–36.

160. Assadi, H.; Gärtner, F.; Stoltenhoff, T.; Kreye, H. Bonding Mechanism in Cold Gas Spraying. *Acta Mater* **2003**, *51*, 4379–4394, doi:10.1016/S1359-6454(03)00274-X.

161. Mattox, D.M. Vacuum Deposition, Reactive Evaporation, and Gas Evaporation. In *Surface Engineering*; ASM International, 1994; pp. 556–572.

162. Cramer, S.D.; Covino Jr, B.S. Corrosion: Fundamentals, Testing, and Protection, Volume 13A, ASM Handbook. *Journal of Thermal Spray Technology* **2003**, *12*, 459.

163. Guo, Q.; Ghadiri, R.; Weigel, T.; Aumann, A.; Gurevich, E.; Esen, C.; Medenbach, O.; Cheng, W.; Chichkov, B.; Ostendorf, A. Comparison of in Situ and Ex Situ Methods for Synthesis of Two-Photon Polymerization Polymer Nanocomposites. *Polymers (Basel)* **2014**, *6*, 2037–2050, doi:10.3390/polym6072037.

164. Chun, S.; Hong, A.; Choi, Y.; Ha, C.; Park, W. A Tactile Sensor Using a Conductive Graphene-Sponge Composite. *Nanoscale* **2016**, *8*, 9185–9192, doi:10.1039/C6NR00774K.

165. Huang, Y.; Zhang, J.; Pu, J.; Guo, X.; Qiu, J.; Ma, Y.; Zhang, Y.; Yang, X. Resistive Pressure Sensor for High-Sensitivity e-Skin Based on Porous Sponge Dip-Coated CB/MWCNTs/SR Conductive Composites. *Mater Res Express* **2018**, *5*, 065701, doi:10.1088/2053-1591/aac8c0.

166. Ding, Y.; Xu, T.; Onyilagha, O.; Fong, H.; Zhu, Z. Recent Advances in Flexible and Wearable Pressure Sensors Based on Piezoresistive 3D Monolithic Conductive Sponges. *ACS Appl Mater Interfaces* **2019**, *11*, 6685–6704, doi:10.1021/acsami.8b20929.

167. Chen, Q.; Gao, Q.; Wang, X.; Schubert, D.W.; Liu, X. Flexible, Conductive, and Anisotropic Thermoplastic Polyurethane/Polydopamine /MXene Foam for Piezoresistive Sensors and Motion Monitoring. *Compos Part A Appl Sci Manuf* **2022**, *155*, 106838, doi:10.1016/j.compositesa.2022.106838.

168. Nabeel, M.; Varga, M.; Kuzsela, L.; Filep, Á.; Fiser, B.; Viskolcz, B.; Kollar, M.; Vanyorek, L. Preparation of Bamboo-Like Carbon Nanotube Loaded Piezoresistive Polyurethane-Silicone Rubber Composite. *Polymers (Basel)* **2021**, *13*, 2144, doi:10.3390/polym13132144.

169. Lv, B.; Chen, X.; Liu, C. A Highly Sensitive Piezoresistive Pressure Sensor Based on Graphene Oxide/Polypyrrole@Polyurethane Sponge. *Sensors* **2020**, *20*, 1219, doi:10.3390/s20041219.

170. Lü, X.; Yu, T.; Meng, F.; Bao, W. Wide-Range and High-Stability Flexible Conductive Graphene/Thermoplastic Polyurethane Foam for Piezoresistive Sensor Applications. *Adv Mater Technol* **2021**, *6*, 2100248, doi:10.1002/admt.202100248.

171. Vanyorek, L.; Muranszky, G.; Sikora, E.; Pénzeli, X.; Prekob, Á.; Kiss, A.; Fiser, B.; Viskolcz, B. Synthesis Optimization and Characterization of Nitrogen-Doped Bamboo-Shaped Carbon Nanotubes. *J Nanosci Nanotechnol* **2019**, *19*, 429–435, doi:10.1166/jnn.2019.15776.

172. Youssry, M.; Al-Ruwaidhi, M.; Zakeri, M.; Zakeri, M. Physical Functionalization of Multi-Walled Carbon Nanotubes for Enhanced Dispersibility in Aqueous Medium. *Emergent Mater* **2020**, *3*, 25–32, doi:10.1007/s42247-020-00076-3.

173. Fadley, C.S. X-Ray Photoelectron Spectroscopy: Progress and Perspectives. *J Electron Spectros Relat Phenomena* **2010**, *178*, 2–32, doi:10.1016/j.elspec.2010.01.006.

174. Lothenbach, B.; Durdzinski, P.; De Weerdt, K. Thermogravimetric Analysis. *A practical guide to microstructural analysis of cementitious materials* **2016**, *1*, 177–211.

175. Majeed, S.; Zhao, J.; Zhang, L.; Anjum, S.; Liu, Z.; Xu, G. Synthesis and Electrochemical Applications of Nitrogen-Doped Carbon Nanomaterials. *Nanotechnol Rev* **2013**, *2*, 615–635, doi:10.1515/ntrev-2013-0007.

176. Chen, Y.; Mastalerz, M.; Schimmelmann, A. Characterization of Chemical Functional Groups in Macerals across Different Coal Ranks via Micro-FTIR Spectroscopy. *Int J Coal Geol* **2012**, *104*, 22–33, doi:10.1016/j.coal.2012.09.001.

177. Dutta, A. Fourier Transform Infrared Spectroscopy. *Spectroscopic methods for nanomaterials characterization* **2017**, 73–93.

178. Shieh, Y.; Chen, J.; Twu, Y.; Chen, W. The Effect of PH and Ionic Strength on the Dispersion of Carbon Nanotubes in Poly (Acrylic Acid) Solutions. *Polym Int* **2012**, *61*, 554–559, doi:10.1002/pi.3203.

179. Huo, W.; Zhang, X.; Gan, K.; Chen, Y.; Xu, J.; Yang, J. Effect of Zeta Potential on Properties of Foamed Colloidal Suspension. *J Eur Ceram Soc* **2019**, *39*, 574–583, doi:10.1016/j.jeurceramsoc.2018.08.035.

180. Xu, M.; Li, F.; Zhang, Z.; Shen, T.; Zhang, Q.; Qi, J. Stretchable and Multifunctional Strain Sensors Based on 3D Graphene Foams for Active and Adaptive Tactile Imaging. *Sci China Mater* **2019**, *62*, 555–565, doi:10.1007/s40843-018-9348.

181. Xia, G.; Zhou, C.; Jin, S.; Huang, C.; Xing, J.; Liu, Z. Sensitivity Enhancement of Two-Dimensional Materials Based on Genetic Optimization in Surface Plasmon Resonance. *Sensors* **2019**, *19*, 1198, doi:10.3390/s19051198.

182. Cheng, B.; Yang, S.; Woldu, Y.T.; Shafique, S.; Wang, F. A Study on the Mechanical Properties of a Carbon Nanotube Probe with a High Aspect Ratio. *Nanotechnology* **2020**, *31*, 145707, doi:10.1088/1361-6528/ab6239.

183. Chen, B.; Shen, J.; Ye, X.; Imai, H.; Umeda, J.; Takahashi, M.; Kondoh, K. Solid-State Interfacial Reaction and Load Transfer Efficiency in Carbon Nanotubes (CNTs)-Reinforced Aluminum Matrix Composites. *Carbon N Y* **2017**, *114*, 198–208, doi:10.1016/j.carbon.2016.12.013.

184. Demirer, G.S.; Zhang, H.; Matos, J.L.; Goh, N.S.; Cunningham, F.J.; Sung, Y.; Chang, R.; Aditham, A.J.; Chio, L.; Cho, M.-J. High Aspect Ratio Nanomaterials Enable Delivery of Functional Genetic Material without DNA Integration in Mature Plants. *Nat Nanotechnol* **2019**, *14*, 456–464, doi:10.1038/s41565-019-0382-5.

185. Zhang, X.; Chen, F.; Han, L.; Zhang, G.; Hu, Y.; Jiang, W.; Zhu, P.; Sun, R.; Wong, C.-P. Flexible, Highly Sensitive, and Ultrafast Responsive Pressure Sensor with Stochastic Microstructures for Human Health Monitoring. *Adv Eng Mater* **2021**, *23*, 2000902, doi:10.1002/adem.202000902.

186. Slobodian, P.; Riha, P.; Olejnik, R.; Matyas, J.; Kovar, M. Poisson Effect Enhances Compression Force Sensing with Oxidized Carbon Nanotube Network/Polyurethane Sensor. *Sens Actuators A Phys* **2018**, *271*, 76–82, doi:10.1016/j.sna.2017.12.035.

187. Wen, M.; Sun, X.; Su, L.; Shen, J.; Li, J.; Guo, S. The Electrical Conductivity of Carbon Nanotube/Carbon Black/Polypropylene Composites Prepared through Multistage Stretching Extrusion. *Polymer (Guildf)* **2012**, *53*, 1602–1610, doi:10.1016/j.polymer.2012.02.003.

188. Ke, K.; Pötschke, P.; Wiegand, N.; Krause, B.; Voit, B. Tuning the Network Structure in Poly (Vinylidene Fluoride)/Carbon Nanotube Nanocomposites Using Carbon Black: Toward Improvements of Conductivity and Piezoresistive Sensitivity. *ACS Appl Mater Interfaces* **2016**, *8*, 14190–14199, doi:10.1021/acsami.6b03451.

189. Ouellet, S.; Cronin, D.; Worswick, M. Compressive Response of Polymeric Foams under Quasi-Static, Medium and High Strain Rate Conditions. *Polym Test* **2006**, *25*, 731–743, doi:10.1016/j.polymertesting.2006.05.005.

190. Dupuis, R.; Aubry, E. Development and Comparison of Foam Comprehensive Law in Great Deformation. In Proceedings of the Proceedings of the XIth International Congress and Exposition, Orlando, FL, USA; 2008; pp. 2–5.

191. Zhong; Ding; Li; Shen; Yadav; Chen; Bao; Jiang; Wang Facile Fabrication of Conductive Graphene/Polyurethane Foam Composite and Its Application on Flexible Piezo-Resistive Sensors. *Polymers (Basel)* **2019**, *11*, 1289, doi:10.3390/polym11081289.

192. Mora, A.; Verma, P.; Kumar, S. Electrical Conductivity of CNT/Polymer Composites: 3D Printing, Measurements and Modeling. *Compos B Eng* **2020**, *183*, 107600, doi:10.1016/j.compositesb.2019.107600.

193. Cao, P.; Peng, J.; Li, J.; Zhai, M. Highly Conductive Carbon Black Supported Amorphous Molybdenum Disulfide for Efficient Hydrogen Evolution Reaction. *J Power Sources* **2017**, *347*, 210–219, doi:10.1016/j.jpowsour.2017.02.056.

194. Ravindren, R.; Mondal, S.; Nath, K.; Das, N.C. Synergistic Effect of Double Percolated Co-supportive MWCNT-CB Conductive Network for High-performance EMI Shielding Application. *Polym Adv Technol* **2019**, *30*, 1506–1517, doi:10.1002/pat.4582.